SYNTHESIS AND ELECTROCHEMICAL PROPERTIES OF ACTIVATED CARBON FROM CASSAVA STARCH FOR ENERGY STORAGE APPLICATIONS
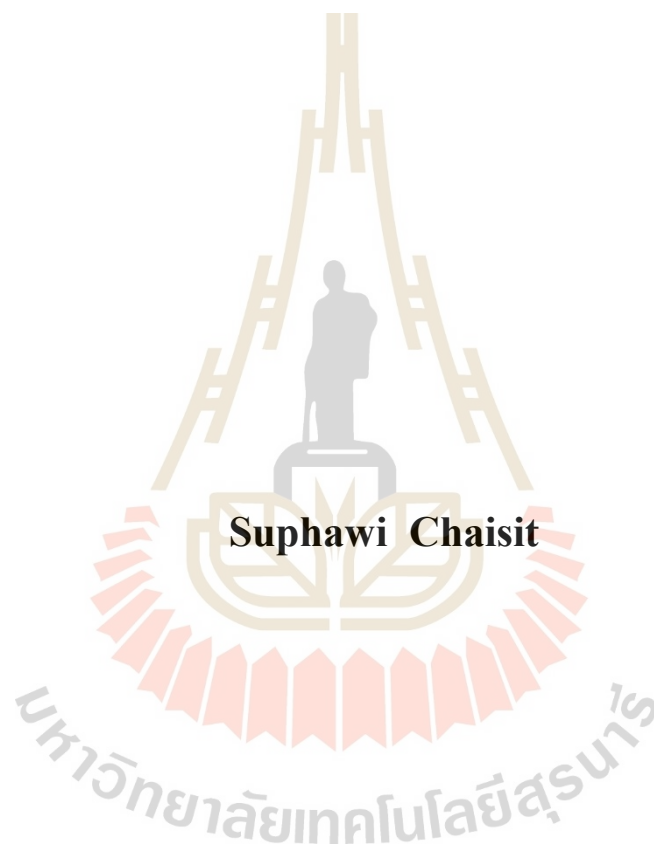
Suphawi Chaisit

A Thesis Submitted in Partial Fulfillment of the Requirements for the

Degree of Master of Science in Physics

Suranaree University of Technology

Academic Year 2018

การสังเคราะห์และคุณสมบัติทางเคมีไฟฟ้าของถ่านกัมมันต์จากแป้งมัน สำปะหลัง เพื่อประยุกต์ใช้ในระบบกักเก็บพลังงาน

นางสาวสุภาวี ชัยสิทธิ์

วิทยานิพนธ์นี้เป็นส่วนหนึ่งของการศึกษาตามหลักสูตรปริญญาวิทยาศาสตรมหาบัณฑิต
สาขาวิชาฟิสิกส์
มหาวิทยาลัยเทคโนโลยีสุรนารี
ปีการศึกษา 2561

SYNTHESIS AND ELECTROCHEMICAL PROPERTIES

OF ACTIVATED CARBON FROM CASSAVA STARCH
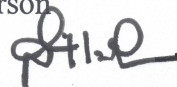
FOR ENERGY STORAGE APPLICATIONS

Suranaree University of Technology has approved this thesis submitted in partial fulfillment of the requirements for a Master's Degree.
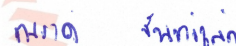
Thesis Examining Committee

_____

(Assoc. Prof. Dr. Sirichok Jungthawan)

Chairperson

_____

(Prof. Dr. Santi Maensiri)

Member (Thesis Advisor)

_____

(Dr. Narong Chanlek)

Member (Thesis Co-Advisor)

_____

(Dr. Wiwat Nuansing)

Member

_____

(Prof. Dr. Santi Maensiri)

Vice Rector for Academic Affairs

and Internationalization

_____

(Assoc. Prof. Dr. Worawat Meevasana)

Dean of Institute of Science

สุภาวี ชัยสิทธิ์ : การสังเคราะห์และคุณสมบัติทางเคมีไฟฟ้าของถ่านกัมมันต์จากแป้งมัน
สำปะหลัง สำหรับประยุกต์ใช้ในระบบกักเก็บพลังงาน (SYNTHESIS AND
ELECTRO CHEMICAL PROPERTIES OF ACTIVATED CARBON FROM CASSAVA
STARCH FOR ENERGY STORAGE APPLICATIONS). อาจารย์ที่ปรึกษา : ศาสตราจารย์
ดร.สันติ แม้นศิริ, 117 หน้า.

คุณสมบัติทางเคมีไฟฟ้า/แป้งมันสำปะหลัง/ถ่านกัมมันต์/การกักเก็บพลังงาน

    ถ่านกัมมันต์จากแป้งมันสำปะหลัง โดยใช้เทคนิคการกระตุ้นทางเคมีด้วยโพแทสเซียม
ไฮดรอกไซด์ ทำการเผา (carbonization) เพื่อให้เกิดรูพรุนโดยประกอบด้วยสองขั้นตอนคือ
แอคติเวชัน (activation) และ คาร์บอไนเซชัน (carbonization) ตรวจสอบสมบัติทาง สัณฐานวิทยา
หมู่ฟังก์ชันทางเคมีเชิงพื้นผิว โครงสร้างเชิงผลึก สมบัติความพรุนและสถานะทางเคมีของสาร
ตัวอย่างโดยใช้เทคนิคการเลี้ยวเบนของรังสีเอ็กซ์ (XRD) กล้องจุลทรรศน์แบบส่องกราด (SEM)
เทคนิคการวิเคราะห์หาค่าพื้นที่ผิวของสาร (BET) ฟูเรียร์ทรานสฟอร์มอินฟราเรด (FTIR) และ
เทคนิคโฟโตอิมิชชัน (XPS) ตามลำดับ ได้ศึกษาสมบัติทางไฟฟ้าเคมีของขั้วไฟฟ้า (Electrochemical
properties) ที่เตรียมจากวัสดุถ่านกัมมันต์ที่ประดิษฐ์ด้วยเทคนิคคือ โวลแทมเมตรี (CV) การประจุ
ที่กระแสคงที่ (GCD) และ อิเล็กโทรเคมิคัลอิมพีแดนซ์สเปกโทรสโกปี (EIS) ถ่านกัมมันต์ที่เตรียม
ได้มีขนาดรูพรุนเท่ากับ 1.76 - 2.20 นาโนเมตร มีปริมาตรรูพรุนสูงเท่ากับ 6.7 ลูกบาศก์เซนติเมตร
ต่อกรัม จากการวัดการดูดซับก๊าซไนโตรเจนพบว่าถ่านกัมมันต์มีพื้นที่ผิวจำเพาะสูงสุดคือ 2,047
ตารางเมตรต่อกรัม และค่าปริมาตรรูพรุนสูงสุดเท่ากับ 1.02 ลูกบาศก์เซนติเมตรต่อกรัม การศึกษา
สมบัติเชิงเคมีไฟฟ้าของขั้วไฟฟ้าได้แสดงให้เห็นถึงกลไกการเก็บพลังงานที่เตรียมขึ้นพบว่ามี
รูปแบบการเก็บประจุแบบการเก็บแบบประจุไฟฟ้าสองชั้น (EDLC) ของถ่านกัมมันต์นี้ ค่าการเก็บ
ประจุจำเพาะของขั้วไฟฟ้ามีค่าการเก็บประจุเท่ากับ 129 ฟารัดต่อกรัมที่ 2 แอมแปร์ต่อกรัม
นอกจากนี้ขั้วไฟฟ้ายังมีการเก็บประจุร้อยละ 95 ในการทดลองประจุซ้ำจำนวน 1,000 รอบ หลังจาก
การอัด-การคายประจุ

การกระตุ้นทางเคมีและอุณหภูมิการเผาของคาร์บอนสามารถปรับปรุงค่าการเก็บประจุจำเพาะของ
ถ่านกัมมันต์ได้

สาขาวิชาฟิสิกส์

ปีการศึกษา 2561

ลายมือชื่อนักศึกษา_____

ลายมือชื่ออาจารย์ที่ปรึกษา_____

ลายมือชื่ออาจารย์ที่ปรึกษาร่วม_____

SUPHAWI CHAISIT : SYNTHESIS AND ELECTROCHEMICAL PROPERTIES OF ACTIVATED CARBON FROM CASSAVA STARCH FOR ENERGY STORAGE APPLICATION. THESIS ADVISOR : PROF. SANTI MAENSIRI, D.Phil. 117 PP.

ELECTROCHEMICAL PROPERTIES/CASSAVA STARCH/ACTIVATED CARBON/ENERGY STORAGE

Activated carbon derived from cassava starch was fabricated by chemical activation of potassium hydroxide. The samples were carbonized to create pore structure using two steps of activation and carbonization. The morphology, surface functional chemistry, microstructure, crystallinity, chemical state and porosity of the sample were investigated by X-ray diffraction (XRD), Scanning electron microscopy (SEM), Fourier-transform infrared spectroscopy (FTIR), X-ray photoemission spectroscopy (XPS) and Brunauer-emmett teller (BET) techniques. The electrochemical properties of the sample were studied by using Cyclic voltammetry (CV), Galvanostatic charge discharge (GCD) and Electrochemical impedance spectroscopy (EIS). The activated carbon has micro pore average size between 1.76-2.20 nm and high pore volume of 6.7 $cm^3 g^{-1}$. N_2 isotherm measurement of the samples revealed the highest surface area of 2047 $m^2 g^{-1}$ and highest total pore volume of 1.02 $cm^3 g^{-1}$ for activated carbon. The studying of electrochemical properties of the activated carbon electrode revealed the energy storage mechanism of EDLC behavior. The specific capacitance of the electrode is 129 $F g^{-1}$. The activation and carbonization temperature can improve the specific capacitance of the activated carbon.

Moreover, the electrode showed the imposing cycling capacity retention more than 95 % at 1000 cycles after charge-discharge.

School of Physics

Academic Year 2018

Student' s Signature_____

Advisor's Signature_____

Co-Advisor's Signature_____

ACKNOWLEDGMENT

Suphawi Chaisit

CONTENS

CONTENS (Continued)

CONTENS (Continued)

CONTENS (Continued)

CONTENS (Continued)

CONTENS (Continued)

LIST OF TABLES

LIST OF TABLES (Continued)

LIST OF FIGURES

LIST OF FIGURES (Continued)

LIST OF FIGURES (Continued)

LIST OF FIGURES (Continued)

LIST OF FIGURES (Continued)

LIST OF ABBREVIATIONS

ADS	Adsorption isotherm
BET	Brunauer-Emmett-Teller method
BJH	Berrett-Joyner-Halenda method
CV	Cyclic voltammetry
DES	Desorption isotherm
EDLC	Electrical double layer capacitor
EIS	Electrochemical impedance spectroscopy
FTIR	X-ray photoemission spectroscopy
GCD	Galvanostatic charge /discharge
IUPAC	The International Union of Pure and Applied Chemistry
SC	Supercapacitor
SEM	Scanning electron microscopy
XPS	X-Ray Photoemission spectroscopy
XRD	X-ray diffraction

CHAPTER I

INTRODUCTION

1.1 Background and motivation

In recent years, there has been an enormous increase in the global demand for energy. The energy sources used at a certain time and place. Our severe dependency on oil and electricity makes energy a vital component of our daily life. World population Continued to grow, and statistical analysis predicts that by the year 2050, it will be increased by 30% of today population. Energy consumption rate of our planet would be accelerated to an alarming rate of 34% by 2050, which will demand fossil fuel and non-renewable sources such as oil, gas and coal (Zhang *et al.*, 2011; Kim and Kim, 2006). Energy demand accompanied by downfall in conventional energy sources, which is associated with a myriad of environmental issues and their very impact on life, grew a worldwide consensus on clean energy.

Energy storage is a widespread subject of interest to scientists, engineers, technologists worldwide. The Electrochemical technology for energy storage and conversion devices such as rechargeable batteries, supercapacitors and fuel cells has been gaining momentum to overcome the huge gap present between energy supply and energy demand.
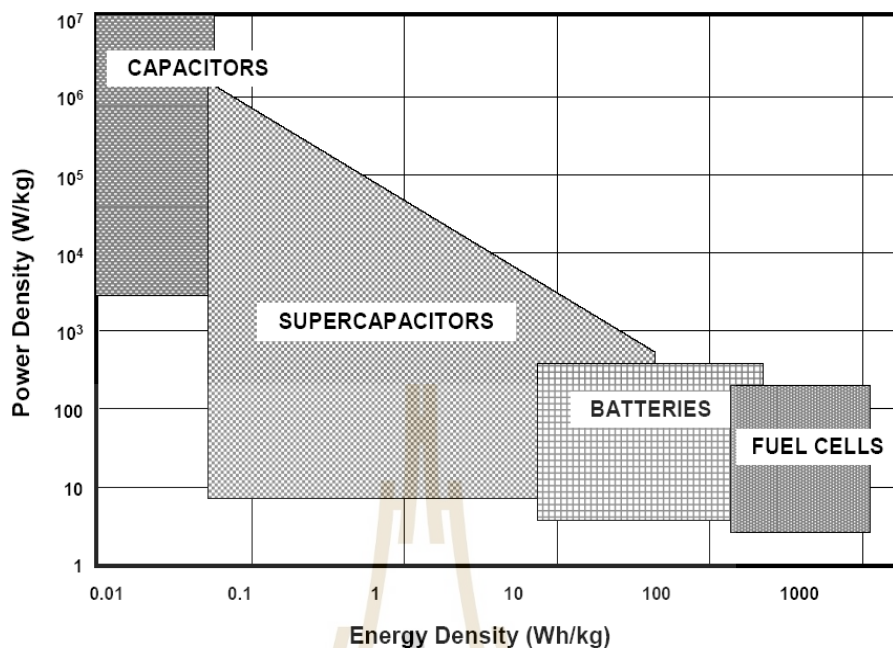
Figure 1.1 Ragone plot of energy density vs. power density for various energy-storing devices (Kötz and Carlen, 2000).

In figure 1.1, ragone plot of power density vs. energy densities is shown for the most significant energy storage and conversion system at present. Each system plays a unique role, with their respective abilities to store and deliver energy illustrated by their governing area (Kötz and Carlen, 2000). Advanced Li ion secondary batteries have been produced with high energy densities reaching 180 Wh kg^{-1}, but these show a lower power density performance (Simon and Gogotsi, 2008). Capacitors have many advantages over batteries: they weigh less, generally don't contain harmful chemicals or toxic metals, and they can be charged and discharged zillions of times without ever wearing out. Electrochemical capacitors (ECs), also known as supercapacitors that bridge the gap between capacitors and batteries/fuel cells, they have a number of key attitude such as the characteristic ability to discharge and recharge stored energy within

seconds, near limitless recyclability with a typical cycle life compared with batteries and higher energy density than conventional dielectric capacitors, environmental friendliness, low maintenance cost and operation over a wide temperature range (Conway, 2013).

In general, supercapacitors can be classified into three types by the charge mechanism of their respective active material used for electrode construction such as electrical double-layer capacitors (EDLCs), pseudocapacitors and a battery-like asymmetric hybrid configuration. Many carbon materials, such as porous carbon (Zhou *et al.*, 2012) and graphene (Fan *et al.*, 2012) are developed for the EDLCs. However, the EDLCs usually have low energy density. The energy density of pseudocapacitors is usually many times greater than EDLCs. In addition to the construction of supercapacitor consist of three components electrode, electrolyte, and separator. In the characteristic of electrode material, that is high conductivity, high surface, good corrosion resistance, high-temperature stability and low-cost. (Kalyani and Anitha, 2013).

So, my work mainly focuses on the electrode material with the high surface area and low cost. In order to improve their capacitor value by carbon activation due to the surface area of electrode material is an important parameter in EDLDs. Generally, there are two methods for preparation of activated carbon. By using physical activation and activation. Comparing physical activation with chemical giving the higher of specific capacitance (Gao *et al.*, 2017). In this work, the activated carbon was prepared from cassava starch by using chemical activation with a different concentration ratio of chemical agent: raw material. And in different carbonization temperatures. The obtained activated carbon was studied by techniques such as differential scanning

calorimetric method (DSC), scanning electron microscopy (SEM), transmission electron microscopy (TEM), X-ray diffraction (XRD), Brunauer–Emmett–Teller method (BET) and X-ray photoemission spectroscopy (XPS). The activated carbon electrodes were investigated electrochemical properties by cyclic voltammetry (CV), Galvanostatic Charge Discharge (GCD) and electrochemical impedance spectroscopy (EIS).

1.2 Objective of the research

In this work, we aim to study electrochemical properties of activated carbon from cassava starch for supercapacitor electrode applications. The objectives are listed as follows.

1.2.1 To enhance supercapacitor electrodes by chemical activation (KOH) derived carbon material from cassava starch and annealing temperature under argon atmosphere.

1.2.2 To study effect of the impregnation ratios between raw material and activation regent (KOH) and carbonization temperature (600, 700 and 800 ºC).

1.2.3 To study pore structures and surface area of the activated carbon by using BET measurement.

1.2.4 To improve surface area and electrochemical properties of activated carbon electrode by chemical activation method.

1.3 Scope of study

1.3.1 This work focuses on the activated carbon derived from cassava starch by 6 M potassium hydroxide (KOH) activation.

1.3.2 Study of effect of the carbonization temperature on the physical and electrochemical properties at 400 $^{\circ}$C for non-activated carbon   and 600, 700, 800 $^{\circ}$C for activated carbon.

1.3.3 The morphology, the pore structure, and the electrochemical performance of the activated carbon by KOH activation are compared.

1.4 Location

Advanced Material Physics Laboratory (AMP), School of Physics, Institute of Science, Suranaree University of Technology, Nakhon Ratchasima, Thailand.

1.5 Anticipated outcomes

1.5.1 Acquirement of skills in the activated carbon derived from cassava starch.

1.5.2 Skills in the characterization of activated carbon.

1.5.3 Understanding of the electrochemical performance of the activated carbon derived from cassava starch.

1.5.4 Publication in International ISI journals.

1.6 Outline of thesis

This thesis is divided into five chapter. The first chapter is the introduction of the thesis. Chapter II describes a brief literature review of information concerning the structure, synthesis method, and potential applications of activated carbon derived from cassava starch. Furthermore, the theory approach concerning the physical and electrochemical properties are also described in this section. Chapter III, the preparation and characterization method of activated carbon are described. Chapter IV present is the experimental results and discussion. Lastly, the conclusions and recommendations of this thesis are given in Chapter V.
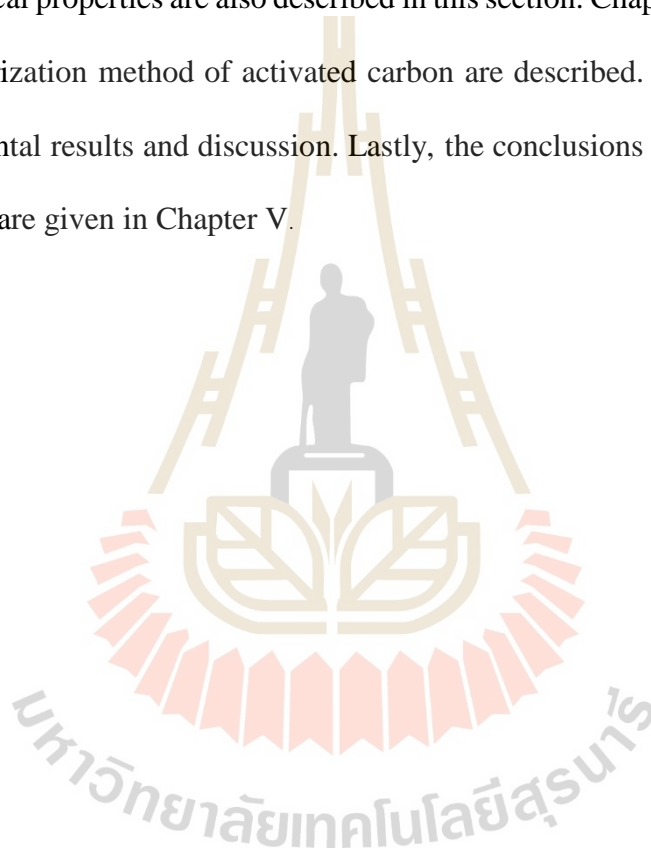
CHAPTER II

LITERATURE REVIEWS

2.1 Capacitor

2.1.1 Working principle of capacitor

A capacitor is store energy in an electrostatic field. It is component of two parallel electrodes (Plate) and dielectric separated between two parallel. The capacitor has a positive and negative charge to exchange between surfaces of electrodes of across polarity. That can be occur by applying potential difference to electrode. When the charge in a capacitor connected a circuit. The voltage source will be action for short time. It is capacitance (C) in unit of farads. There is the ratio of electric charge on electrode (Q) to the difference of potential opposite electrode.

$$C = \frac{Q}{V} \qquad (2.1)$$

For a conventional capacitor, C is proportional to area (A) of each electrode and the permittivity (ε) of the dielectric is inversely proportional to distance (D) between the electrode so that.

$$C = A \frac{\varepsilon_r \, \varepsilon_0}{D} \qquad (2.2)$$

Where ε_0 is permittivity of free space, ε_r is dielectric constant (or relative permittivity) of the material between the plates. However, there are three main parameter that the determine capacitance. This following:

- Plate area (common to the two electrodes)

- Separation distance between the electrode

- Properties of dielectric used (Lu, 2013)

Conductive Plates
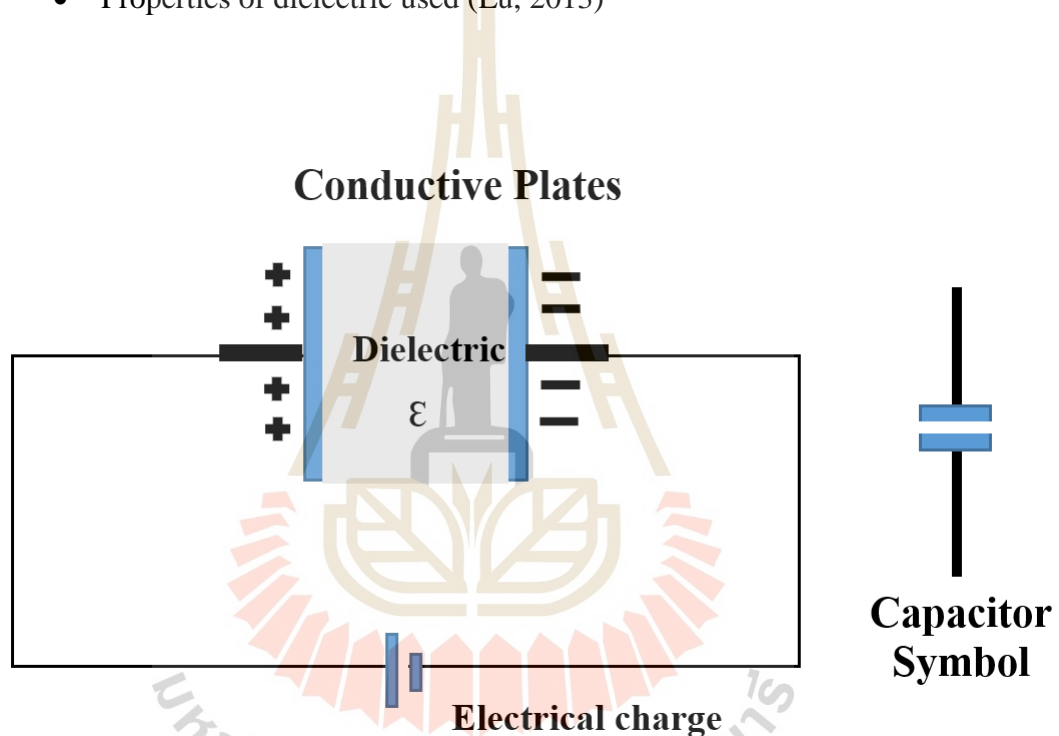
Figure 2.1 Schematic diagram of a conventional capacitor.

However, the conventional capacitor can be storing little energy because it's limitation charge storage area and separate distance between the two charged plates. Therefore, a new generation was improvement based on the electrical double layer capacitive as the supercapacitors.

2.2 Supercapacitor

In the few centuries later, the scientist known and understood with the subject of capacitor. It is in conventional capacitor for the energy stored. This a given by:

$$E = \frac{1}{2} CV^2 \qquad (2.3)$$

Where E is the energy store, C is the capacitance and V is the applied voltage and power of supercapacitors are calculated according to:

$$P = \frac{V^2}{4R} \qquad (2.4)$$

Where C is the dc capacitance in Farads, V is the nominal voltage and R is the equivalent series resistance (ESR) in ohms (Pandolfo and Hollenkamp, 2006). Convention capacitor have specific capacitance in order ranging to pF to $\mu F\ cm^{-2}$ (Chandra, 2012).

In order to specific capacitance will be increasing more than 4-5 order of magnitude (Simon and Gogotsi, 2010). However, the innovation concept for developing capacitor with specific capacitance by required. In order to c~50 to $500\ F\ g^{-1}$ with weight and small volume (Chmiola *et al.*, 2006; Conway, 2013; Pushparaj *et al.*, 2007; Sung *et al.*, 2006). The concept of value capacitance increase magnitude in order supercapacitor are the term as supercapacitor. It is the large capacitance value. Although, the internationally no accepted definition for supercapacitor the can be broadly defined as following. The supercapacitor is electrochemical energy storage like a kind of batteries. (Gao *et al.*, 2017; Zhu *et al.*, 2011). Electrochemical capacitor can be storing as highly amount of energy and energy at rates demanded specific capacitance by the application.

However, the supercapacitor is not limitation to electrochemical charge transfer kinetic of batteries and there are work at high charge and discharge rates and can have a lifetime of over a million cycles with contrary to batteries (Zhu *et al.*, 2011).

Supercapacitors have energy density lower than lithium-ion batteries, In addition, they have a long life cycle and they have higher power density, high cycle ability, and low safety when compared to secondary batteries (Enock *et al.*, 2017). This research is focused on the maximum of energy density and low-cost electrode materials made so far for supercapacitor electrode. Generally, supercapacitors can be classified into 3 types based on charge storage mechanism. That are double –layer capacitor, pseudo capacitor, and hybrid capacitor as show figure 2.2.
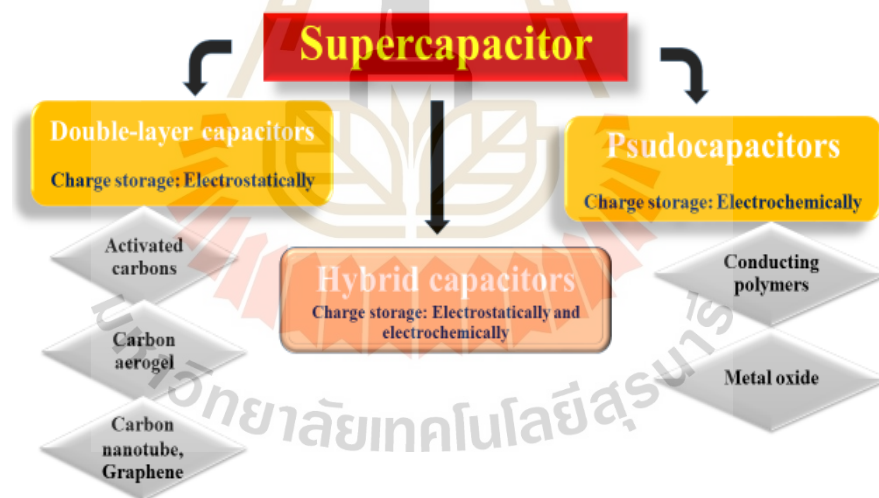
Figure 2.2 Taxonomy of electrochemical capacitors (Adapted from (Shukla *et al.*, 2012)).

In a supercapacitor, there do not use the solid dielectric of the capacitor. Their uses activated carbon electrode, a separator can be ions to pass through and an electrolyte for transfer ion between electrodes (Enock *et al.*, 2017). Both positive and negative of the electrode were made up of like material. Double layer charging effect is predominated by the charge storage mechanism in supercapacitors. So, it is known that material is the important factor for doing of the supercapacitor. Electrode material in supercapacitor divide three main of categories, carbon-based, transition metal oxides and conducting polymer. Activated carbon is one of carbon-based material was interested in the investigation of electrode material in supercapacitors because of the high surface area and high porosity that support good charge accumulation at the interface with the electrolyte (Kalyani and Anitha, 2013). Therefore, it can be high capacitance on the system. A schematic view of the capacitor is shown in Figure 2.3.
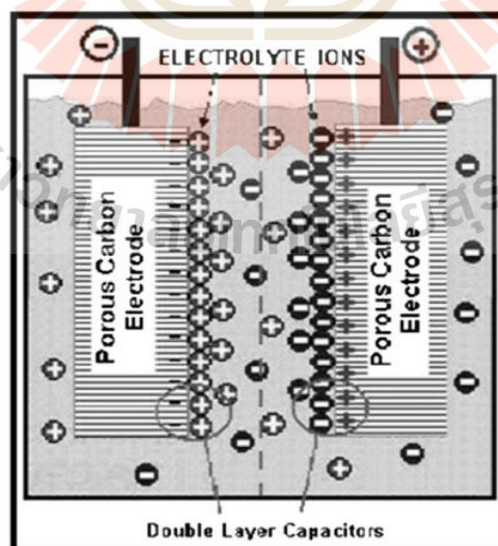
Figure 2.3 Schematic view of electrical double layer capacitor. (Kalyani and Anitha, 2013).

2.3 Electrostatic Double layer capacitor

The electrostatic double-layer capacitor is one of the classification supercapacitors use store charge electrostatically principle. My research work focuses on activated carbon material electrode for the electrostatic double-layer capacitor. Every electrochemical capacitor has two electrodes, mechanically separated by a separator, which are electrically connected to each other via the electrolyte. The electrolyte is a mixture of positive and negative ions dissolved in a solvent. An area originates at each of the two electrodes surfaces where the liquid electrolyte contacts the conductive metallic surface of the electrode. This interface forms a common boundary between two different phases of matter such as an insoluble solid electrode surface and an adjacent liquid electrolyte. By applying a voltage, both electrodes generate two layers of polarized ions. One layer of ions is in the surface lattice structure of the electrode. The other layer, with opposite polarity, originates from dissolved and solvated ions distributed in the electrolyte and has moved in direction of the polarized electrode. A structure of an ideal double-layer capacitor is shown in Figure 2.4.
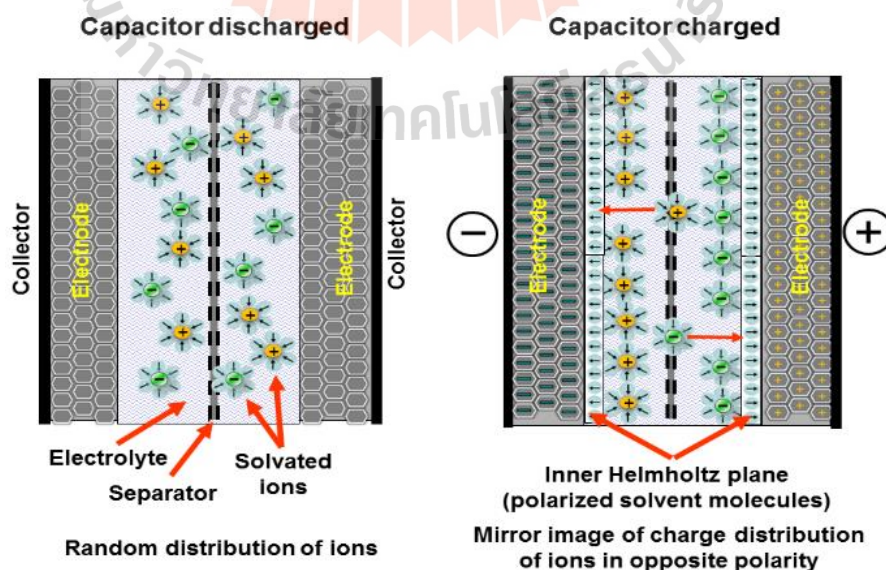
Figure 2.4 Structure of an ideal double-layer capacitor (Beback *et al*., 2011).

During the charging process, one of an electrode is positive and another is negative. The ions in electrolyte are dissociated by attractive force and then move to accumulate close to the interface between electrolyte and each electrode and then form the double layer structure which is in the range of 2-10 Å. This is the charged process. When the supercapacitor is discharged the ions move away from the electrodes and then generate the energy (Zhang *et al*., 2011).

2.4 Activated carbon for electrode material

There are two methods for preparation of activated carbon. The first method of physical activation involves carbonized under an inert atmosphere (CO_2, N_2, Ar or a mixture of these) and high temperature using either steam (Kalyani *et al*., 2013). The physical activation has two-step on a process, generally, the researcher uses CO_2 gas for activation process because it is clean, easy to handle and facilitates control of activation process due to the slow reaction a temperature around 800 ^{o}C. Carbonization temperature has ranged between 400 ^{o}C and 850 ^{o}C and activation temperature range between 600 ^{o}C and 900 ^{o}C (Ioannidou and Zabaniotou, 2007). The chemical activation method treated impregnation of precursor with a chemical such as KOH, $ZnCl_2$ and H_2SO_4 (Kalyani and Anitha, 2013). In addition, this method was prepared in a single step at ~ 700 to ~ 1200 K combining the carbonization and activation. The porous carbon material from chemical activation is a high specific surface area (> 2000 $m^2 g^{-1}$) and large pore volume which compares physical activation (Gao *et al*., 2017). The activated carbon, in the study of Kalyani et al. Which was chemical activation with KOH of fire wood material, compares physical activation with steam in the $NaNO_3$

electrolyte. Show in table 2.1. As can be observed specific capacitance of KOH activation has value more than steam of physical activation.

Table 2.1 Comparing of physical activation with steam in the $NaNO_3$ electrolyte and Chemical activation with KOH (Rufford *et al.*, 2010).

Biomass material	Activating agent	Electrolyte	BET surface area ($m^2\,g^{-1}$)	Specific capacitance ($F\,g^{-1}$)
Bamboo	Steam	Non-aqueous	445-1025	5-60
	KOH	Et_4NBF_4	1413	15-65
Fir Wood	Steam	$NaNO_3$	1016	89
		HNO_3		120
		H_2SO_4		96
Fir Wood	KOH	$NaNO_3$	2821	165
	$KOH + CO_2$	H_2SO_4		197

In 2010, Rufford *et al.* Studies activated carbon for supercapacitor electrode. Sugarcane bagasse was prepared by chemical activation with $ZnCl_2$. In addition, prototype of supercapacitor was fabricated sandwich-type supercapacitor cells containing 1 M H_2SO_4. The sugarcane bagasse carbons are specific energy up to 10 Wh kg^{-1} and specific capacitance to 300 F s^{-1} (Rufford *et al.*, 2010). So, my research studies chemical activation with KOH due to there is exhibit high specific capacitance and high pore structure are shown in table 2.2. However, Specific capacitance and pore structure depended on the effect of carbonization temperature and chemical ratio activation.
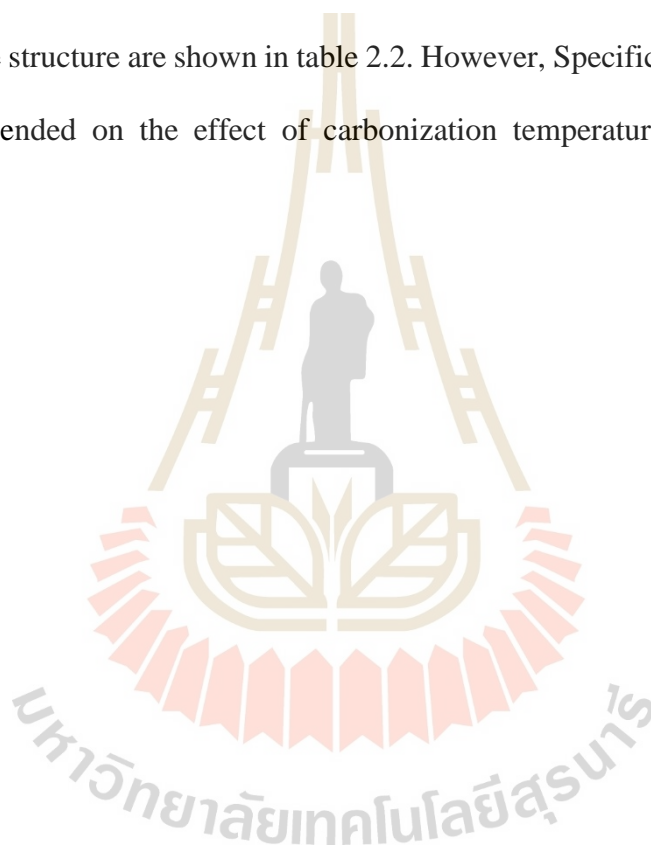
Table 2.2 Survey of activated carbons from biomass precursors for electrode materials in supercapacitors. (Rufford *et al.*, 2010).

Carbon source	Activation method	S_{BET} ($m^2\,g^{-1}$)	Capacitance ($F\,g^{-1}$)	Electrolyte
Sugar cane bagasse	NaOH	2871	109	1 M H_2SO_4
Banana fibers	KOH	686	264	1 M Na_2SO_4
Fir wood	KOH	1064	180	0.5 M H_2SO_4
Fir wood	Steam	1016	110	0.5 M H_2SO_4
Seaweed biopolymer	Thermal	273	198	1 M H_2SO_4
Corn gain	KOH	3199	257	6 M KOH

2.5 Electrochemical properties of chemical activation

Electrochemical properties of activated carbon significantly investigate the specific capacitance, lead to improvement and development of supercapacitor application. In 2008, studies production of activated carbon from bagasse and rice husk. Comparing, Three chemical reagents with $ZnCl_2$, NaOH and H_3PO_4 under evaluation only for temperature 600, 700 and 800 ^{o}C. The $ZnCl_2$ produced activated carbon had the highest surface area when comparing three reagents. The carbon produced from $ZnCl_2$ chemical agent at optimum activation temperature with 700 ^{o}C had a surface area of 674 $m^2\,g^{-1}$ about bagasse and 750 $m^2\,g^{-1}$ of rice husk (Kalderis *et al.*, 2008). At the high temperature, surface area decreasing, lead to increasing time had a negative effect on the development of the surface area probably because the pore from the formation had a blocking (Elmouwahidi *et al.*, 2012). Studies activated carbon from KOH-activation of organ seed shells. The three-electrode cell using 1 M H_2SO_4 were fabricated for electrochemical measurement. The activated carbon had the lowest capacitance (259 F g^{-1} at 125 mA g^{-1}) and lowest capacity retention (52 % at 1 A g^{-1}), because of surface carboxyl groups electrolyte diffusion into pore (Farma *et al.*, 2013). Study of highly porous binder less activated carbon electrodes from fiber of oil palm empty fruit bunches, the activated carbon was prepared by KOH activation and N_2-carbonization. The high surface area had 1704 $m^2\,g^{-1}$ and total pore volume had 0.889 $cm^3\,g^{-1}$. In addition, Specific energy and specific power of 150 F g^{-1} and 173 Wk g^{-1}, respectively. In 2015, Ma et al. studies nitrogen-doped porous carbon derived from biomass waste. Zinc chloride was activated for potato waste by nitrogen-doped carbon. The surface area of activated carbon at 700 ^{o}C carbonization had a value of 1052 $m^2\,g^{-1}$. Specific capacitance is 225 F g^{-1} in 2 M KOH electrolyte.

The electrode material had good cycle ability with 93.7 % at 5 A g^{-1} for 5000 cycles. In my research mainly focus on the development of electrode material with a high surface area, high specific capacitance and low-cost. Thus, this work interested in activated carbon by chemical activation, and effect of occurring pore structure of activated carbon product.

CHAPTER III

RESERCH METHODOLOGY

The experimental process of research, in order to investigating the characterization and electrochemical properties of activated carbon derived from cassava starch. The activated carbon from is very interesting for using as supercapacitor electrode material because of first study and adding value to agricultural product. The activated carbon prepared by potassium hydroxide (KOH) at differential impregnation ratio by carbonization at 600 $^{\circ}$C, 700 $^{\circ}$C and 800 $^{\circ}$C in argon flowing for 2 h. The characterization of the sample was done by various techniques to understand thermal stability, morphology, microstructure, and porosity using the X-ray diffraction (XRD), Scanning electron microscope (SEM), Brunauer-emmett-teller (BET), Fourier transform infrared spectroscopy (FTIR) and X-ray photoemission spectroscopy (XPS). Finally, in part of understanding the electrochemical properties as sample are also included in this chapter.

3.1 Material

- Cassava root

- Potassium hydroxide (KOH)

- Sodium hydroxide (NaOH)

- Hydrochloric acid (HCl)

- Deionized water (DI, Synchrotron light research institute)

- Carbon black

- Activated carbon

3.2 Apparatus

- Stainless furnace tube

- Electrochemical station (AUTOLAB-PGSTAT302N, Netherlands)

- Hot plate and Magnetic stirrer (IKA, C-MAG HS7)

- Hydraulic presser

- Argon tank

3.3 Preparation of activated carbon

In this study, the activated carbon prepared by chemical activation process of potassium hydroxide impregnation at different impregnation with non-activated carbon: KOH (1:1, 1:3 and 1:5 respectively) ratio by carbonization at 600, 700, 800 °C in the horizontal tubular furnace. The carbonization was performed under argon flow. The activated carbon was washed by HCl solution until the pH of reach 7 and was dried overnight. After that the obtained activated carbons were studied activated carbon characterize and electrochemical properties. The preparation process is shown in Figure 3.1.
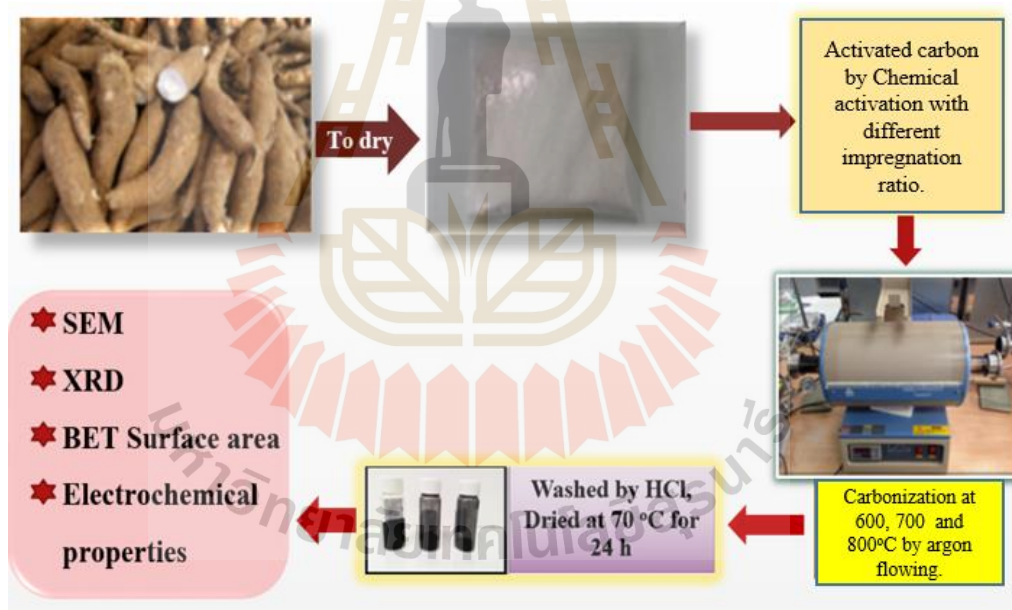
Figure 3.1 The preparation of activated process.

3.4 Characterizations of the activated carbon

The structures of the prepared activated carbon were evaluated by X-ray diffraction (Bruker D2 Phaser ceramic Cu X-ray tube, 30 kV/10 mA with X-ray source, 1-D (LYNXEYE) detector)). The chemical compositions were analyzed by X-ray photoelectron spectroscopy (PHI5000 VersaProbe II, ULVAC-PHI: monochromatic Al Kα excitation source (1486.6 eV)). The surface morphologies were investigated using scanning electronmicroscopy (SEM: JEOL JSM-6010LV, Magnification 8x-300,000x, SE detector, Everhart-thornley type). The surface area and pore size distribution were analyzed by Brunauer-Emmett-Teller (BET: BELSORP Mini II, Japan) technique. The samples were degassed at 300 ºC for 12 h and then analyzed for nitrogen absorption at 77 K. Adsorption isotherm was used to study the characteristics of the pore of this samples. The pore size distributions were analyzed by using the Barrett-Joyner-Halenda method (BJH) was employed to determine the pore character of the sample.

3.5 Electrode preparation and electrochemical characterization

The activated carbon was prepared as an active material for an electrode of electrochemical capacitor. The activated carbon (8 mg), acetylene black (1 mg), polyvinylidene fluoride (1 mg), 1-methyl-2-pyrrolidinone (200 ml) were mixed and coated on Ni foam as an electrode. The prepared electrodes were dried in oven at 70 ºC for 1 day and then were pressed at 20 MPa. The electrochemical performance of the prepared electrodes was evaluated by a three electrodes system. The system consists of counting electrode (CE), reference electrode (RE) and working electrode (WE) of the electrochemical cell tested in 6M of KOH solution. Cyclic voltammetry (CV) curves of

the electrodes were evaluated by using potentionstat method at the scan rates of 2 mV s^{-1},5 mV s^{-1}, 10 mV s^{-1}, 20 mV s^{-1} and 30 mV s^{-1}and voltages between -1.2 V to 0 V. Galvanostatic charge-discharge (CD) curves were measured at current densities of 2 A g^{-1} to 200 A g^{-1}. Electrochemical impedance spectroscopy (EIS) was performed under the frequency range between 100 kHz and 100 mHz in order to study the electrical circuit of performed electrodes. The specific capacitance, energy density, and power density are calculated by the following equations (Chen *et al.*, 2014).

$$C = (I \times \Delta t)/(\Delta V \times m) \tag{3.1}$$

$$E = \left[C \times \left(\Delta V^2 \right) \right]/2 \tag{3.2}$$

$$P = E/t \tag{3.3}$$

Where C is specific capacitance (F g^{-1}), E is energy density (Wh kg^{-1}), P is power density (KW kg^{-1}), I is discharge current (A), t is the discharge time(s), ΔV is potential window (V) and m is the mass of active materials (g). However, we can see the process experimental followed by figure 3.2.
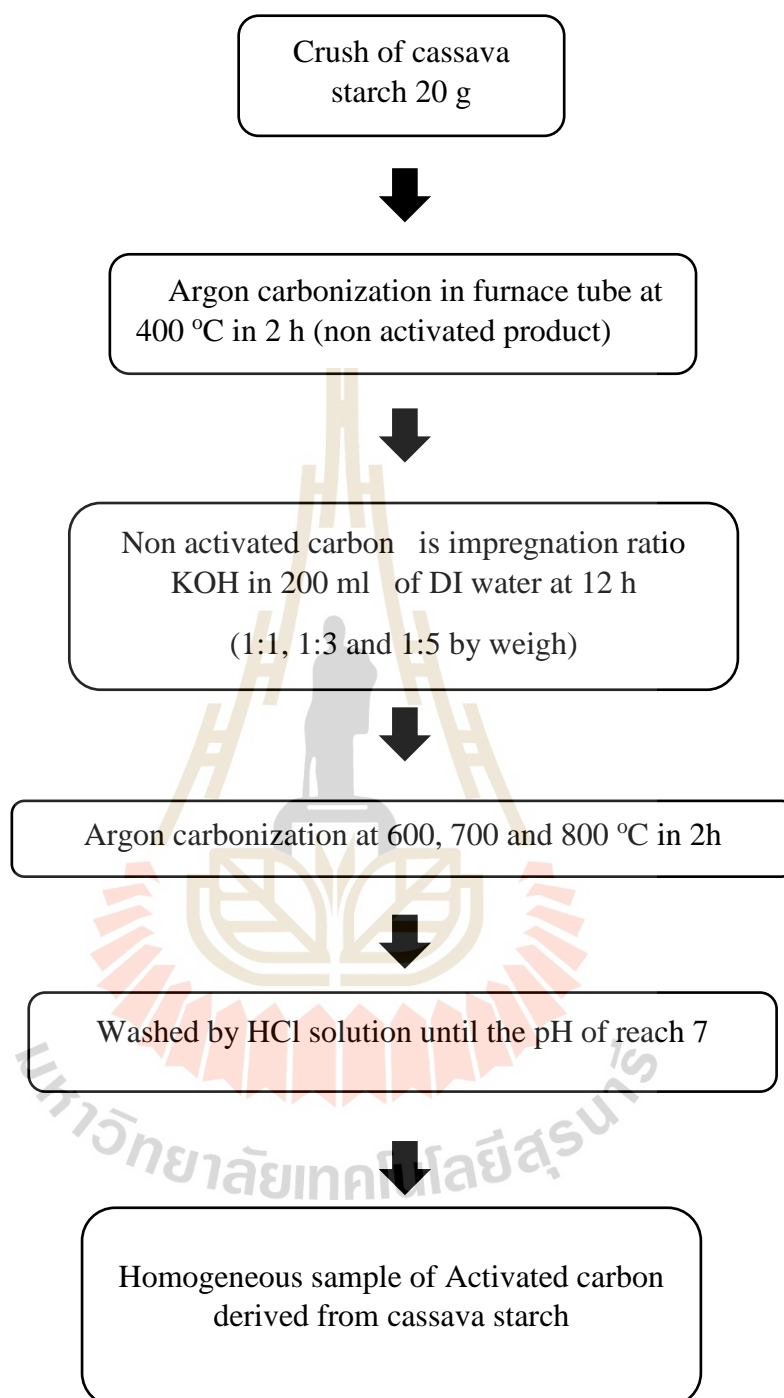
Figure 3.2 Diagram showing the preparation of activated carbon derived from cassava starch.

3.6 Basic characterization

3.6.1 Thermal geography analysis and differential scanning calorimeter (TGA-DSC) is used to study thermal responsive of cassava starch for proportional temperature use. All products will be heated from room temperature up to 1000 $^{\circ}$C, by heating rate 5 $^{\circ}$C min^{-1} in nitrogen.

3.6.2 The morphologies of the activated carbon are examined by scanning electron microscopy (SEM), and transmission electron microscopy (TEM).

3.6.3 The structure of synthesized activated carbon is evaluated by X-ray Diffraction (XRD).

3.6.4 XPS can be used to analyze the surface chemistry of a material.

3.6.5 Surface area and pore size distribution are analyzed by BET surface area. The samples were first degassed at 300 $^{\circ}$C, for 12 h and then analyzed for nitrogen absorption. Adsorption isotherms are used to calculate the specific surface area through application of the BET model, while the total pore volume and pore size distributions are calculated by using the BJH method.

3.6.6 Study of electrochemical properties three electrodes system consisting of counting electrode (CE), reference electrode (RE) and working electrode (WE) of electrochemical cell. Cyclic voltammetry (CV) curve of the electrodes is performed by using potential stat method. Galvanostatic charge-discharge (CD) is used to study performance of the electrodes at current densities. Electrochemical impedance spectroscopy (EIS) is performed under the frequency range between 100 kHz and 100 MHz in order to study the electrical circuit of performed electrodes.

3.7 Instrumentations

3.5.1 High current potentiostat/galvanostat system (AUTOLAB PGSTAT302N, Netherlands).

3.5.1 Thermogravimetric/Differential Thermal Analyzer (TG-DTA)

3.5.2 Scanning electron microscope (SEM, JSM-6010 LV, USA)

3.5.3 BELSORP-mini system (BELSORP Mini II, Japan)

3.5.4 X-ray diffraction (XRD)

3.5.5 X-ray photoemission spectroscopy (XPS) beam line (BL8)

3.8 Location of research

3.8.1 SUT COE on Advanced Functional Materials (AFM), School of Physics, Suranaree University of Technology, Nakhon Ratchasima, Thailand.

3.8.2 The Center for Scientific and Technological Equipment, SUT.

3.8.3 Synchrotron Light Research Institute (Public Organization)

3.9 Material characterization

3.9.1 X-ray diffraction (XRD)

X-ray diffraction is technique to discover the crystal structure of materials (Leng, 2009). This technique uses the basic of interference phenomenon of wave. There are wavelength and traveling in the like a direction to the sample. X-ray beams incident on a crystalline solid will be diffracted by the crystallographic planes as illustrated in Figure 3.3. The constructive and destructive interferences occur if a phase difference is $n\lambda$ (in phase) and $n\lambda/2$ (out of phase). Two in-phase incident waves, with beam 1 and

beam 2, are deflected by two crystal planes. The deflected wave related Bragg law equation this following:

$$2d\sin\theta = n\lambda \qquad (3.4)$$

Where d is the spacing between the parallel crystal planes, θ is the angle of incident beam, λ is the wavelength of the incident X-ray beam and n is an integer. The diffractometer records changes of diffraction intensity with 2θ. An intensity peaks located at different 2θ provide a 'fingerprint' for a crystalline solid. Identification of crystalline substance and crystalline phases in a specimen is achieved by comparing the specimen diffraction spectrum with spectra of known crystalline substances.
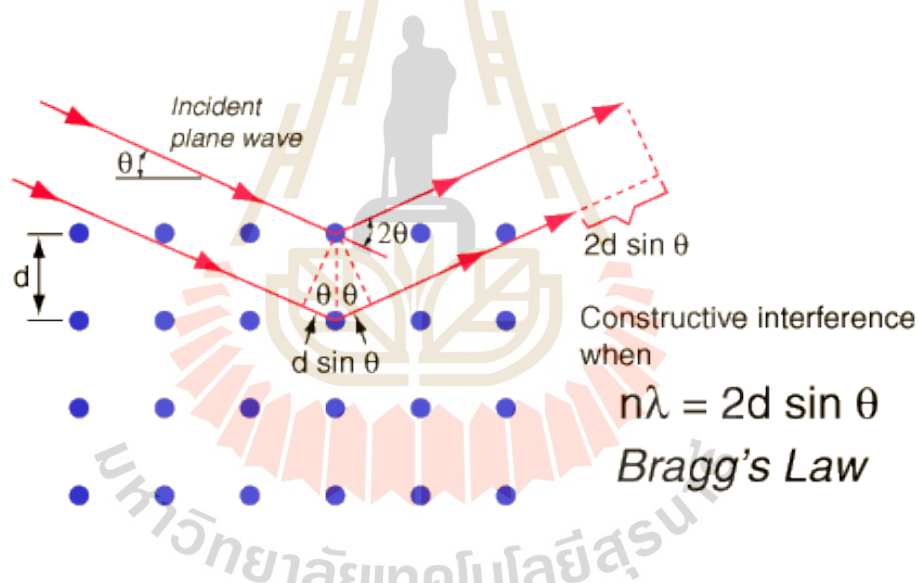
Figure 3.3 Bragg diffraction by crystal planes (Adapted from (Leng, 2009).

In this work, the phase and structure analysis of the activated carbon was carried out by X-ray diffraction (XRD; D2 Advance Bruker) with Cu Kα at $\lambda = 0.15406$ nm as shown in Figure 3.3. The XRD pattern were recorded in the 2θ of $10\,^{\circ}$ - $90\,^{\circ}$ with the time step of 0.5 and the step size of 0.02. The crystalline phase identification was carried out by comparison with the Joint Committee on Powder Diffraction Standards (JCPDS) diffraction files.

3.9.2 Scanning electron microscopy (SEM)

Scanning electron microscopy (SEM) is scanning the surface of material technique for observe microscopic structure (Leng, 2009). This technique uses electron beam to scan surface with sample specimen (Ni, 2013) as shown in Figure 3.4. The electron beam was focused for specimen irradiated created useful images explained the surface morphology of specimen. The SEM operates under a vacuum, and electrons produced by a field emission source are accelerated in a field gradient. The beam pass lenses of electromagnetic go to the specimen. The different types of bombardment with electrons emitted from specimen. This signal from effect of specimen are perform on the detector and amplifier. The most common signals used for imaging are secondary electrons, backscattered electrons, and characteristic X-rays. A detector catches the secondary electrons and an image of the sample surface is constructed by comparing the intensity of these secondary electrons to the scanning primary electron beam. In the study of supercapacitors, SEM have important information about the material surface morphologies for analysis of physical modifications or treatments effects on material phases and morphology (Frackowiak, 2007; Yu *et al.*, 2013). In this work, the morphologies were obtained using scanning electron microscope (SEM. JSM-7800F).
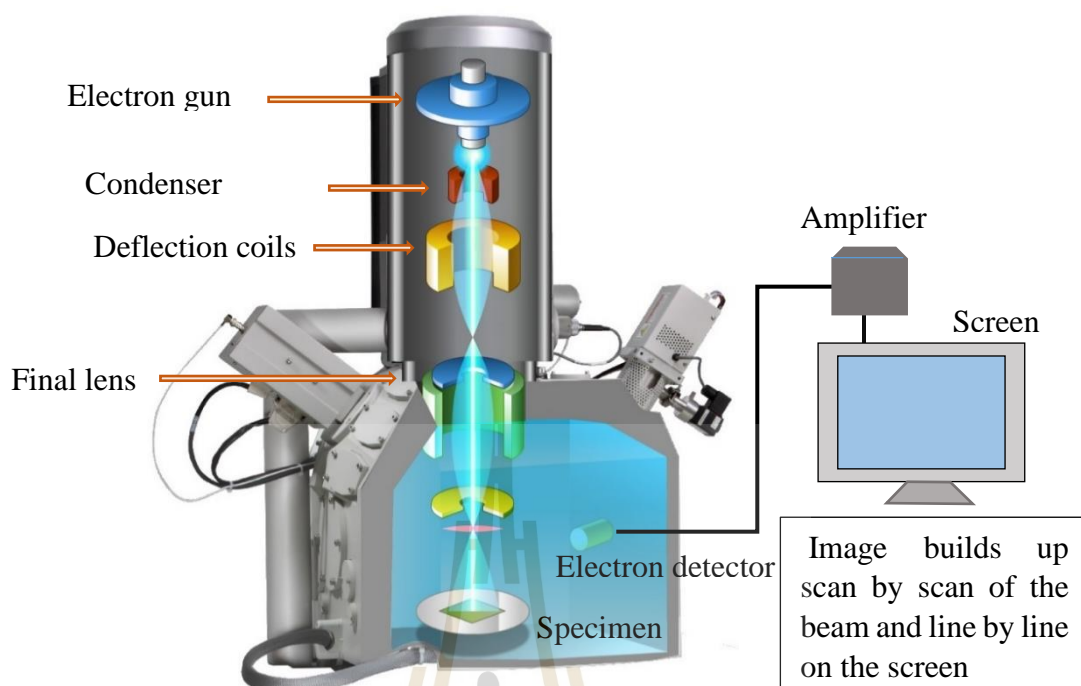
Figure 3.4 Diagram of Major component of SEM

(From https://myscope.training/#/SEMlevel_3_1).

3.9.3 Surface area and porosity

In surface area and porosity relate the BET theory technique. The determine of specific surface is based on the phenomenon physical adsorption of gas from surface of porous material. a sample is exposed to N_2 gas of different pressures at a given temperature (usually at -196 ^{o}C, the liquid-nitrogen temperature). Increments of pressure result in increased amounts of N_2 molecules being adsorbed on the surface of the sample. The pressure at which the adsorption equilibrium is established is measured and the universal gas law is applied to determine the quantity of N_2 gas adsorbed. Thus, an adsorption isotherm is obtained (Figure 3.5). If the pressure is systematically decreased to induce desorption of the adsorbed N_2 molecules, then a desorption isotherm is obtained.
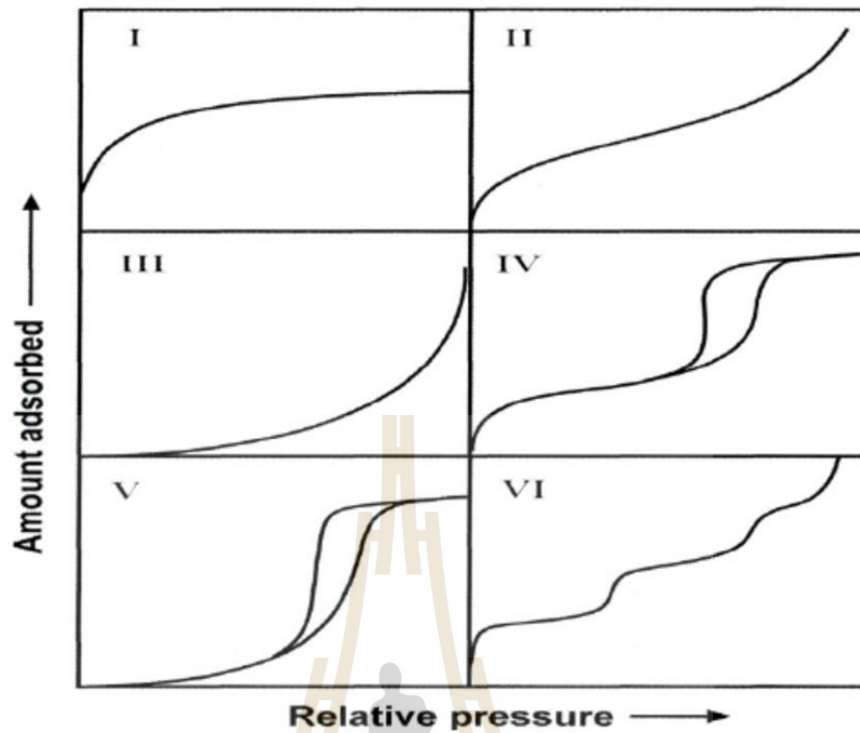
Figure 3.5 The IUPAC classification of adsorption isotherms (ALOthman, 2012).

Analysis of the adsorption and desorption isotherms in combination with some physical models yields information about the pore structure of the sample, such as surface area, pore volume, pore size and surface nature (Gubbins, 2009). In this study, the samples were degassed at 150 °C, for 6 h and then the N_2 adsorption/desorption isotherms were measured at 77 K using an automatic specific surface area/pore size distribution analyzer BELSORP-miniII. The Brunauer-Emmett-Teller (BET) method was used to describe the specific surface;

$$\frac{1}{W((P_0/P)-1)} = \frac{1}{W_mC} + \frac{C-1}{W_mC}\left(\frac{P}{P_0}\right) \qquad (3.5)$$

Where W is the weight of gas adsorbed, P/P_0 is the relative pressure, Wm is the weight of adsorbate as monolayer, and C is the BET constant. The total surface area (SB) can then be derived as follows:

$$S_B = \frac{W_m N A_{CS}}{M} \tag{3.6}$$

Where N is Avogadro's number (6.023×1023), M is the molecular weight of the adsorbate, and ACS is adsorbate cross section area (16.2 Å for nitrogen). The total pore volume (V_T) is derived from the amount of vapor adsorbed at a relative temperature close to unity by the following equation:

$$V_T = \frac{P_a V_{ads} V_m}{RT} \tag{3.7}$$

V_{ads} is the volume of gas adsorbed, V_T is the volume of liquid N_2 in total pore, V_m is molar volume of liquid adsorbate, Pa is ambient pressure, R is gas constant (8.314 J K^{-1} mol^{-1}), and T is ambient temperature. The average pore size is estimated from the pore volume assuming cylindrical pore geometry (type A hysteresis), the average pore radius (r_p) can be expressed as follows:

$$r_p = \frac{2V_T}{S_B} \tag{3.8}$$

The Barrett-Joyner-Halenda method (BJH) and Brunauer's MP (MP) methods were employed to determine the pore character of the samples. The pore size distribution was classified according to three regions: Micropore < 2 nm < Mesopore < 50nm < Macropore.

3.9.4 Fouries Transform Infrared Spectrometer (FTIR)

Furies transform infrared spectrometer is interaction of infrared radiation with a sample by measuring the frequencies at which the sample absorbs the radiation and the intensities of the absorptions. Chemical functional groups are known to absorb light at specific frequencies. Thus, the chemical structure can be determined from the frequencies recorded. In this thesis work, FTIR spectra were analyzed using Bruker Tensor 27 with a resolution of 4 c m^{-1} in the wavelength range of 400-4000 c m^{-1}. The samples were prepared without potassium bromide mixing (KB)

3.9.5 X-ray Photoelectron Spectroscopy (XPS)

X-ray photoelectron spectroscopy (XPS) is the electron spectroscopy for chemical analysis by used for investigation the chemical composition of surface and based on the photoelectric effect. The photoelectric process was ejected of electron from the shell. The ejected photoelectron has kinetic energy:

$$KE = h\nu - BE + \emptyset \tag{3.9}$$

Where KE is the hν is the energy of light, BE is the electron binding energy   and $\emptyset$ is the spectrometer work function. The process, the atom will be released energy by emission an electron.
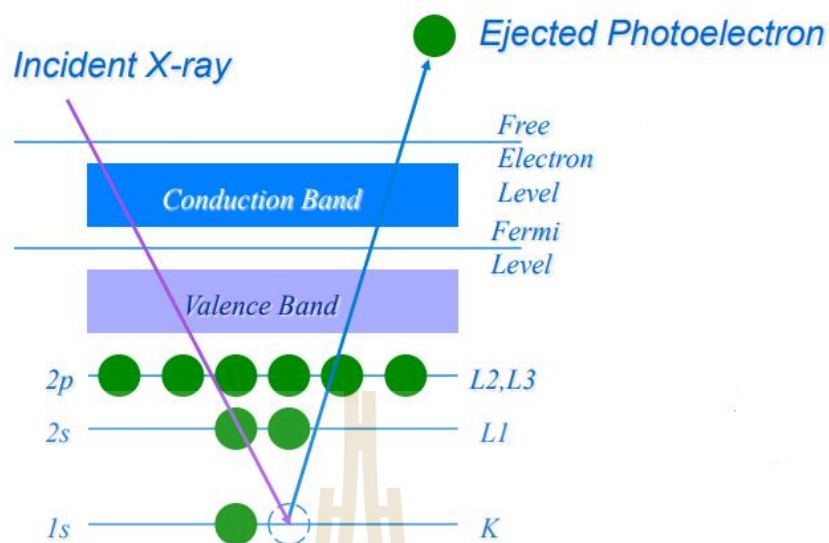
Figure 3.6 Photoelectron process.

3.9.6 Electrochemical measurements

The activated carbon was measured by autolab potentiostat galvanostat (PGSTAT 302N). The electrochemical properties were studied performance by cyclic voltammetry (CV), electrochemical impedance spectroscopy (EIS), and galvanostatic charge-discharge (GCD) techniques. In this work, we use the three electrodes system consists of a platinum wire (Pt) and silver/silver chloride (Ag/AgCl) electrodes used as working, counter, and reference electrodes, respectively. Basically, the current flows thought the CE and the WE, and the voltage is measured (or controlled) between RE and WE. Nova as the electrochemistry software from Metrohm Autolab were used to measure the electrochemical properties.

3.9.6.1 Cyclic voltammetry Cyclic Voltammetry (CV)

The principle techniques apply a voltage to electrode between two voltage limits. The current was recorded when the passed the working electrode and the counter electrode. The current passed the working electrode, the function of electrode potential to yield a CV with an example plot shown in Figure 3.7. This plot is known as voltammogram, which shows three different schematic voltammograms of ideal capacitor, resistive capacitor, and faradaic capacitor. An ideal capacitor displays a rectangular shape due to the capacitance (C) would keep constant at a scan rate. When the resistances present, the rounding of the voltammogram corners was observed. However, most EDLC devices suffer due to internal resistance; hence they display distorted voltammograms with irregular peaks. Prominent peaks that can occur within narrow voltage windows are usually evidence of pseudo-capacitive behavior (Conway *et al*., 1997).
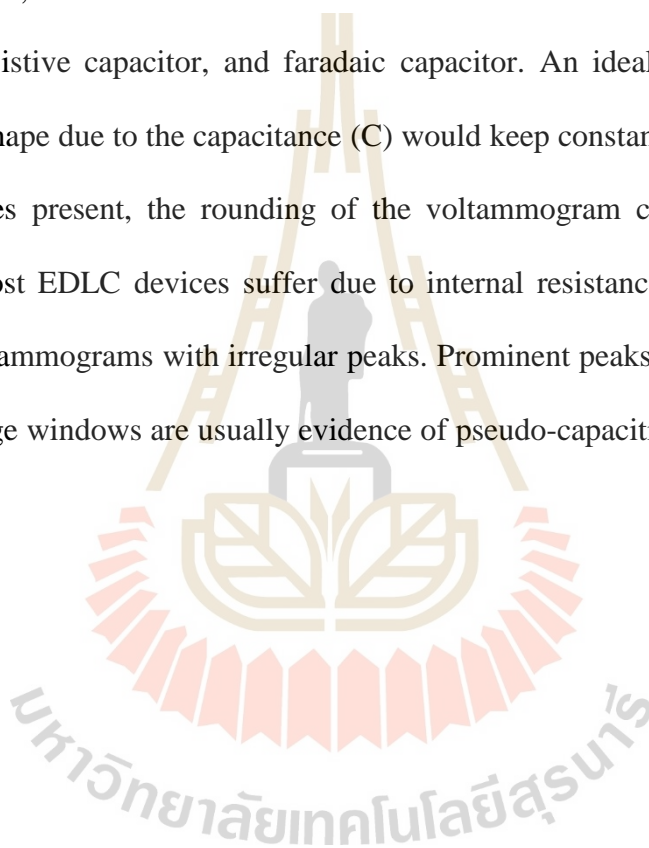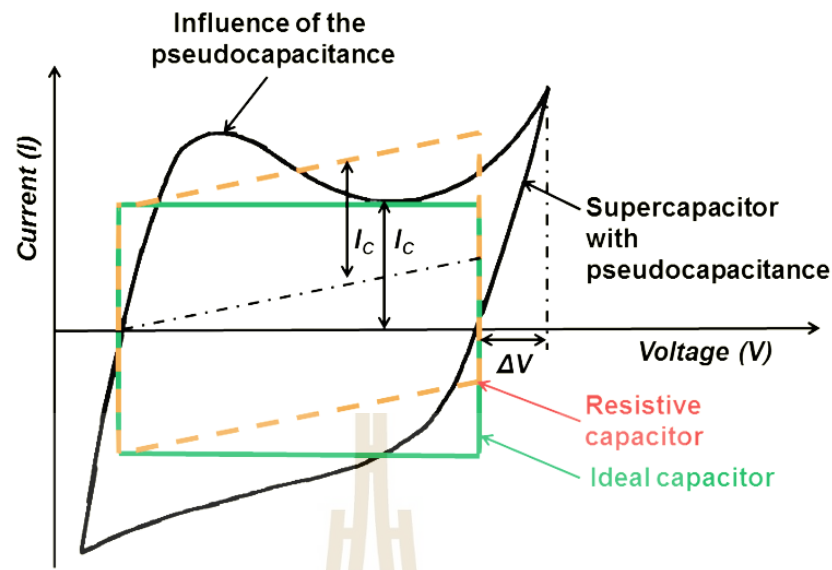
Figure 3.7 Cyclic voltammogram of three different electrochemical capacitors: ideal, resistive, faradaic capacitor.

(Adapted https://en.wikipedia.org/wiki/Pseudocapacitance).

In cyclic voltammetry, the enclosed area of the CV curve can be used to estimate the electrochemical specific capacitance (CCV) using the following equation (Yan *et al.*, 2012):

$$C_{CV} = \frac{1}{\upsilon m \Delta V} \int I dV \tag{3.10}$$

where I is the response current density discharge current (A cm^{-2}), $\int I dV$ is the area of the CV curve, υ is the potential scan rate (mV s^{-1}), m is the mass of the electroactive materials in the electrodes (g cm^{-2}), and ΔV is the potential window (V). According to this equation, the decreasing of scan rate effect to the decreasing of specific capacitance of material because of the short time at high scan rate caused large internal resistance and hardly penetrated of electrolyte ions into inner pores during charge

(Yuan *et al*., 2008). However, the specific capacitance depends on the active site number that mean redox reactions was active participated.

3.9.6.2 Galvanostatic charge-discharge

The charging-discharging (GCD) technique is analysis of electrochemical properties to concept of kinetics and mechanism of electrode reaction. In addition, the determine specific capacitance, energy density, power density and supercapacitor are approach in this GCD technique (Yu *et al*., 2013). In the measurement. We apply a constant cell current for the performed measurement. The charging and discharging time were recorded by cell voltage. In this work, the GCD curves at different current densities of 0.5, 1, 2, 5, 10, 15, 20 and 30 A g^{-1} were investigated for performance electrode of specific capacitance. The discharge exhibits a nonlinear when electrode was founded, this can (Nithya *et al*., 2013):

$$C_{GCD} = \frac{2E}{m(\Delta V)^2} \tag{3.11}$$

where C $_{GCD}$ is the specific capacitance (F g^{-1}), E is the energy density, m is the total mass of the active material, ΔV is the discharge potential window. The important performance indicators for evaluating an electrochemical supercapacitor such as specific energy density (W kg^{-1}), specific power density (W kg^{-1}) were calculated using following equations (Nithya *et al*., 2013):

$$E = \frac{\int V(t)dt}{m} \tag{3.12}$$

$$P = \frac{E}{t} \tag{3.13}$$

Where $\int V(t)dt$ is the integral area of the discharge curve and t is the discharge time.
Moreover, because of long term cycling stability is important for practical applications
for supercapacitors. Therefore, endurance of the electrodes was tested up to 500 charge-
discharge cycles at a current density of 10 A g^{-1}.

3.9.6.3 Electrochemical impedance spectroscopy (EIS).

Electrochemical impedance spectroscopy (EIS) is tool of experiment for the
measurement frequency response of electrode. For investigated reaction in the electrode
and electrolyte interface. (Bard *et al*., 1980). This process. The sinusoidal potential of
small amplitude to the cell electrodes were applied for observed response of result
current to obtain the impedance of the system (Taberna *et al.*, 2006). The apply
sinusoidal potential and the responding current ($\Delta I(\omega)$) are given as:

$$\Delta I(\omega) = \Delta I e^{j(\omega t + \emptyset)} \tag{3.14}$$

Where I is the current amplitude. $\omega = 2\pi f$ is the angular frequency, and $\emptyset$ is phase shift
between current response and the potential. The electrochemical impedance Z (ω) is
defined as:

$$Z(\omega) = \frac{\Delta V}{\Delta I} = |Z(\omega)| e^{-j\emptyset} = Z' + jZ'' \tag{3.15}$$

where Z′ and Z″ are the real part and the imaginary part of the impedance, respectively
defined as:

$$Z'^2 + Z''^2 = |Z(\omega)|^2 \tag{3.16}$$

The impedance responses recorded by the EIS instrument are normally shown as
Nyquist plots that illustrate the relationship between imaginary part impedance (-Z″)

and real part impedance (Z') based on the equivalent circuit having the components of solution resistance (R_s), charge-transfer resistance (R_{ct}), constant phase element (CPE) and Warburg impedance (W). The intercept in the Z' axis at a high frequency refers to Rs which stands for ohmic resistance of the electrolyte, internal resistance of the electrode material and contact resistance at the electrode/current collector interface (Nithya *et al*., 2013).
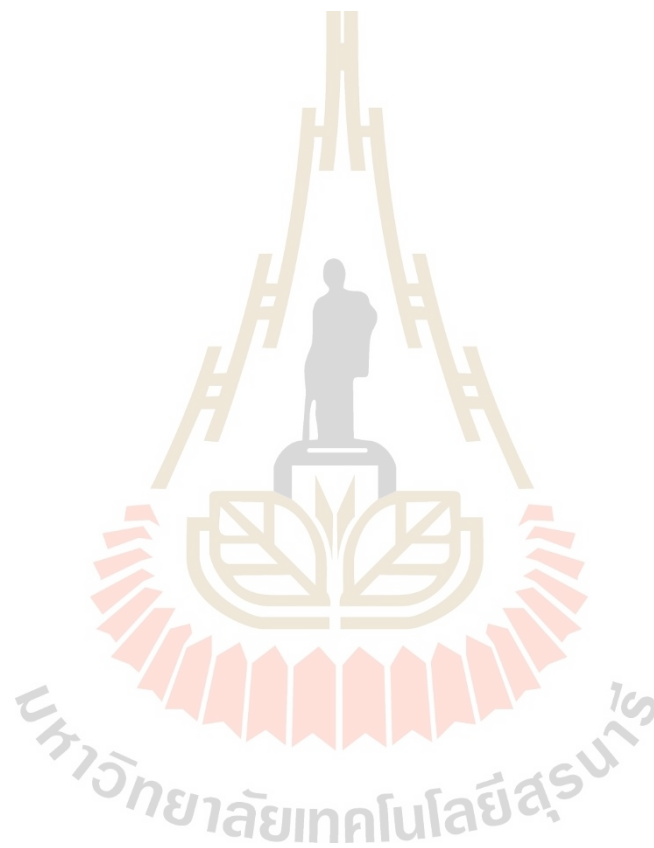
CHAPTER IV

RESULTS AND DISCUSSION

This chapter presents the results and discussion of prepared activated carbon by potassium hydroxide (KOH) derived from cassava starch. Each section consists of fabrication, characterization, and electrochemical studies. The effect of activated carbon derive from cassava starch were studies effect of temperature on the pore structure and effect of chemical ratio with KOH activation. The characterization of the sample was done by various techniques to understand thermal stability, morphology, microstructure, and porosity using the Scanning electron microscope (SEM), X-ray photoemission spectroscopy (XPS), Fourier transform infrared spectroscopy (FTIR), X-ray diffraction (XRD) and Brunauer-emmett-teller (BET) method. Finally, in part of understanding the electrochemical properties as sample, three electrochemical method including to cyclic voltammetry (CV) galvanostatic charge/discharge (GCD) and electrochemical impedance spectroscopy (EIS) were evaluated to explain the capacitive behavior, equivalent circuit of sample and cycling stability.

4.1 Carbonization at temperature of 600 ºC

4.1.1 Structural and morphology characterization.

4.1.1.1 X-ray diffraction (XRD) analysis of the prepared samples at carbonization temperature of 600 ºC

The XRD spectra of the prepared samples were measured with Cu Kα wavelength of 1.54 Å. The diffraction angles were taken from 2 theta of 10 - 80 º with step time and size of 0.2 and 0.02, respectively. The samples were calcined at temperature of 600 ºC with different KOH concentrations in an argon atmosphere which are denoted as carbon: KOH ratio of 1:1, 1:3, and 1:5. As shown in Figure 4.1, two broad peaks at $2\Theta = 23$ º and 43 º were observed which correspond to the (002) and (100) plan, respectively (Peng *et al.*, 2014). Both of them are characteristic of carbon structure. However, the broad peaks at $2\Theta = 43$ º disappeared in the sample of ACCS 600 (1:5) with higher KOH concentration.
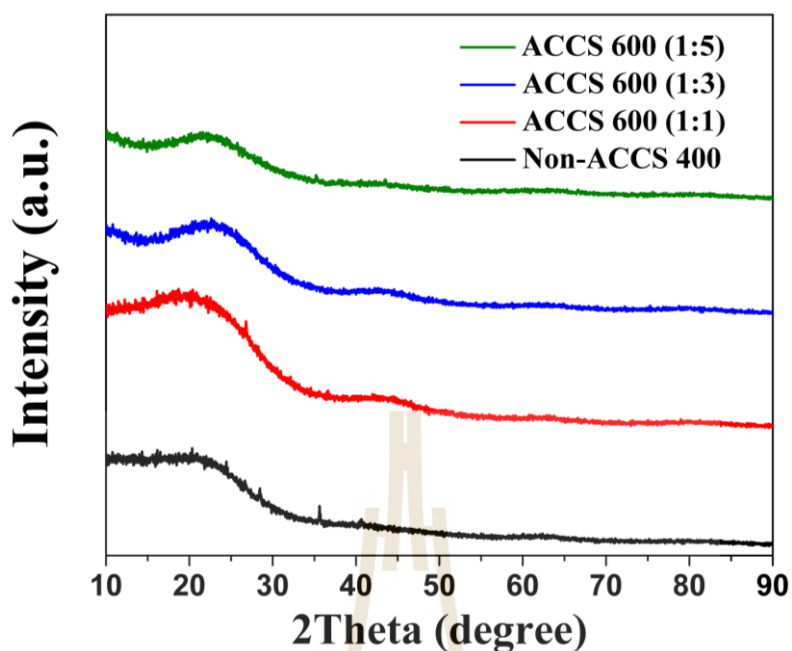
Figure 4.1 XRD patterns of non-activated carbon and activated carbon with differential concentration of activated carbon derive from cassava starch.

4.1.1.2 Morphology of the carbonization at 600 ºC temperature by SEM.

The morphology of activated carbon under the different carbon: KOH ratio was studied by SEM. As shown in Figure 4.2(a), the non-activated carbon (Non-ACCS 400) reveals the smooth surface of non-porous carbon. The rough surface with the presence of pores found in the samples after KOH activation which resulted from the evaporation of the activated agent (Yakout and El-Deen, 2016) as seen in Figure 4.2(b - d). This implies that the microstructure of carbon material was modified after KOH activation. The pore structure of the carbon material after the activation also depends on the KOH concentration (Jiang *et al.*, 2014) which plays an important role in electrochemical performance. As seen in Figure 4.2(b – d), the estimated pore size

of sample ACCS 600 (1:3) is larger than ACCS 600 (1:1) and ACCS 600 (1:5). The pore is formed in the structure due to the chemical reaction during the KOH activation using the following equation:

$$6KOH + 2C \rightarrow 2K + 3H_2 + 2K_2CO_3 \qquad (4.1)$$
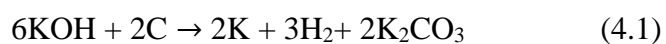
After the KOH activation, the K_2CO_3 decomposed into CO_2 and K_2O and pore are formed and developed in the structure (Cao *et al.*, 2016).
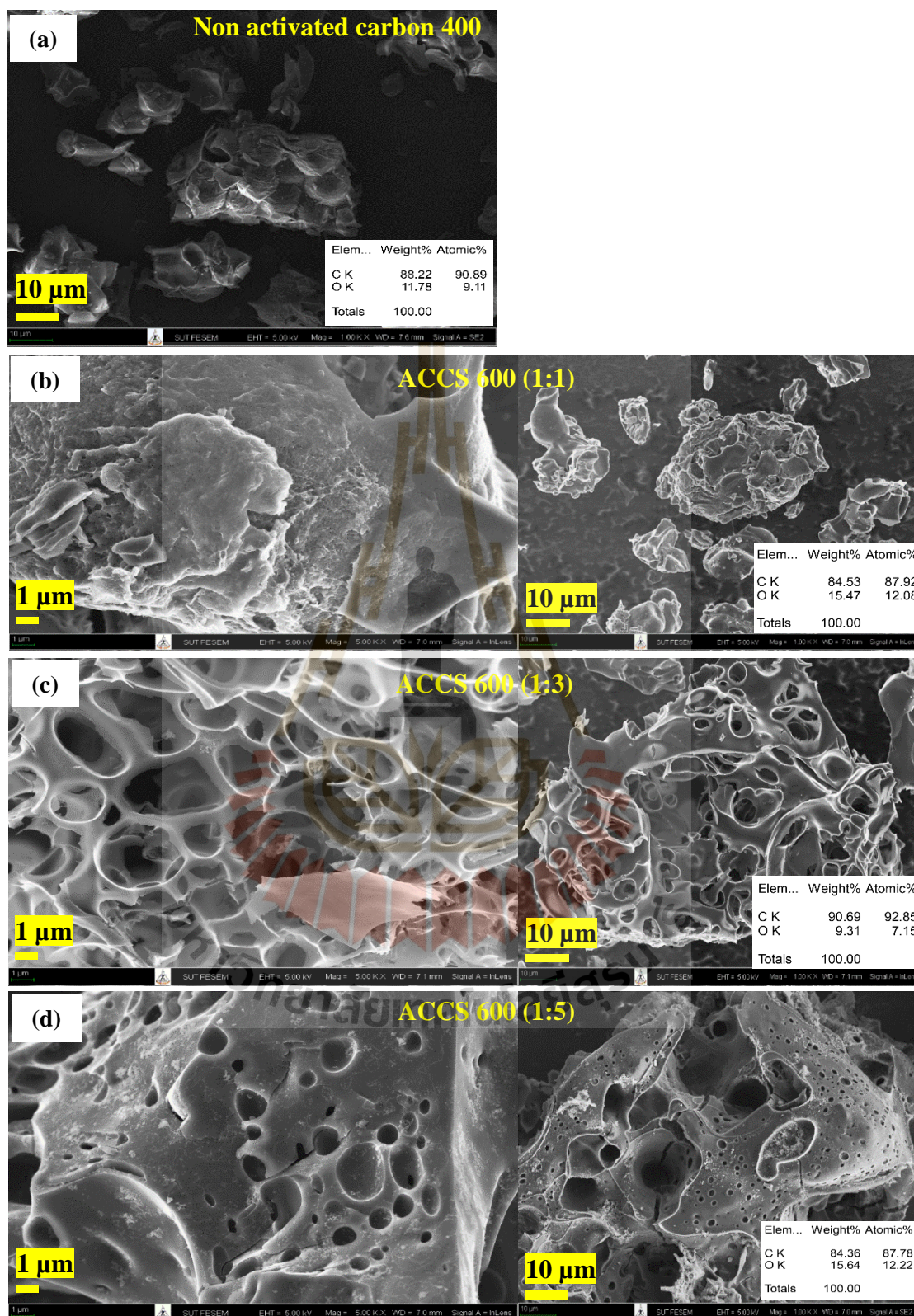
Figure 4.2 SEM images of non-activated carbon (a) Non ACCCS 400 and activated carbon (b) ACCS 600 (1:1), (c) ACCS 600 (1:3) and (d) ACCS 600 (1:5).

4.1.1.3   Characterization of surface area and pore size distribution of the carbonization at temperature of 600 ºC by BET method and BJH method

Figure 4.3 shows the nitrogen adsorption-desorption isotherms of porous activated carbon prepared at different impregnation ratio of KOH. According to the IUPAC classification, all samples exhibit a typical type-I curve with unapparent hysteresis loop which indicated that all samples have a microporous structure (Sing, 1985). The activated carbon with different KOH concentration has an remarkable effect on the pore structure, resulting in higher surface area when compared with non-activated carbon (Wang *et al*., 2015). The calculated pore size from BJH method of non-ACCS 400, ACCS 600 (1:1), ACCS 600 (1:3) and ACCS 600 (1:5) is about 6.52 nm, 1.90 nm, 1.79 nm, and 2.21 nm, respectively (see Table 4.4). The specific surface area of all samples increased after KOH activation, resulting in an increasing of specific capacitance. The sample of ACCS 600 (1:3) shows the highest specific surface area of 1175 m^2 g^{-1} with the lowest specific surface area found in sample of non-activated carbon (Non-ACCS 400). Therefore, these results indicate that the surface area is enlarged by KOH activation under different activation condition. It is the effectively way to generate nanoscale pore in the carbon material.

Figure 4.3 BET measurements of non-activated and activated carbon of ACCS 600 (1:1), (ACCS 600 (1:3) and ACCS 600 (1:5) derived from cassava starch.
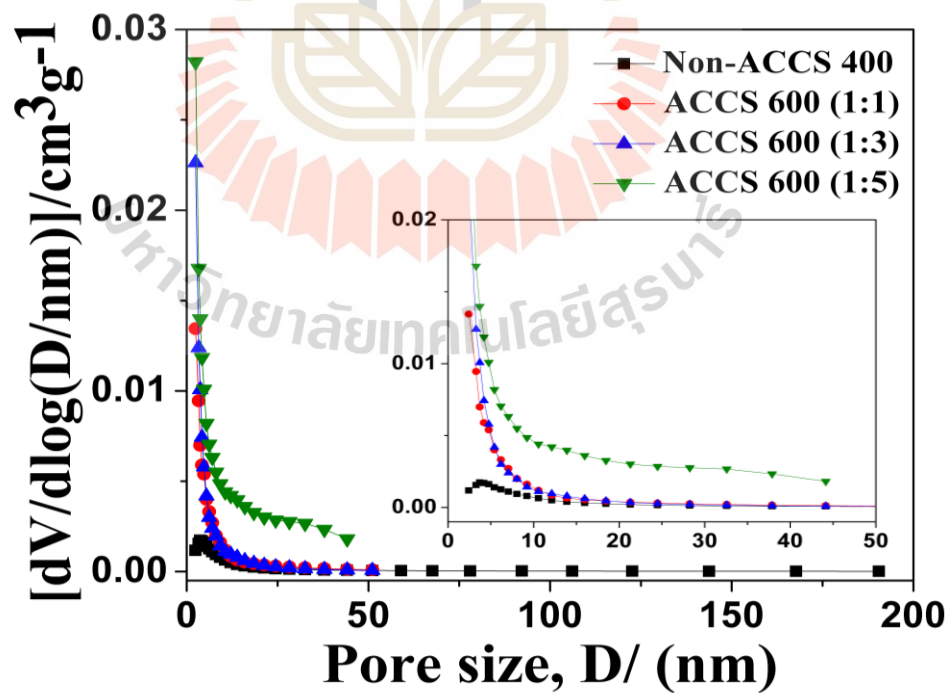
Figure 4.4 (a) BJH pore distribution plots of non-activated and activated carbon of ACCS 600 (1:1), (ACCS 600 (1:3) and ACCS 600 (1:5) derived from cassava starch.

Table 4.1 BET results of non-activated   and activated carbon of ACCS 600 (1:1), ACCS 600 (1:3) and ACCS 600 (1:5) derived from cassava starch.

Sample	BET			Micropore	Mesopore
	S_{BET}	D_P	V_T	V_{mi}	V_{me}
	$(m^2\,g^{-1})$	(nm)	$(cm^3\,g^{-1})$	$(cm^3\,g^{-1})$	$(cm^3\,g^{-1})$
Non-ACCS 400	14.80	6.52	0.02	4.55	0.02
ACCS 600 (1:1)	611	1.90	0.29	0.28	0.06
ACCS 600 (1:3)	1175	1.79	0.53	0.53	0.07
ACCS 600 (1:5)	1087	2.21	0.60	0.45	0.20

* S_{BET} = Surface area, D_P = Mean pore diameter, V_T = Total pore volume, V_{mi} = Micro pore volume and V_{me} = Mesopore volume

4.1.1.4 Fourier transform infrared (FTIR) analysis of the carbonization at 600 ºC temperature

The surface function groups of the non-activated carbon (Non-ACCA 400) and all the activated carbon of ACCS 600 (1:1), ACCS 600 (1:3) and ACCS 600 (1:5) were determined using FTIR analysis. The FTIR spectra of all samples are shown in Figure 4.5. The transmittance broad peak at 2923 c m^{-1} indicates the presence of C-H bond in all samples. The adsorption peak at 1738 c m^{-1} shows the apparent C=O bond in all samples. The strong bond is seen at about 1638 c m^{-1} that may be described to olefin C=C vibration in aromatic region for the material (Yagmur *et al.*, 2008). The absorption peak around 1246-1385 c m^{-1} indicates the existence of C-O single bond in carboxylic acid, alcohol phenol in phosphate ester (Puziy *et al.*, 2005). The peaks in the range of 500-700 c m^{-1} can be attributed to the C-H bending vibration stretching which are showed in all samples. The treatment of the carbon with KOH caused a decrease of helium density, resulting from some mineral impurities removal (Lee *et al.*, 1999).
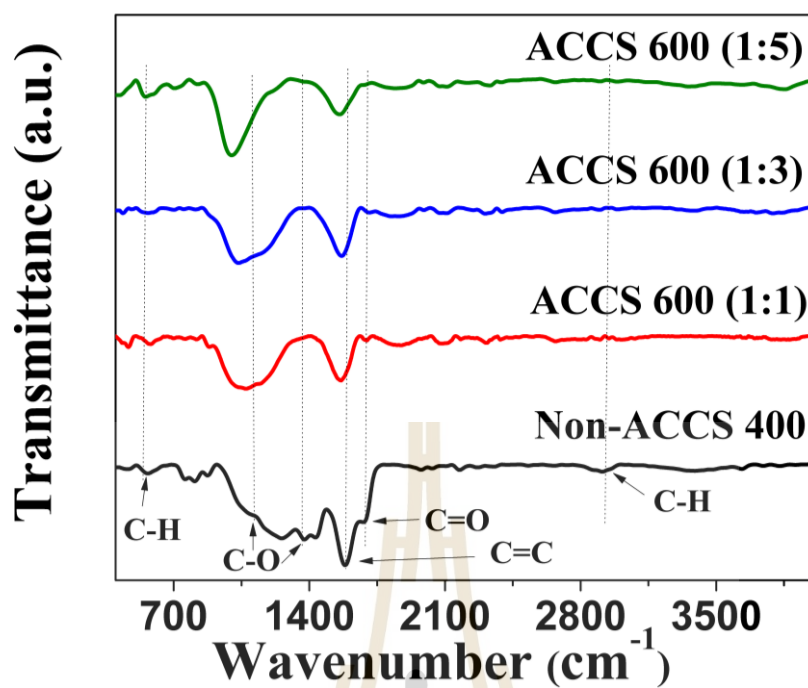
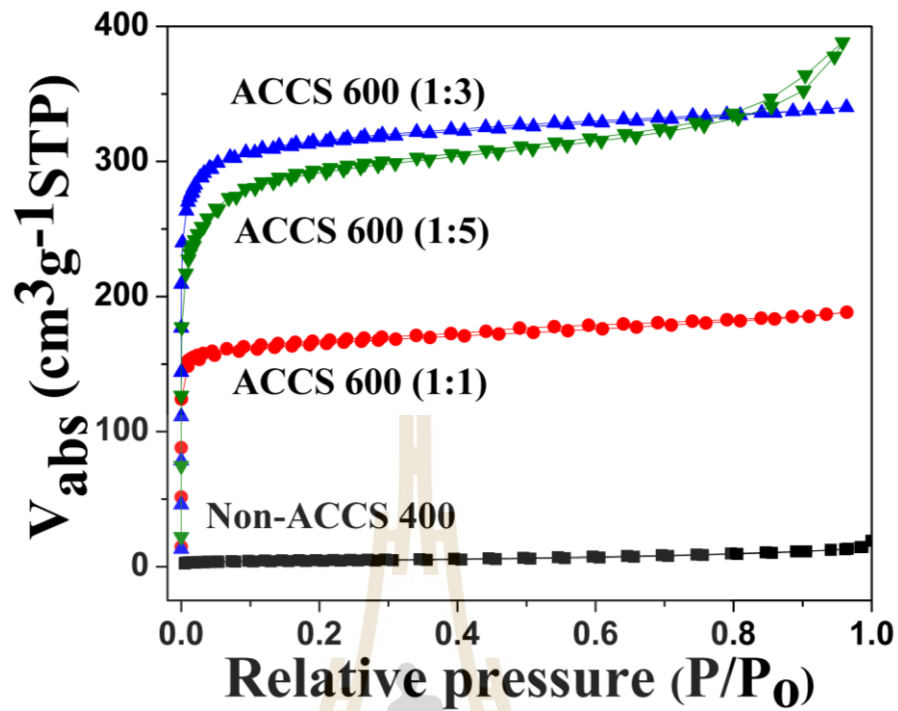**Figure 4.5** FTIR pattern of non-activated and activated carbon of (ACCS 600 (1:1)

(ACCS 600 (1:3) and ACCS 600 (1:5)) derived from cassava starch.

4.1.1.5 X-ray photoemission spectroscopy (XPS) analysis of the carbonization at 600 ⁰C temperature

The chemical compositions of the activated carbons were studied by XPS. The high resolution XPS spectra of C1s peaks of the activated carbon (ACCS 600 (1:1), ACCS 600 (1:3), and ACCS 600 (1:5)) are shown in Figure 4.6. The C1s spectra can be deconvoluted into three sub-peaks at approximately 284.8 eV, 286.2 eV and 288.3 eV which are attributed to C-C/C=C bond, C-O bond and O-C=O bond, respectively (Shulga *et al.*, 2015). The C/O and carbon functional groups concentration of all samples are slightly different. This result shows that the KOH activation has significant effect on the chemical composition of the samples.
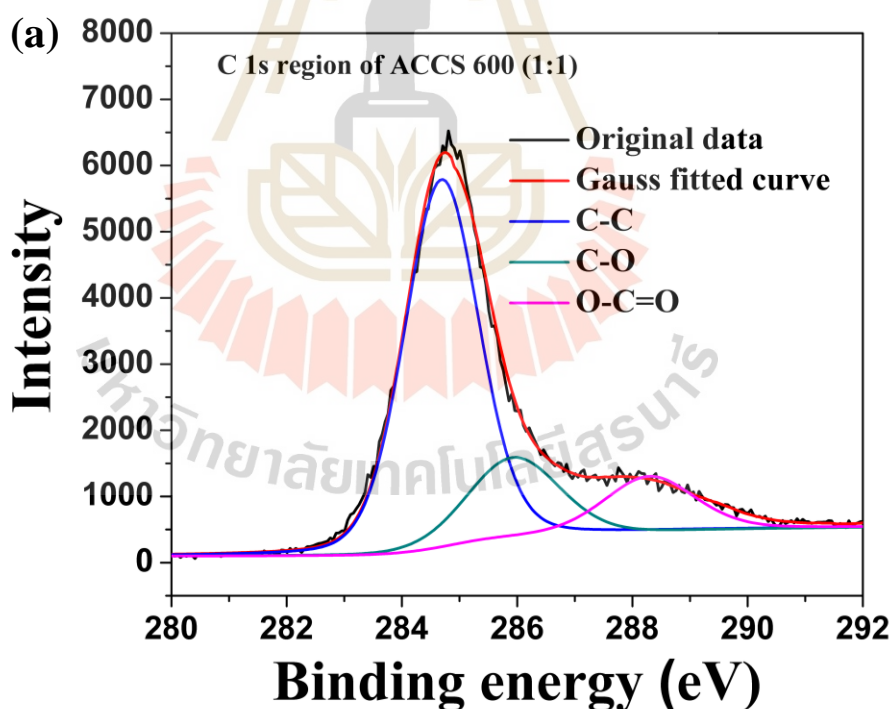
Figure 4.6 High resolution XPS spectra of C1s peak of non-activated and activated carbon of (a) ACCS 600 (1:1), (b) ACCS 600 (1:3) and (c) ACCS 600 (1:5) derived from cassava starch.
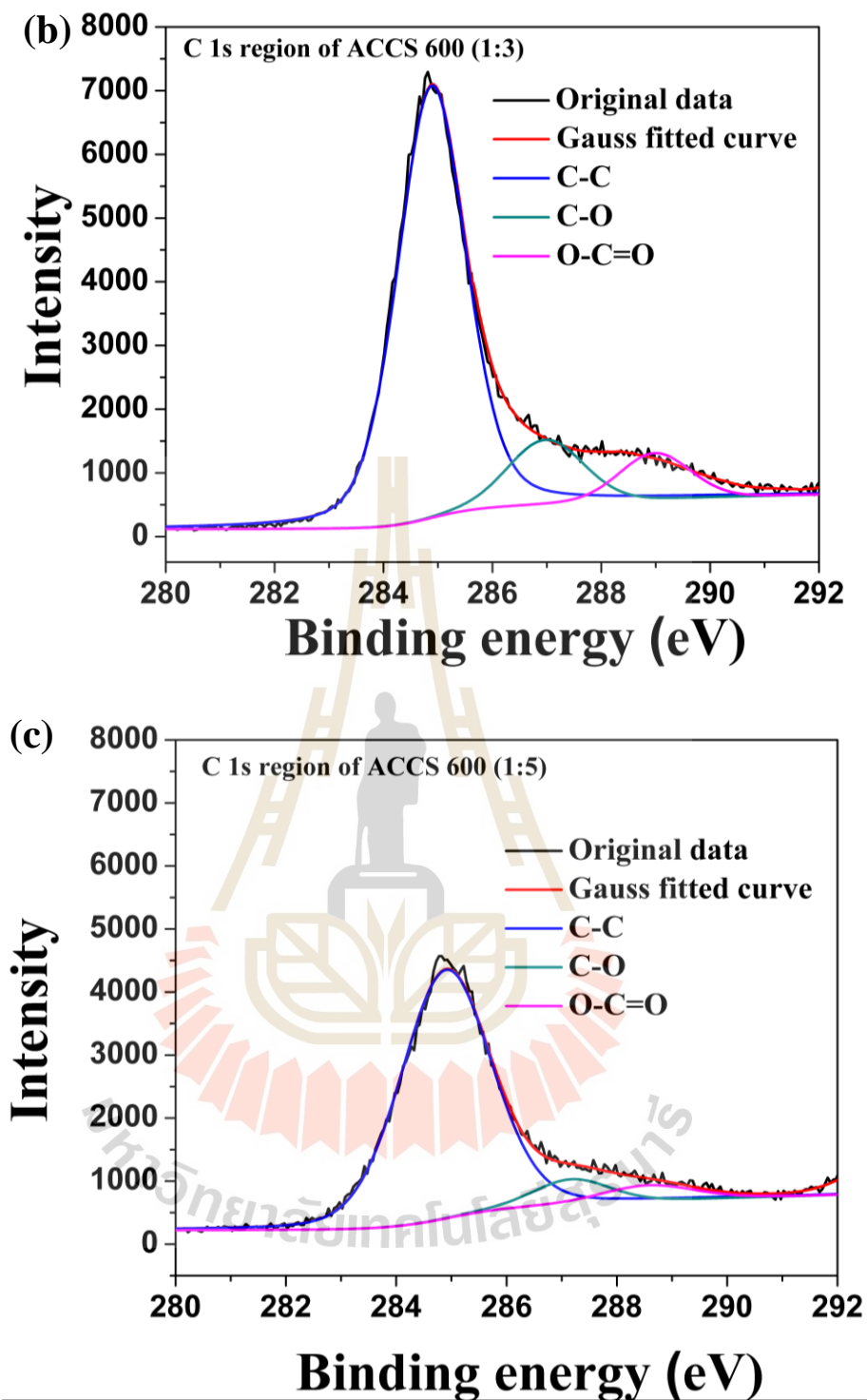
Figure 4.6 (Continued) High resolution XPS spectra of C1s peak of non-activated and activated carbon of (a) ACCS 600 (1:1), (b) ACCS 600 (1:3) and (c) ACCS 600 (1:5) derived from cassava starch.

4.1.2 Electrochemical properties

4.1.2.1 Cyclic voltammetry measurement

The cyclic voltammetry (CV) curves of activated carbon derived from cassava starch at carbonization temperature of 600 ^{o}C with potential windows between -1 to 0 V and different scan rate of 2 to 200 mV s^{-1} are present in the Figure 7. All samples were measured in 6M NaOH solution using three electrodes system. The CV curves of all samples reveal a quasi-rectangular shape, indicating an ideal double layer capacitor. The area of rectangular shape increases with increasing scan rate from 2 – 200 mV s^{-1} due to a fast charge-discharge rate and low equivalent series resistance (Peng *et al.*, 2016). In addition, the non - activated carbon (Non-activated carbon 400) has a smaller area comparing with the activated carbon of all samples. This result indicated that the activated carbon possesses a higher specific capacitance value than the non-activated carbon, resulting from the creation of pores after the KOH activation.
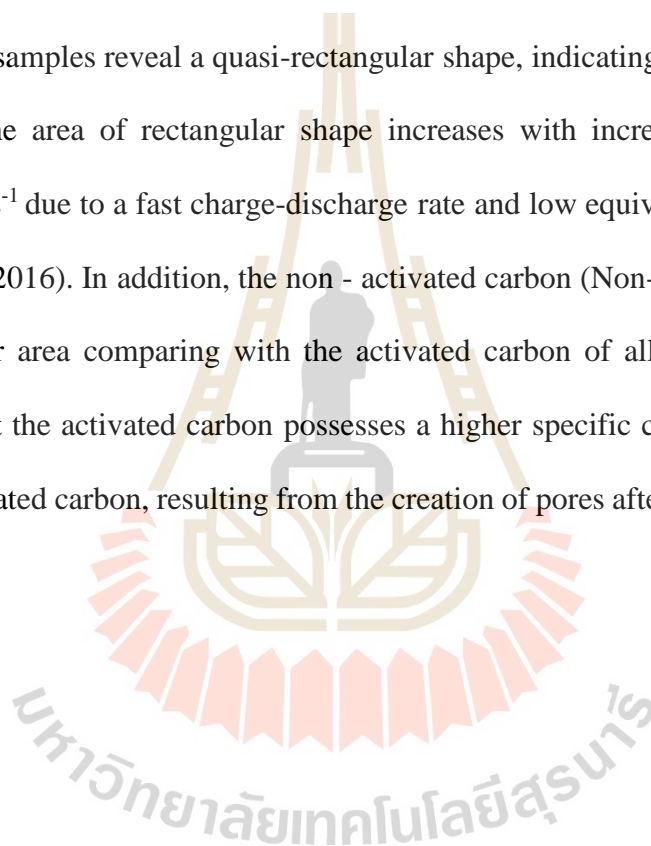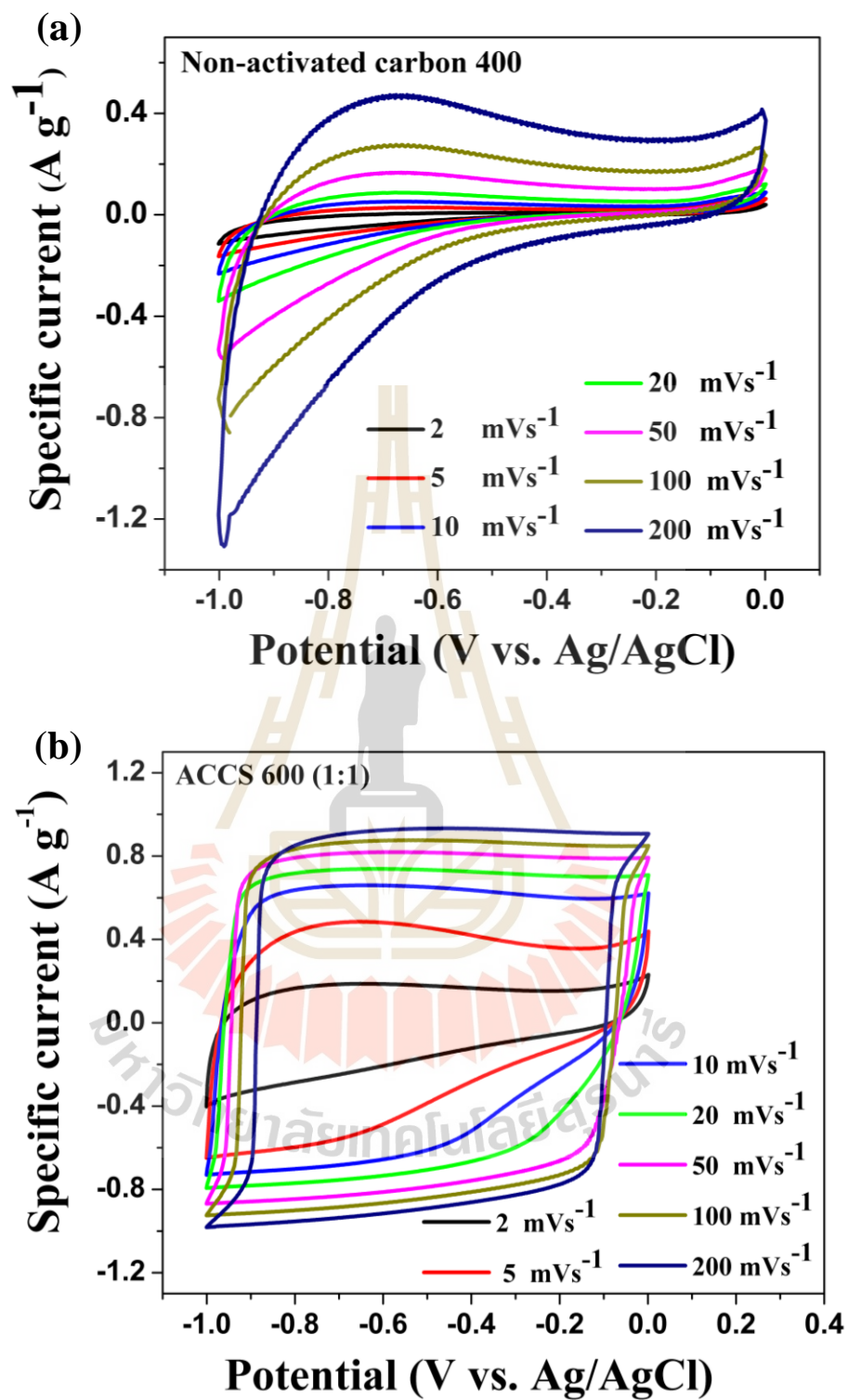
Figure 4.7 CV curves of the activated carbon derived from cassava starch: (a) Non-ACCS 400, (b) ACCS 600 (1:1), (c) ACCS 600 (1:3) and (d) ACCS 600 (1:5).
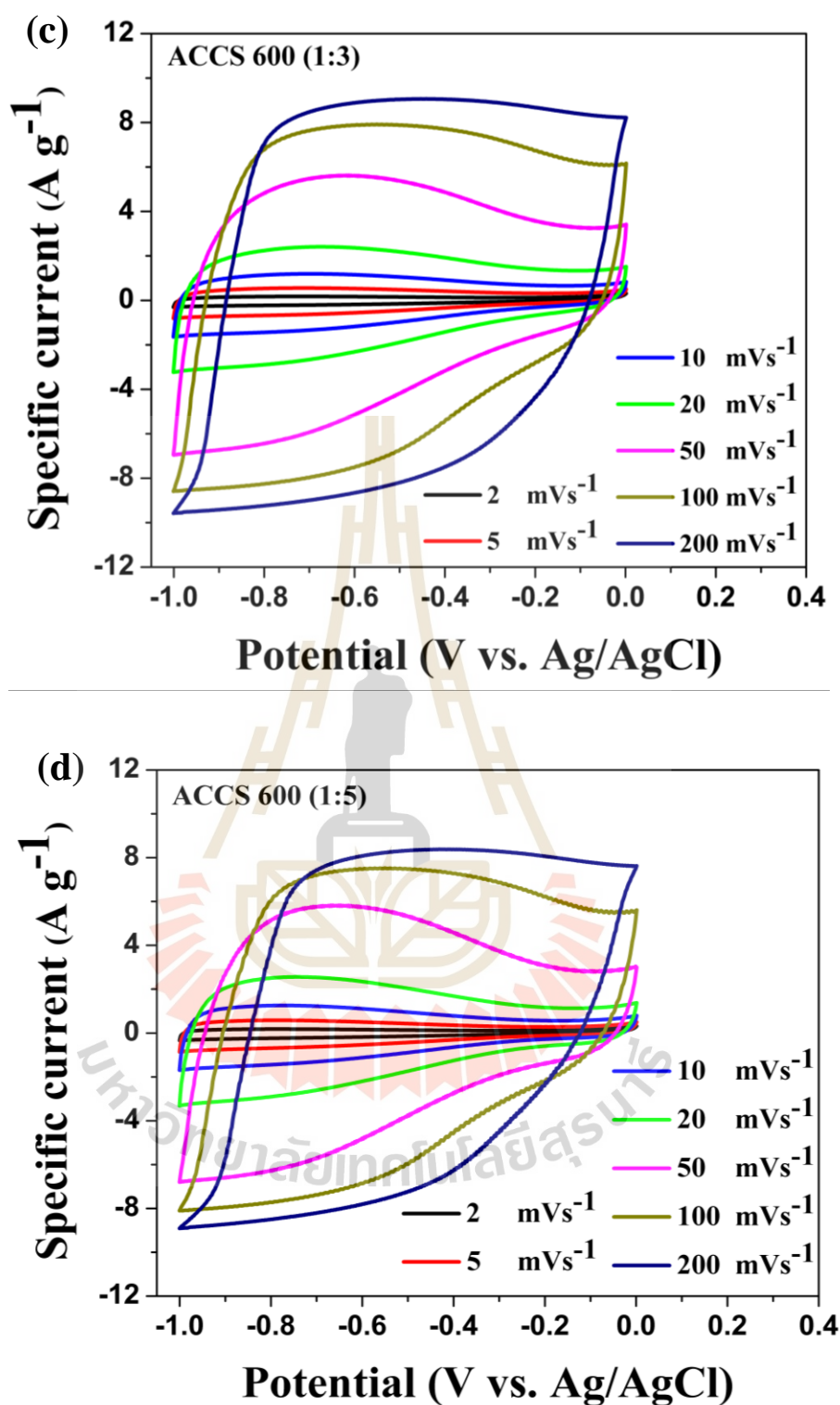
Figure 4.7 (Continued) CV curves of the activated carbon derived from cassava starch:

(a) Non-ACCS 400, (b) ACCS 600 (1:1), (c) ACCS 600 (1:3) and (d) ACCS 600 (1:5).

4.1.2.2 Galvanostatic charge-discharge measurement.

The galvanostatic charge-discharge curves of all samples with different current densities from 0.5 to 30 A g^{-1} are shown in Figure 4.8. As the current density increases, the discharging time decreases. The shape of the charge - discharge curves exhibits a closely linear, indicating a good capacitance of these material (Zheng *et al.*, 2014). The calculated specific capacitance of non-ACCS 400, ACCS 600 (1:1), ACCS 600 (1:3) and ACCS 600 (1:5) is 14, 108, 114 and 107 F g^{-1}, respectively. The maximum specific capacitance value of 114 F g^{-1} at current density of 0.5 A g^{-1} was obtained from the sample of ACCS 600 (1:3) as shown in Table 4.3. Because of their high surface area (> 600 m^2 g^{-1}) and larger pore volume of the activated carbon samples, the specific capacitance value is higher when compared with non-activated carbon.
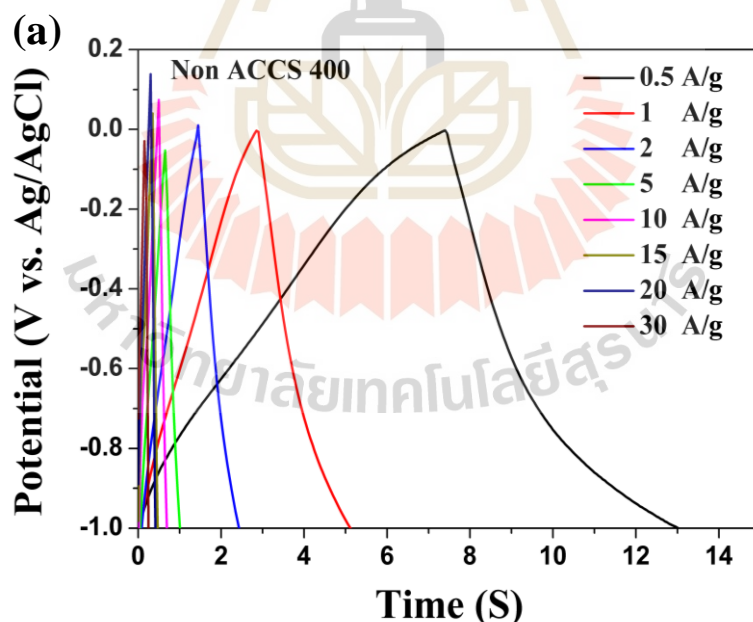
Figure 4.8 Galvanostatic charge-discharge curves of the activated carbon derived from cassava starch: (a) Non-ACCS 400, (b) ACCS 600 (1:1), (c) ACCS 600 (1:3), (d) ACCS 600 (1:5) and (e) GCD curve comparison capacitance value of all sample.

Figure 4.8 (Continued) Galvanostatic charge-discharge curves of the activated carbon derived from cassava starch: (a) Non-ACCS 400, (b) ACCS 600 (1:1), (c) ACCS 600 (1:3), (d) ACCS 600 (1:5) and (e) GCD curve comparison capacitance value of all sample.

Figure 4.8 (Continued) Galvanostatic charge-discharge curves of the activated carbon derived from cassava starch: (a) Non-ACCS 400, (b) ACCS 600 (1:1), (c) ACCS 600 (1:3), (d) ACCS 600 (1:5) and (e) GCD curve comparison capacitance value of all sample.

Table 4.2 Specific capacitance from GCD curve of non-activated and activated carbon of ACCS 600 (1:1), (ACCS 600 (1:3) and ACCS 600 (1:5) derived from cassava starch.

| Sample	Current density (A/g)							
	0.5	1	2	5	10	15	20	30
ACCS 600 (1:1)	108	93	78	61	49	44	41	36
ACCS 600 (1:3)	114	108	101	92	83	78	74	69
ACCS 600 (1:5)	107	104	101	99	96	94	93	90

4.1.2.3 The Nyquist plot of non-activated and activated carbon.

The behavior of the activated carbon electrodes was further investigated by the electrochemical impedance spectroscopy (EIS). Figure 4.9 shows the Nyquist plot of the non-activated and activated carbon electrodes. The obtained solution resistance (Rs) from the intercept of Z′ axis (inset in Figure 4.9) indicates that the non-activated carbon electrode has the higher Rs value than the activated carbon electrode. The Rs does tends to increase with increasing KOH ratio. The better electrochemical performance of ACCS 600 (1:1), ACCS 600 (1:3) and ACCS 600 (1:5) can be attribution to the better electrochemical conductivity compared with non-activated carbon (Peng *et al.*, 2014).
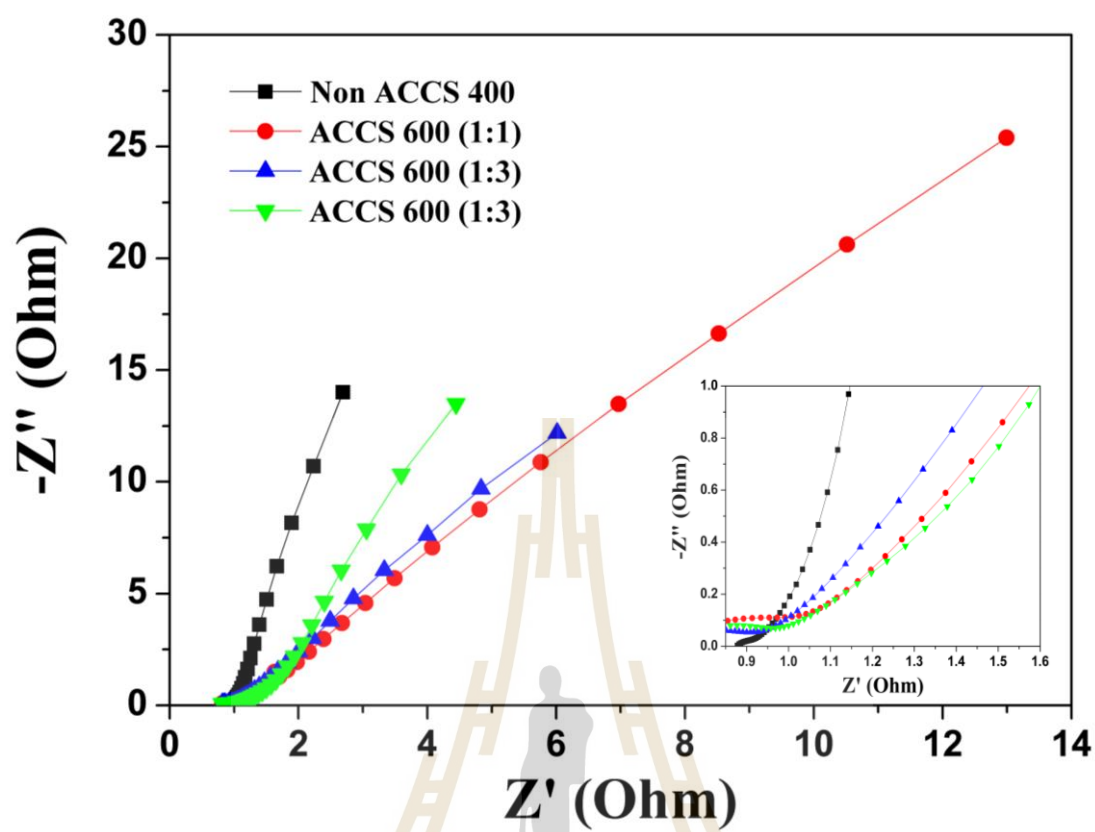
Figure 4.9 The Nyquist plot of non-activated carbon and activated carbon drive from
cassava starch.

4.1.2.4 The cycle life of non-activated carbon and activated carbon derived from cassava starch

As shown in Figure 4.10, the cyclic lifetime for the sample ACCS 600 (1:1) possess the highest capacitance retention. The slightly increase of the specific capacitance after 1000 cycles may be due to the high surface to volume ratio of ACCS 600 (1:1) when compared with ACCCS 600 (1:3) and ACCCS 600 (1:5), allowing more active surfaces for ion adsorption. Moreover, the Coulomb efficiency of electrode as function of cycle number can be calculated from the following equation (Peng *et al.*, 2013):

$$\eta\ (\%) = \frac{T_d}{T_c} \times 100 \qquad (4.1)$$

Where T_d is discharge time and T_c is charge. The Coulomb efficiency of Non ACCS 400, ACCS 600 (1:1), ACCS 600 (1:3) and ACCS 600 (1:5) samples remains the value of 53 %, 121 %, 93 % and 94 %, respectively after 1000 cycles. This result indicate that the activated carbon electrode has long life cycle stability and good electrochemical conductivity (Huang *et al.*, 2014; Li *et al.*, 2008).
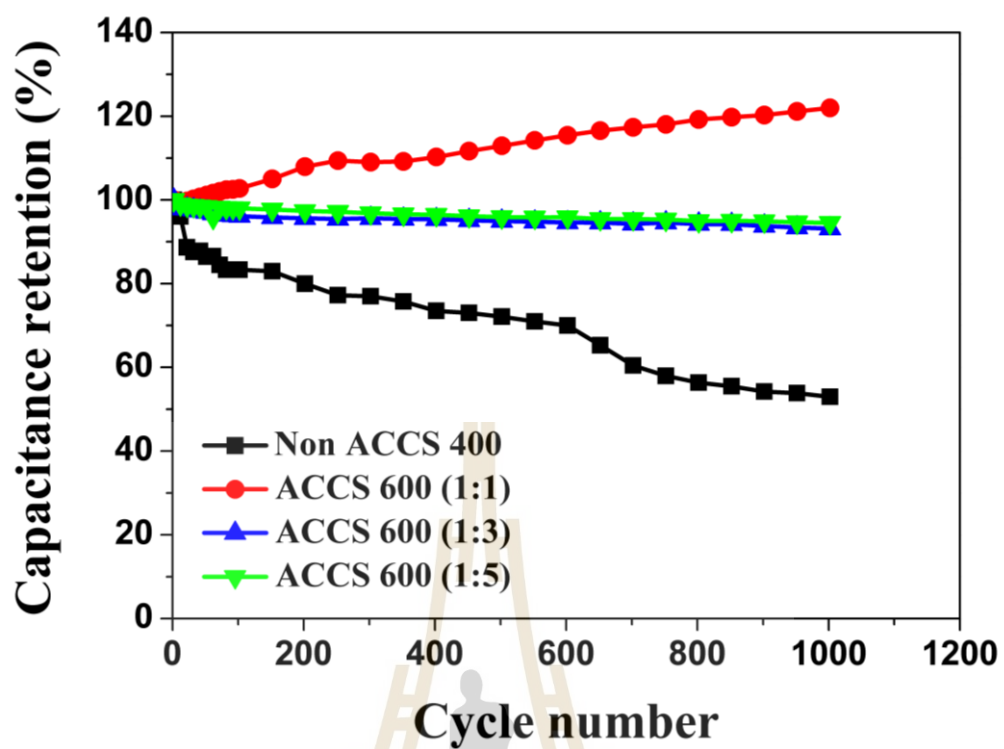
Figure 4.10 the cycle life of non-activated carbon and activated carbon drive from cassava starch.

4.2 Carbonization at 700 ºC Temperature

4.2.1 Structural and morphology characterization.

4.2.1.1 X-ray diffraction (XRD) analysis carbonization at 700 ºC temperature

The XRD spectra of prepared samples in Figure 4.7 were measured with Cu, Kα wavelength of 1.54 Å between 2Θ from 10 to 80 º, step time 0.2 and step size 0.02. The samples were calcined with the differential concentration of KOH at the 700 ºC in argon atmosphere. The XRD pattern of all samples show the broad peak of amorphous carbon about 2Θ = 23 º corresponding to plane 002 crystal plane diffraction peak that indicated the amorphous carbon structures mainly formed during carbonization. However, the broad peak of 2Θ = 43 º for Non ACCS 400 is disappearance. But this peak was presented in the ACCS 700 (1:1), ACCS 700 (1:3) and ACCS 700 (1:1). Indicating that intensity in the angle scatter are increasing which activated carbon at l:1 KOH activation (ACCCS 700 (1:1)) and decreasing of intensity which high activated carbon ratio at ACCS 700 (1:5) (Peng *et al.*, 2014).
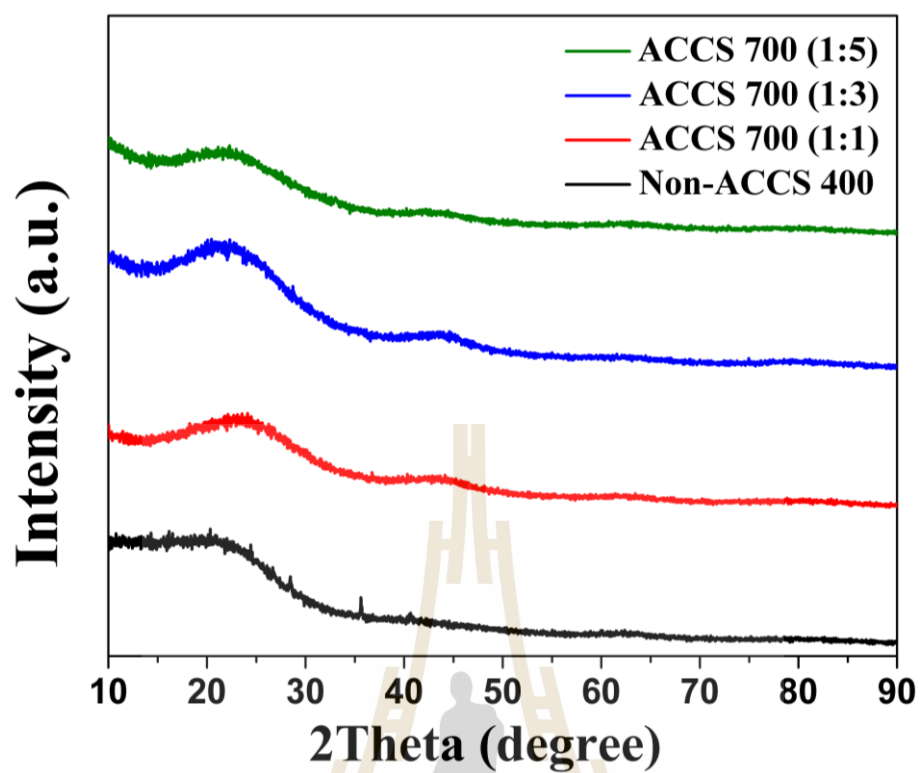
Figure 4.11 XRD patterns of non-activated carbon and activated carbon with differential concentration of activated carbon derive from cassava starch.

4.2.1.2 Scanning electron microscope (SEM) analysis carbonization at temperature of 700 ℃

The morphology of activated carbon under the differential KOH ratio were study by SEM. The non-activated carbon (Non-ACCS 400) measurement, the resulting was the smooth surface, after activation, the surface of carbon material exhibits rough and pore show in figure 4.8. The indicated that the activation has effect to the intersection between carbon layer and KOH. The ACCS 700 (1:1) revealed clear of pore structure. That mean with concentration of KOH solution is not enough to ratio of raw material mass. This cause, the pore structure depend on the concentration of KOH activation (Jiang *et al.*, 2014). The sample of ACCS 700 (1:3) is highest   pore structure compared with activated carbon of ACCS 700(1:1) and ACCS 700 (1:5). In addition, the surface in ACCS 700 (1:3) showed that the pore structure has some part broken due to the activation process and surface of sample were corrosion longer activation time more than ACCS 700 (1:1) and ACCS 700 (1:5). The ACCCS 700 (1:5) exhibits the good pore structure that mean the carbonization and activation but it occurred shot time (Sun *et al.*, 2010).
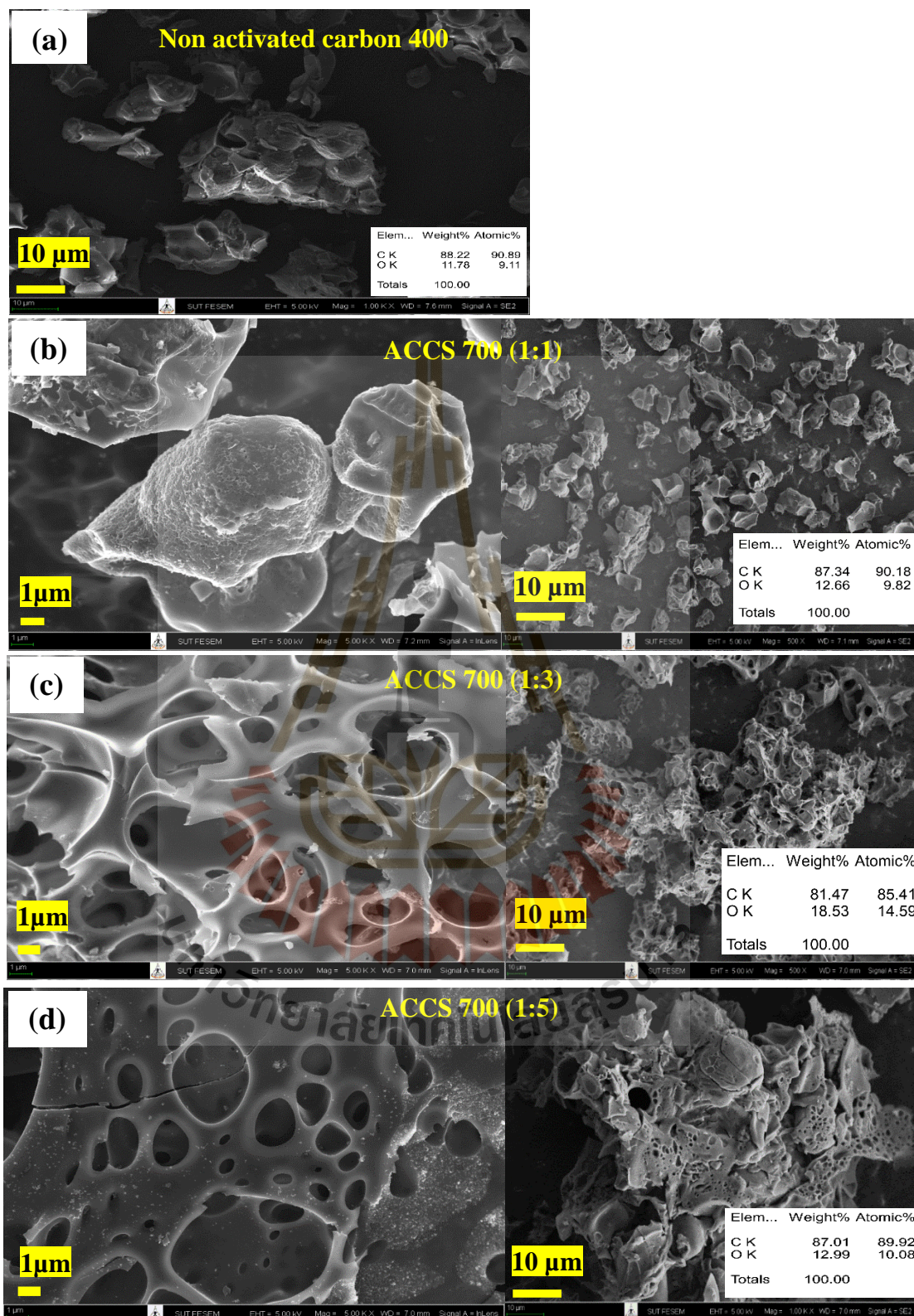
Figure 4.12 SEM images of (a) non-activated carbon Non activated carbon 400, (b) ACCS 700 (1:1), (C) ACCS 700 (1:3) and (d) ACCS 700 (1:5).

4.2.1.3 Brunauer-emmett-teller (BET) analysis at temperature of 700 ºC temperature

The specific surface area and pore character of the activated carbons were investigated by nitrogen adsorption method measured at 77 K. The absorption isotherm shape can explain a strength of the interaction between the surface area of sample and absorption with absence and existence of pore as shown in Figure 4.9. According to IUPAC classification, the absorption isotherm of all samples is type I this same of ACCS 600 of all sample, indicating the presence of micropore structures with high internal surface area in the sample. In addition, This observe that the pore volume of ACCS 700 (1:1) , ACCS 700 (1:3) and ACCS 700 (1:5) are much higher than Non ACCS 400 and the isotherms of ACCS 700 (1:1) , ACCS 700 (1:3) and ACCS 700 (1:5) indicated of relative pressure P/P0 more than 0.2 and increasing from P/P0 = 0.4 to 0.9 with adding of KOH activated ratio. This indicating the co-existence of mesopore (Zhou *et al.*, 2016).

The BJH pore distribution plots of activated carbon are shown in Figure 4.10. The pore size distribution calculated from BJH method shows that the pore size of all samples is in the range of 1-20 nm. This indicates that the KOH activation can modify the surface area and pore structures such as micropore and mesopore. The specific surface area and pore structure of the activated carbon are shown in Table 4.4. The KOH activated samples also exhibit higher BET surface area than the non-activation sample. The ACCS 700 (1:5) sample has the maximum surface area of 1824 $m^2\,g^{-1}$ and pore volume of 0.86 $cm^3\,g^{-1}$. Due to the reaction between KOH and carbon surface as in equation 4.1. The presence of mesopores and high specific area of the KOH activation samples are promising for supercapacitor application. The micropore

structure can lead to fast transfer electrolyte ion during the charge/discharge process, increasing specific capacitance (Zheng *et al.*, 2014). The large surface area has the advantage of quick charge transfer and ion diffusion, leading to higher specific capacitance for apply supercapacitor electrode (Ma *et al.*, 2015).

Figure 4.13 BET measurements of non-activated and activated carbon of ACCS 700 (1:1), (ACCS 700 (1:3) and ACCS 700 (1:5) derived from cassava starch.
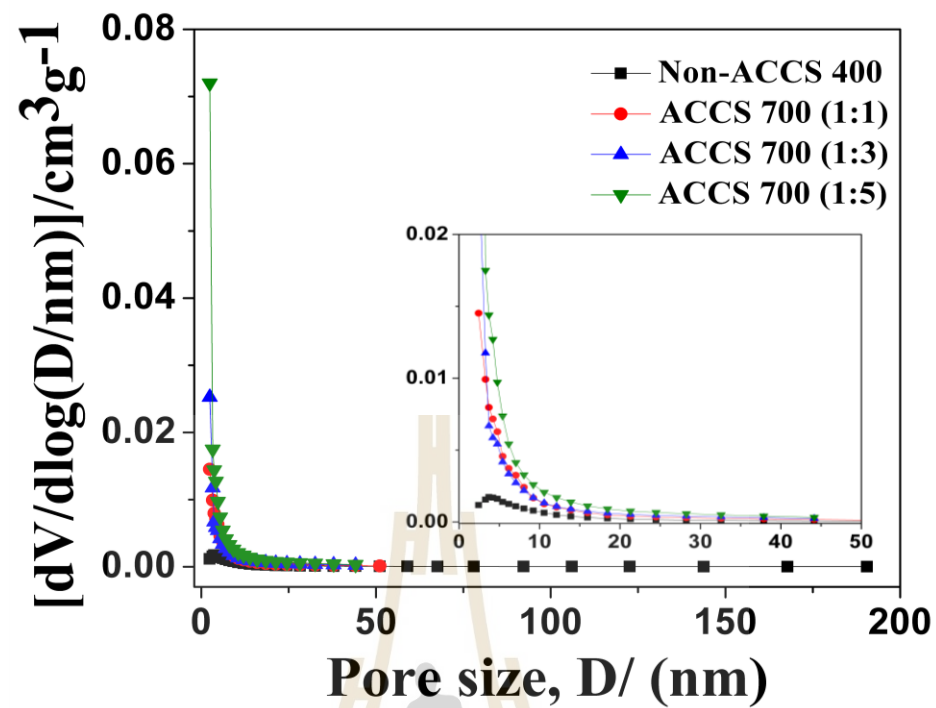
Figure 4.14 (a) BJH pore distribution plots of non-activated and activated carbon of ACCS

700 (1:1), (ACCS 700 (1:3) and ACCS 700 (1:5) derived from cassava starch.

Table 4.3 BET results of non-activated and activated carbon of ACCS 700 (1:1), ACCS 700 (1:3) and ACCS 700 (1:5) derived from cassava starch.

Sample	BET			Micropore	Mesopore
	S_{BET}	D_P	V_T	V_{mi}	V_{me}
	$(m^2\,g^{-1})$	(nm)	$(cm^3\,g^{-1})$	$(cm^3\,g^{-1})$	$(cm^3\,g^{-1})$
Non-ACCS 400	14.80	6.52	0.02	4.55	0.02
ACCS 700 (1:1)	881	1.87	0.41	0.41	0.07
ACCS 700 (1:3)	1302	1.77	0.57	0.57	0.08
ACCS 700 (1:5)	1824	1.88	0.86	0.85	0.19

* S_{BET} = Surface area, D_P = Mean pore diameter, V_T = Total pore volume, V_{mi} = Micro pore volume and V_{me} = Mesopore volume

4.2.1.4 Fourier transform infrared (FTIR) analysis of the carbonization at temperature of 700 ºC

The surface function groups of the non-activated carbon (Non-ACCA 400) and all the activated carbon (ACCS 700 (1:1), ACCS 700 (1:3) and ACCS 700 (1:5)) were determined using FTIR analysis. The spectra of all sample are shown in figure 4.11. The transmittance broad peak of 2923 c m^{-1} indicated the C-H band, completely appeared for the all sample. Stretching adsorption band at 1738 c m^{-1} apparent of C=O in the all sample. The strong band is seen at about 1638 c m^{-1} that may be described to olefin C=C vibration in aromatic region for the material.(Yagmur *et al.*, 2008). The absorbs ion around 1246-1385 c m^{-1} indicated the existence of C-O single band in carboxylic acid, alcohol phenol in phosphate ester (Puziy *et al.*, 2005). The peaks in the range 500-700 c m^{-1} can be attributed the C-H bending vibration stretching was showed of all sample. Indicated that, the treatment of the carbon with potassium hydroxide caused a decrease of helium density. The resulting from some mineral impurities removal (Lee *et al.*, 1999).
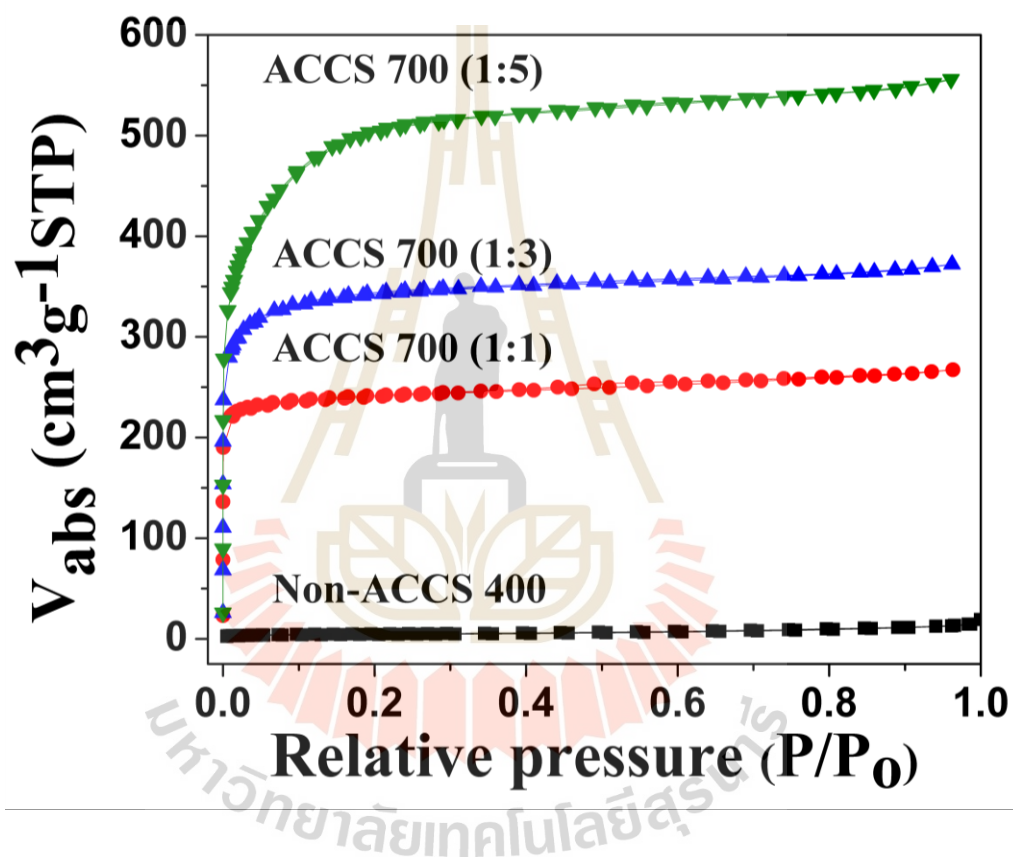
Figure 4.15 FTIR pattern of non-activated and activated carbon of ACCS 700 (1:1), ACCS 700 (1:3) and ACCS 700 (1:5) derived from cassava starch.

4.2.1.5 X-ray photoemission spectroscopy (XPS) analysis of the carbonization at temperature of 700 °C

The chemical compositions of the activated carbons were studied by XPS. The high resolution XPS spectra of C1s peaks of the activated carbon (ACCS 700 (1:1), ACCS 700 (1:3), and ACCS 700 (1:5)) are shown in Figure 3. The C1s spectra can be deconvoluted into three sub-peaks at approximately 284.8 eV, 286.2 eV and 288.3 eV which are attributed to C-C/C=C bond, C-O bond and O-C=O bond, respectively (Shulga *et al.*, 2015). The C/O and carbon functional groups concentration of all samples are slightly different. This result shows that the KOH activation has no significant effect on the chemical composition of the samples.
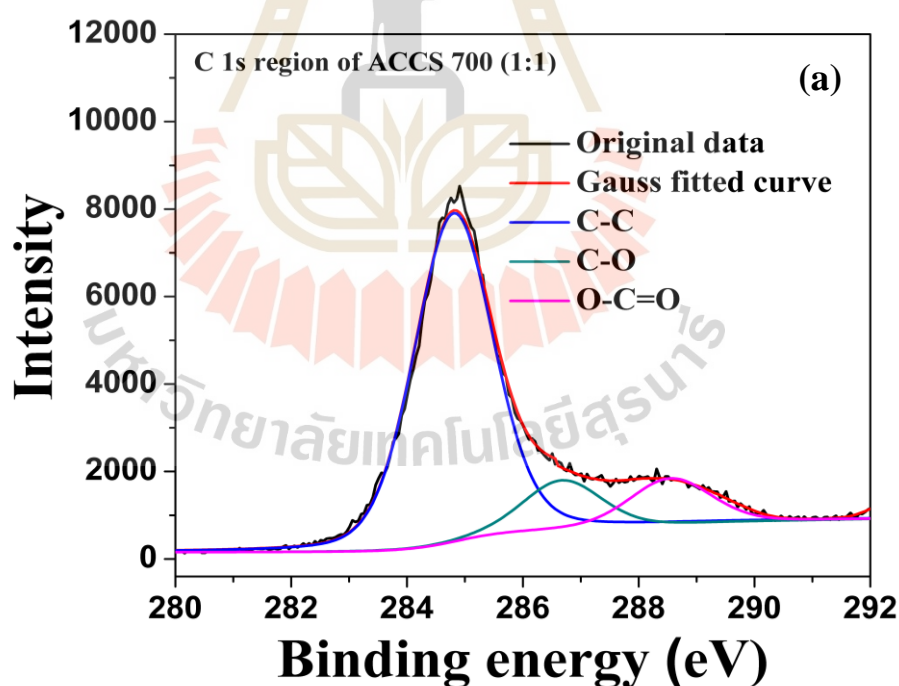
Figure 4.16 High resolution XPS spectra of C1s peak of non-activated and activated carbon of (a) ACCS 700 (1:1), (b) ACCS 700 (1:3) and (c) ACCS 700 (1:5) derived from cassava starch.
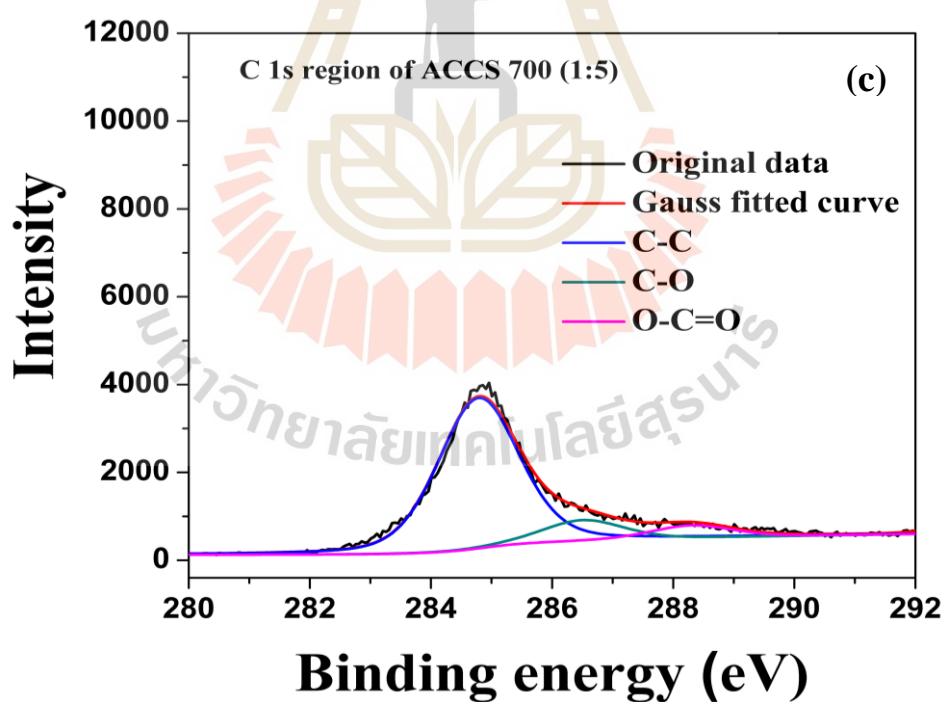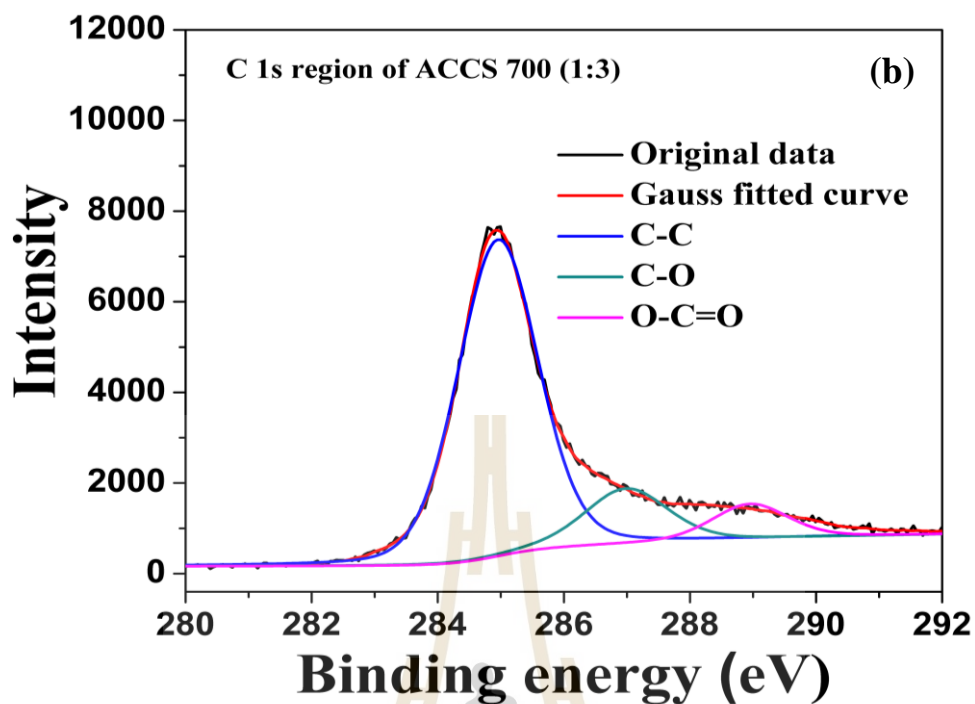
Figure 4.16 (Continued) High resolution XPS spectra of C1s peak of non-activated and activated carbon of (a) ACCS 700 (1:1), (b) ACCS 700 (1:3) and (c) ACCS 700 (1:5) derived from cassava starch.

4.2.2 Electrochemical properties

4.2.2.1 Cyclic voltammetry measurement

The cyclic voltammetry (CV) curve of KOH activation derived from cassava starch at 700 $^{\circ}$C carbonization recorded between -1 to 0 V at differential scan rate of 2 to 200 mV s^{-1} are present in the figure 4.14. All sample were measurement in 6 NaOH solution using by three electrode system. The CV curve of all sample electrode vary scan rate between 2 to 200 mV s^{-1} revealed a quasi-rectangular shape unapparent redox peak. This result indicated a ideal double layer capacitor of charge discharge method. The rectangular shape is a high area with increase high scan rate at 200 mV s^{-1} due to fast charge-discharge rate and low equivalent series resistance (Peng *et al.*, 2016). Addition, the non- activated carbon (Non-activated carbon 400) is small area compare with the activated carbon of all sample. Indicating, the activated carbon is high specific capacitance more than the non-activated carbon may be the result related pore structure of BET method due to the activated carbon create pore structure.

Figure 4.17 CV curves of the activated carbon derived from cassava starch: (a) Non-ACCS 400, (b) ACCS 700 (1:1), (c) ACCS 700 (1:3) and (d) ACCS 700 (1:5).

Figure 4.17 (Continued) CV curves of the activated carbon derived from cassava starch: (a) Non-ACCS 400, (b) ACCS 700 (1:1), (c) ACCS 700 (1:3) and (d) ACCS 700 (1:5).

4.2.2.2 Galvanostatic charge-discharge measurement

The galvanostatic charge-discharge behavior of the electrode at current densities from 0.5 to 30 A g^{-1} are shown in figure 4.15. The galvanostatic charge-discharge curves measured in all samples show that current density increases with decrease of the discharge time. The specific capacitance of Non-ACCS 400, ACCS 700 (1:1), ACCS 700(1:3) and ACCS 700(1:5) are 14, 126, 129 and 99 F g^{-1}, respectively. The maximum specific capacitance of 129 F g^{-1} at 0.5 A g^{-1} current density was obtained from the ACCS 700 (1:3) as show the table 4.3. The shape of curve exhibit closely linear in the potential range. The all of sample indicated a good capacitance of these material (Zheng *et al.*, 2014). The specific capacitance of activated carbon is high compare with non-activated carbon (Non-ACCS 400) because of higher surface area and pore volume measured from BET technique analysis as shown in table 4.3. and related from SEM result.
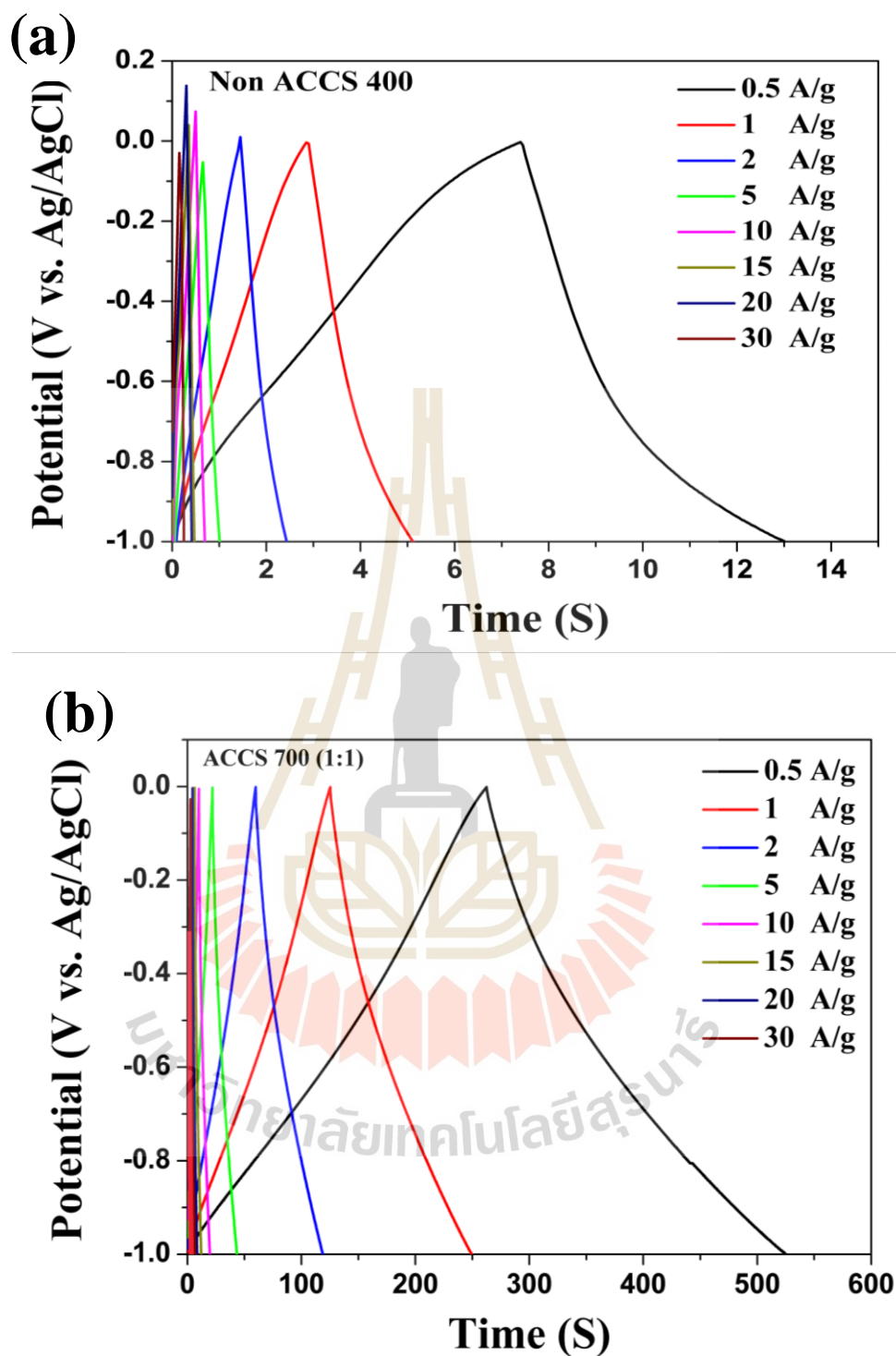
Figure 4.18 Galvanostatic charge-discharge curves of the activated carbon derived from cassava starch: (a) Non-ACCS 400, (b) ACCS 700 (1:1), (c) ACCS 700 (1:3), (d) ACCS 700 (1:5) and (E) GCD curve comparison capacitance value of all sample.
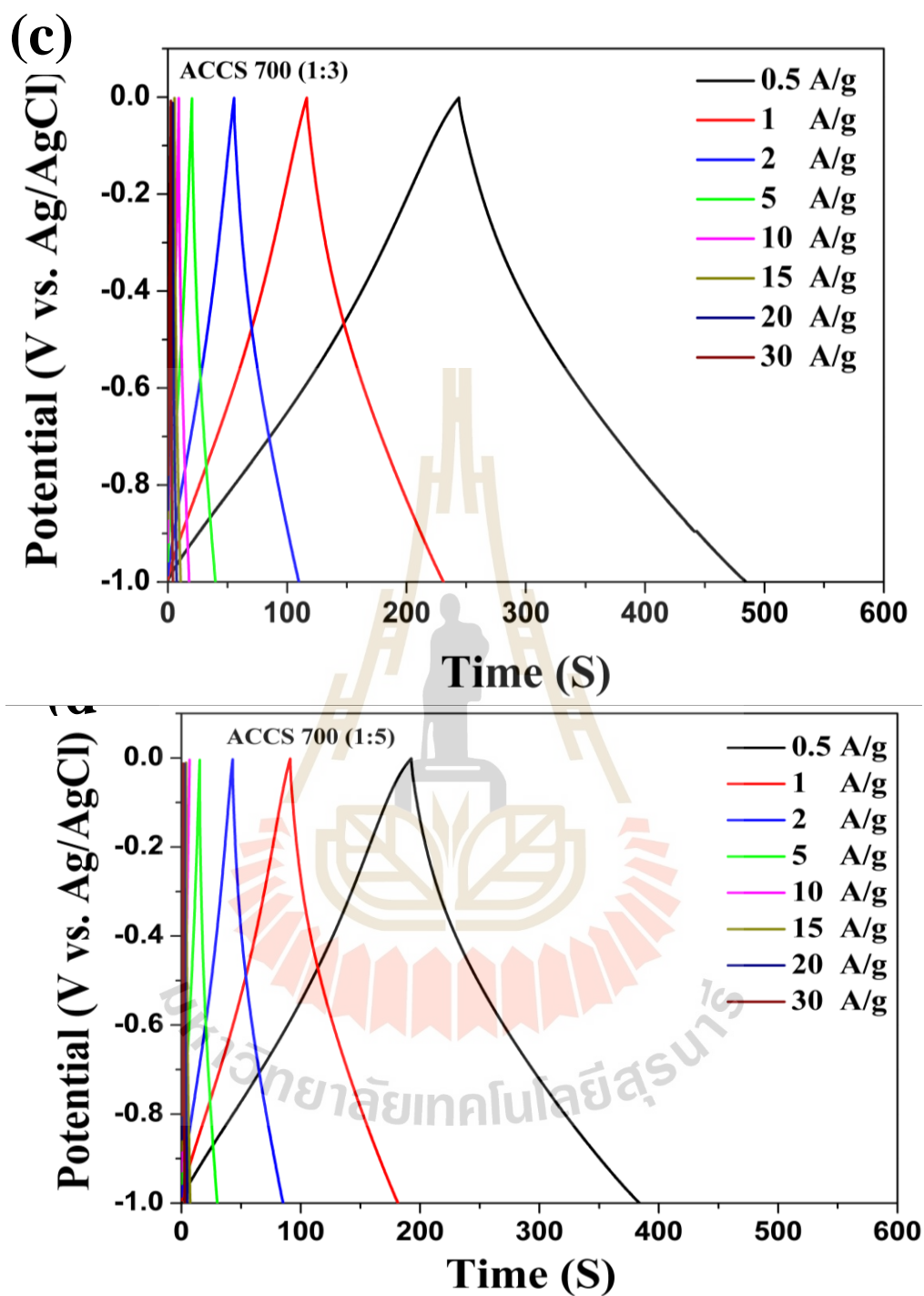
Figure 4.18 (Continued) Galvanostatic charge-discharge curves of the activated carbon derived from cassava starch: (a) Non-ACCS 400, (b) ACCS 700 (1:1), (c) ACCS 700 (1:3), (d) ACCS 700 (1:5) and (E) GCD curve comparison capacitance value of all sample.
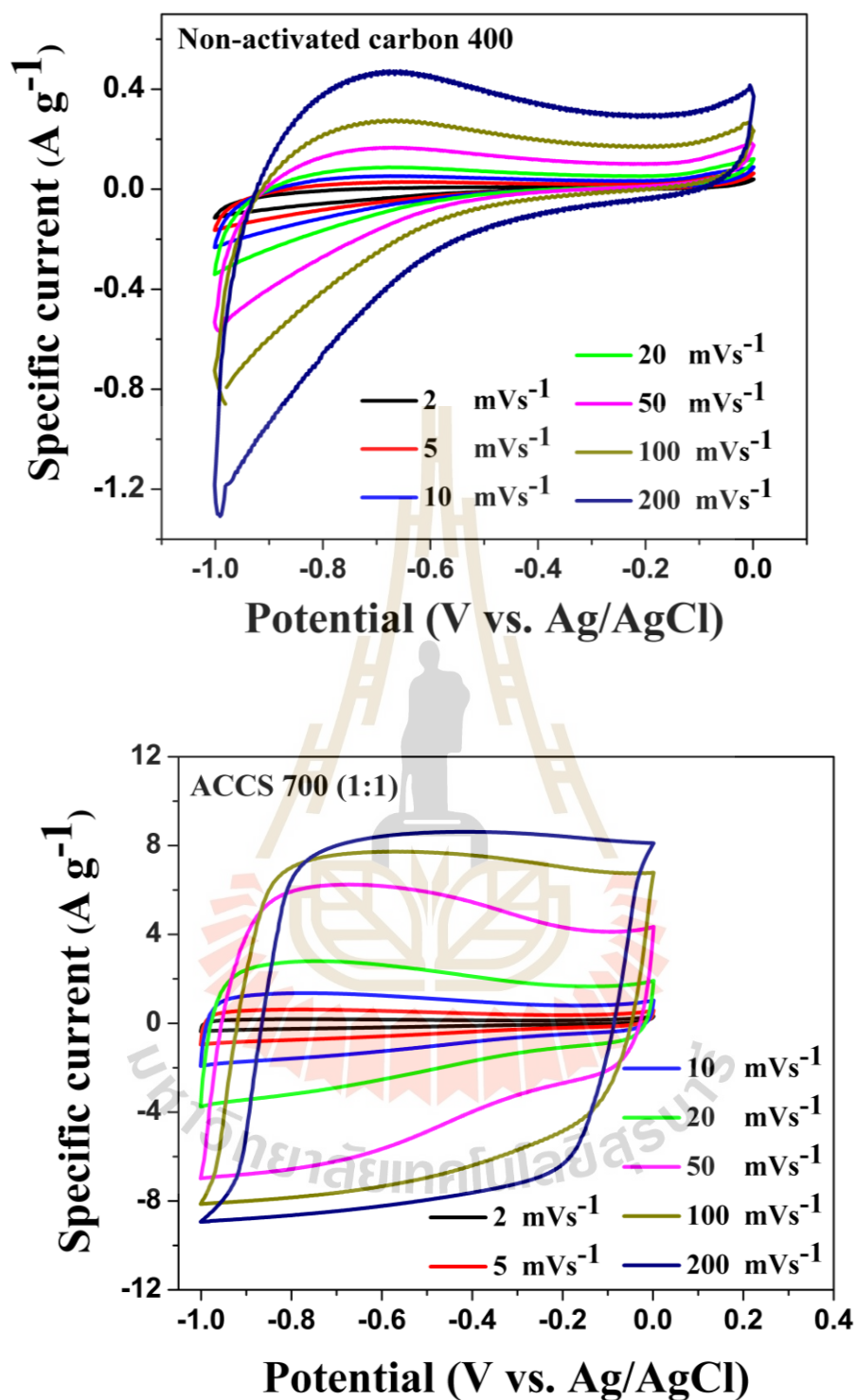
(e)
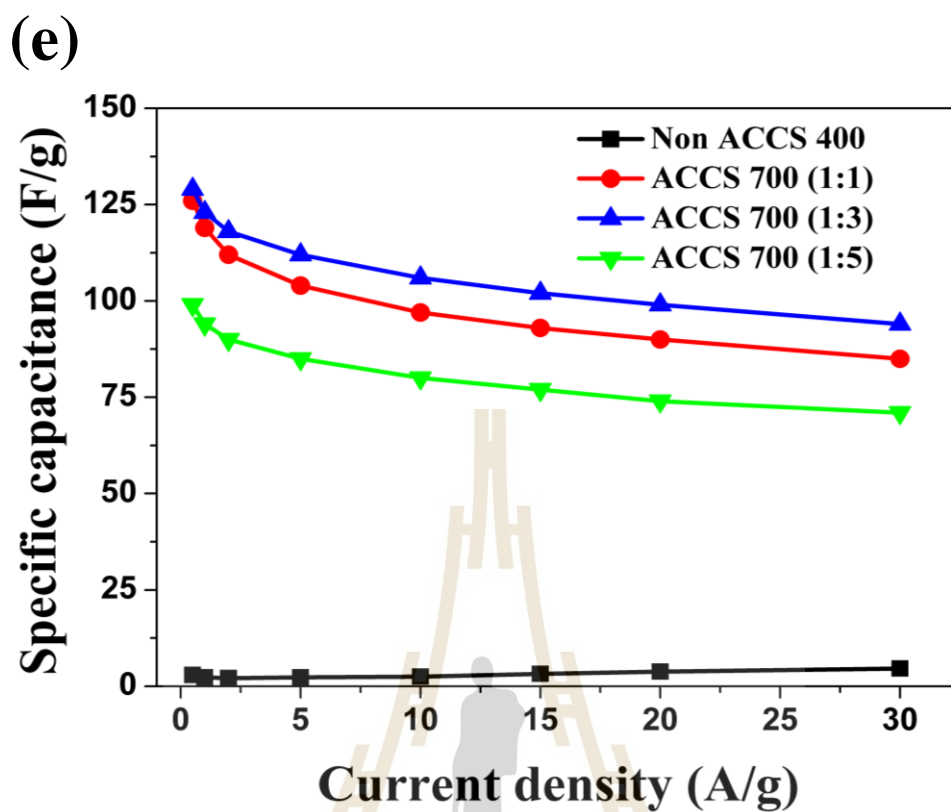
Figure 4.18 (Continued) Galvanostatic charge-discharge curves of the activated carbon derived from cassava starch: (a) Non-ACCS 400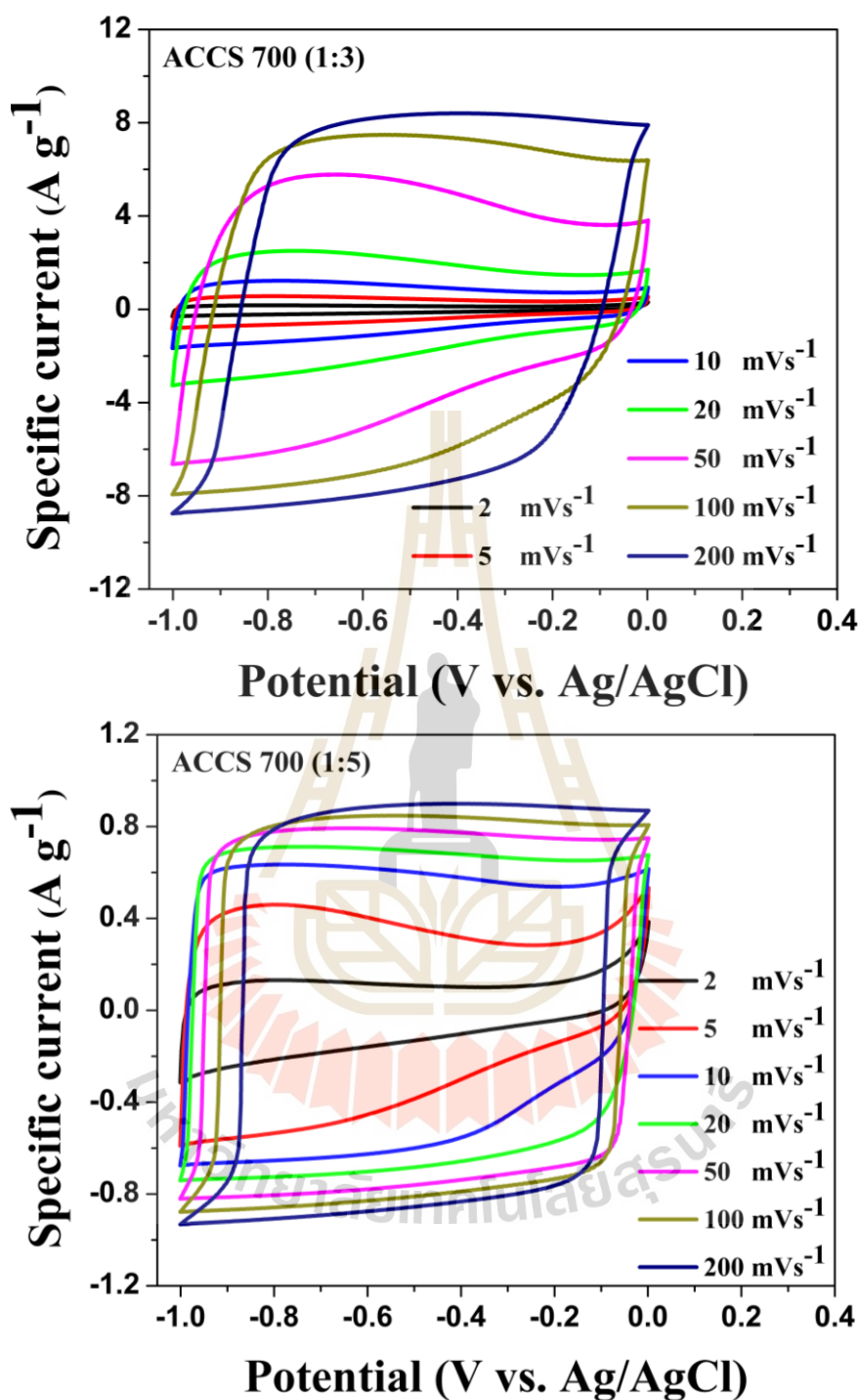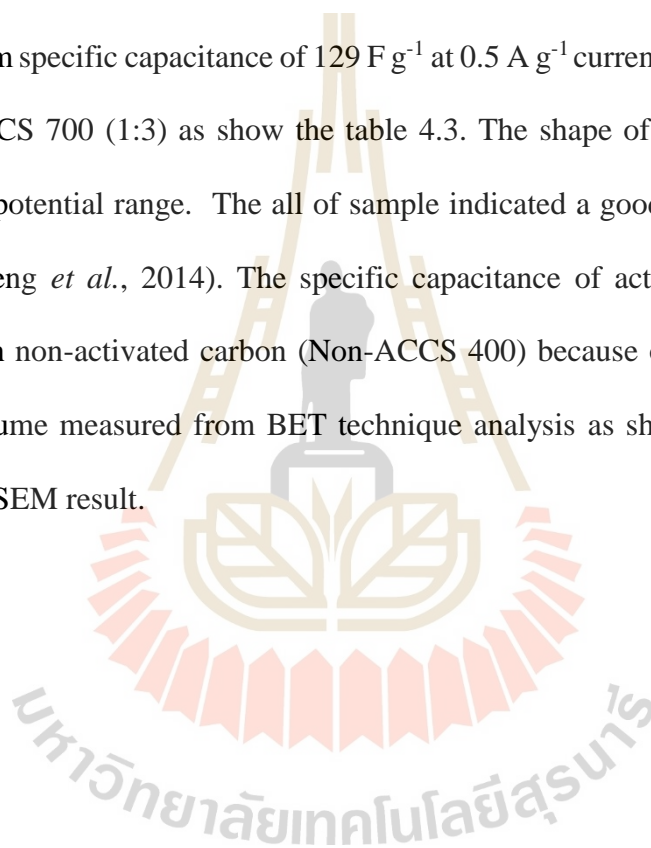, (b) ACCS 700 (1:1), (c) ACCS 700 (1:3), (d) ACCS 700 (1:5) and (E) GCD curve comparison capacitance value of all sample.

Table 4.4 Specific capacitance from GCD curve of non-activated and activated carbon of ACCS 700 (1:1), (ACCS 700 (1:3) and ACCS 700 (1:5) derived from cassava starch.

Sample	Current density (A/g)							
	0.5	1	2	5	10	15	20	30
ACCS 700 (1:1)	126	119	112	104	97	93	90	85
ACCS 700 (1:3)	129	123	118	112	106	102	99	94
ACCS 700 (1:5)	99	94	90	85	80	77	74	71

4.2.2.3 The Nyquist plot of non-activated and activated carbon

The behavior of the activated carbon electrodes was further investigated by the electrochemical impedance spectroscopy (EIS). Figure 6e shows the Nyquist plot of the impedance for the activated carbon electrodes. The solution resistance (Rs) interpreted from the intercept at Z′ axis (inset in Figure 6e) indicates that the non-activated carbon electrode has the Rs value higher than the activated carbon electrode. The Rs not have tends to increase with KOH ratio, The better electrochemical performance of for ACCS 700 (1:1), ACCS 700 (1:3) and ACCS 700 (1:5) can be attribution to the better electrochemical conductivity compare with non-activated carbon (Peng *et al.*, 2014).
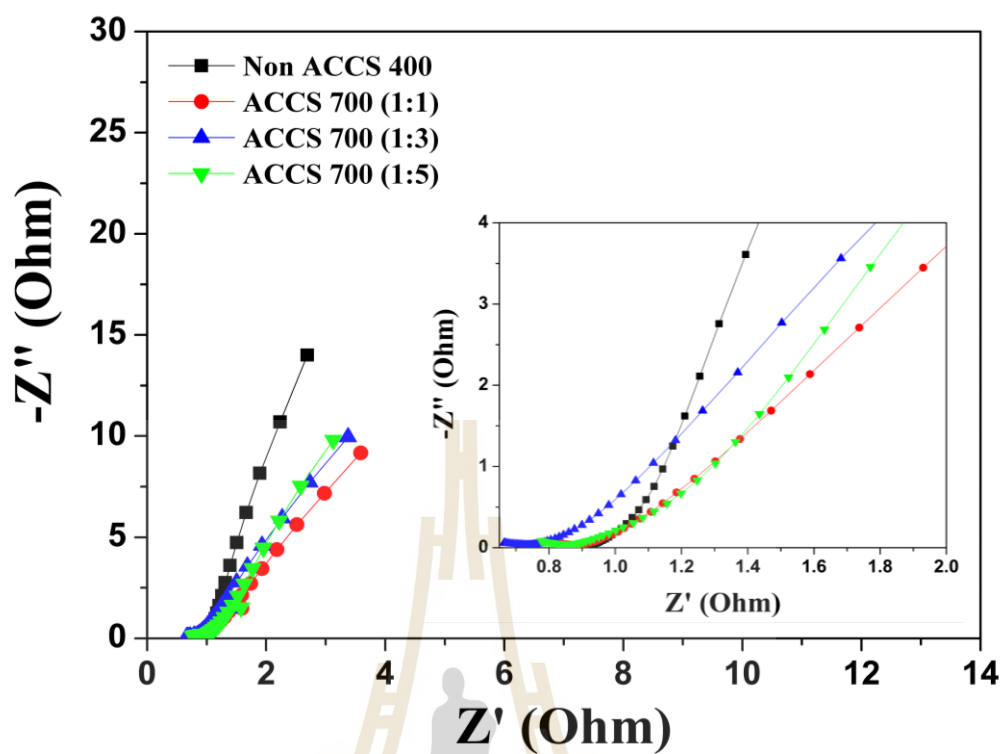
Figure 4.19 the Nyquist plot of non-activated carbon and activated carbon drive from cassava starch.

4.2.2.4 The cycle life of non-activated carbon and activated carbon derived from cassava starch at 2 A g^{-1}

The cyclic lifetime for the ACCS 700 (1:1) sample which has the highest specific capacitance is shown in the Figure 4.10. The measurement was performed in 6 M NaOH electrolyte with 1000 cycles at the current density of 2 A g^{-1}. The Coulomb efficiency of electrode as cycle number can be calculated from the equation 5 (Peng *et al.*, 2013). The Coulomb efficiency of Non ACCS 400, ACCS 700 (1:1), ACCS 700 (1:3) and ACCS 700 (1:5) samples remains the value of 53 %, 94 %, 92 % and 95 %, respectively after 1000 cycles. This result indicate that the good activated carbon electrode has long life cycle stability and good electrochemical conductivity (Huang *et al.*, 2014; Li *et al.*, 2008) lead to the efficacy of development for supercapacitor application.
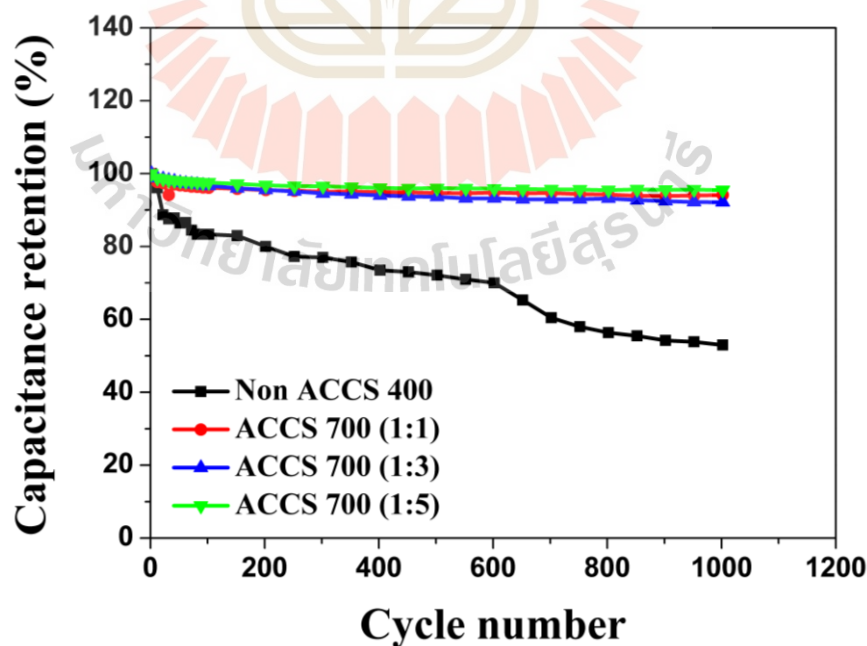
Figure 4.20 The cycle life of non-activated carbon and activated carbon drive from cassava starch.

4.3 Carbonization at Temperature of 800 °C

4.3.1 Structural and morphology characterization.

4.3.1.1 X-ray diffraction (XRD) analysis of the carbonization at 800 °C temperature

The XRD spectra of prepared samples in figure 4.18 were measured with Cu, Kα wavelength of 1.54 Å between 2Θ from 10 to 80 °, step time 0.2 and step size 0.02. The samples were calcined with the differential concentration of KOH at the 800 °C in argon atmosphere. The XRD pattern of all samples show the broad peak of amorphous carbon. The pattern of Non ACCS 400 and ACCS 800 (1:3) sample show broad diffraction peaks about 2Θ = 23 ° corresponding to plane 002 crystal plane diffraction peak that indicated the amorphous carbon structures mainly formed during carbonization. However, the broad peak of 2Θ = 43 ° for Non ACCS 400 disappearance. But, this peak was presented in the ACCS 800 (1:1), ACCS 800 (1:3) and ACCS 800 (1:5). Indicating that intensity in the angle scatter are increasing which activated carbon increasing ratio concentration. (Peng *et al.*, 2014). More ever, this result may be randomly oriented graphitic carbon layers are present on the structure (Huang and Zhao, 2016; Jiang *et al.*, 2014).
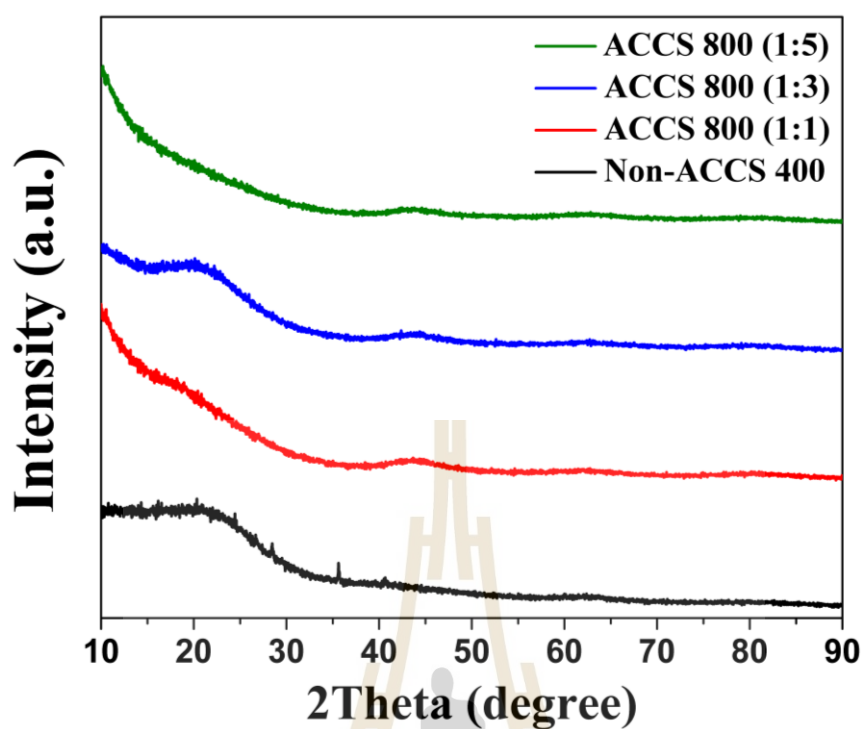
Figure 4.21 XRD patterns of non-activated carbon and activated carbon with differential concentration of activated carbon derive from cassava starch.

4.3.1.2 Scanning electron microscope (SEM) analysis of the carbonization at 800 ºC temperature

The morphology of activated carbon under the differential KOH ratio were study by SEM. The non-activated carbon (Non-ACCS 400) measurement, the resulting was the smooth surface, after activation, (we can see that figure 4.2(b), 4.2(c) and 4.2(d)) the surface of carbon material exhibits rough and pore. These resulted from the evaporation of the activated agent. The space area from external surface occupied by KOH activation (Yakout and El-Deen, 2016). Indicating that the activation has effect to the interaction between carbon layer and KOH. This cause, the pore structure depend on the concentration of KOH activation (Jiang *et al.*, 2014). After the KOH activation, the surface in ACCS 700 (1:3) and ACCS 800 (1:5). show the pore structure this mean the activation process and surface of sample were erudition longer activation time more than ACCS 800 (1:1) and The ACCCS 800 (1:5) exhibit the good pore structure that mean the carbonization and activation but it occurred shot time. (Sun *et al.*, 2010). This result have potential to developed supercapacitor application. (Cao *et al.*, 2016).
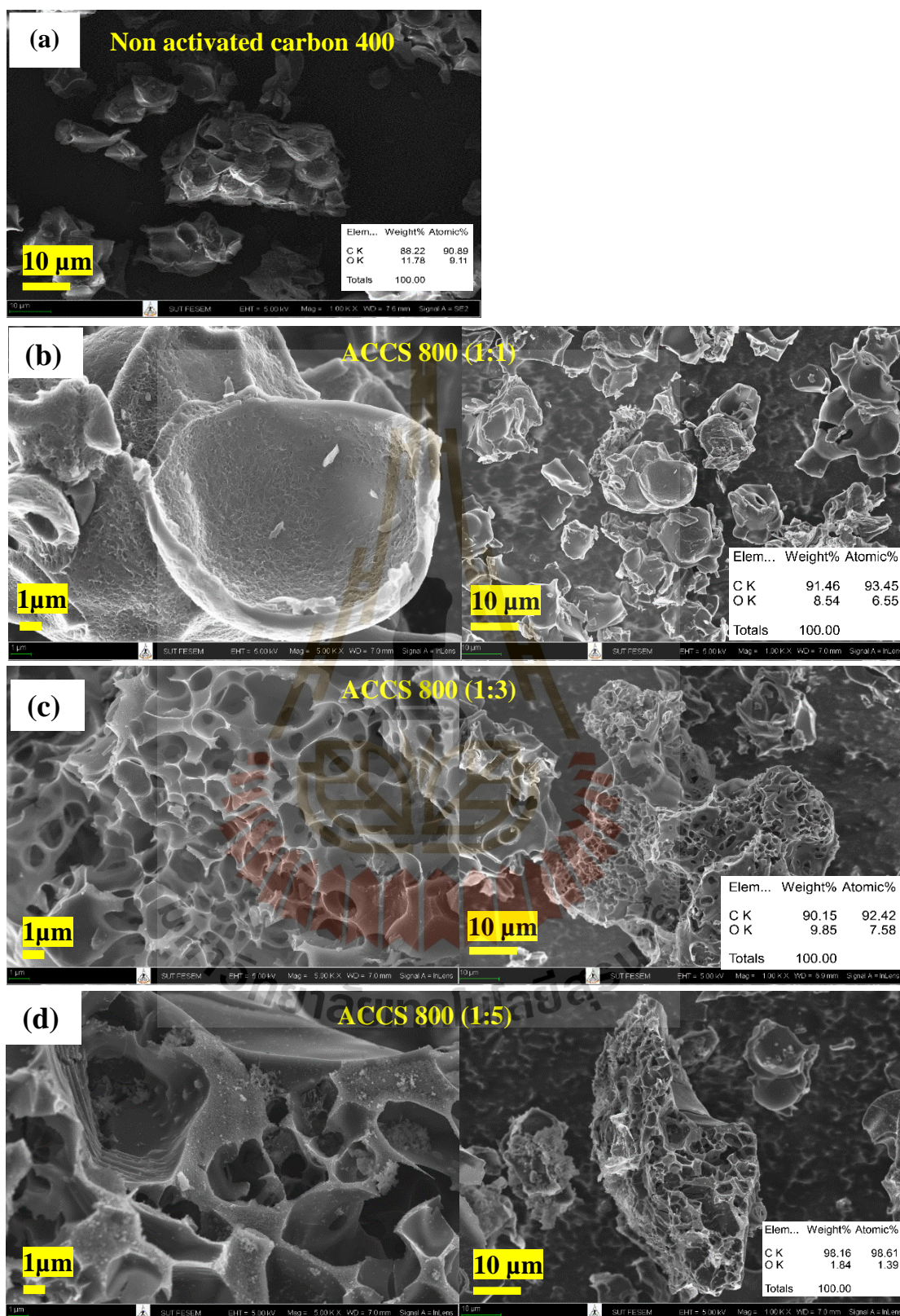
Figure 4.22 SEM images of (a) Non activated carbon 400, (b) ACCS 800 (1:1), (c) ACCS 800 (1:3) and (d) ACCS 800 (1:5).

4.3.1.3 Brunauer-emmett-teller (BET) analysis of the carbonization at temperature of 800 °C

Nitrogen adsorption-desorption isotherm of porous activated carbon prepared at differential impregnation ratio of KOH are shown in Figure 4.3 All sample exhibits atypical type-I curve. Indicated that the all sample have a microporous structure only (according to the IUPAC classification) (Sing, 1985). The ACCS 800 (1:5) is highest of 2047 m^2 g^{-1} due to the high concentration of KOH activation lead to interaction of carbon and oxygen on the surface. The activated carbon of concentration KOH ratio has interested effect on the pore structure. The pore structure depend on KOH concentration where compare with non-activated carbon (Wang *et al.*, 2015). That resulting are the higher surface area (see table 4.1). The BJH method can be calculate at the average pore size for non-ACCS 400, ACCS 800 (1:1), ACCS 800 (1:3) and ACCS 800 (1:5) is about 6.52 nm, 1.88 nm, 1.79 nm and 1.99 nm respectively. The resulting that the mesopore (in the range 2-10 nm) of activated carbon are smaller than the non-activated carbon from the table 4.4. The specific surface area of all sample after activated carbon have increased specific capacitance. The non-activated carbon (Non-ACCS 400) is lowest specific surface area at 14.8 m^2 g^{-1}. Moreover, we focus research on the activated carbon. These results indicate that the surface area is enlarged by KOH activation under differential activation condition. It is the way of effectively to generate nanoscale pore in the carbon material.

Figure 4.23 BET measurements of non-activated and activated carbon of ACCS 800 (1:1), (ACCS 800 (1:3) and ACCS 800 (1:5) derived from cassava starch.

Figure 4.24 (a) BJH pore distribution plots of non-activated and activated carbon of

ACCS 800 (1:1), (ACCS 800 (1:3) and ACCS 800 (1:5) derived from cassava starch.

Table 4.5 BET results of non-activated and activated carbon of ACCS 800 (1:1), ACCS 800 (1:3) and ACCS 800 (1:5) derived from cassava starch.

Sample	BET			Micropore	Mesopore
	S_{BET}	D_P	V_T	V_{mi}	V_{me}
	$(m^2\,g^{-1})$	(nm)	$(cm^3\,g^{-1})$	$(cm^3\,g^{-1})$	$(cm^3\,g^{-1})$
Non-ACCS 400	14.80	6.52	0.02	4.55	0.02
ACCS 800 (1:1)	1179	1.88	0.55	0.56	0.07
ACCS 800 (1:3)	1633	1.79	0.73	0.75	0.10
ACCS 800 (1:5)	2047	1.99	1.02	1.02	0.28

* S_{BET} = Surface area, D_P = Mean pore diameter, V_T = Total pore volume, V_{mi} = Micro pore volume and V_{me} = Mesopore volume

4.3.1.4 Fourier transform infrared (FTIR) analysis of the carbonization at temperature of 800 ºC

The surface function groups of the non-activated carbon (Non-ACCA 400) and all the activated carbon (ACCS 800 (1:1), ACCS 800 (1:3) and ACCS 800 (1:5)) were determined using FTIR analysis. The spectra of all sample are shown in figure 4.22. The transmittance broad peak of 2923 c m^{-1} indicated the C-H band, completely appeared for the all sample. Stanching adsorption band at 1738 c m^{-1} apparent of C=O in the all sample. The strong band is seen at about 1638 c m^{-1} that may be described to olefin C=C vibration in aromatic region for the material. (Yagmur *et al.*, 2008). The absorb sion around 1246-1385 c m^{-1} indicated the existence of C-O single band in carboxylic acid, alcohol phenol in phosphate ester (Puziy *et al.*, 2005). The peaks in the range 500-700 c m^{-1} can be attributed the C-H bending vibration stretching was showed of all sample. Indicated that, the treatment of the carbon with potassium hydroxide caused a decrease of helium density. The resulting from some mineral impurities removal (Lee *et al.*, 1999).
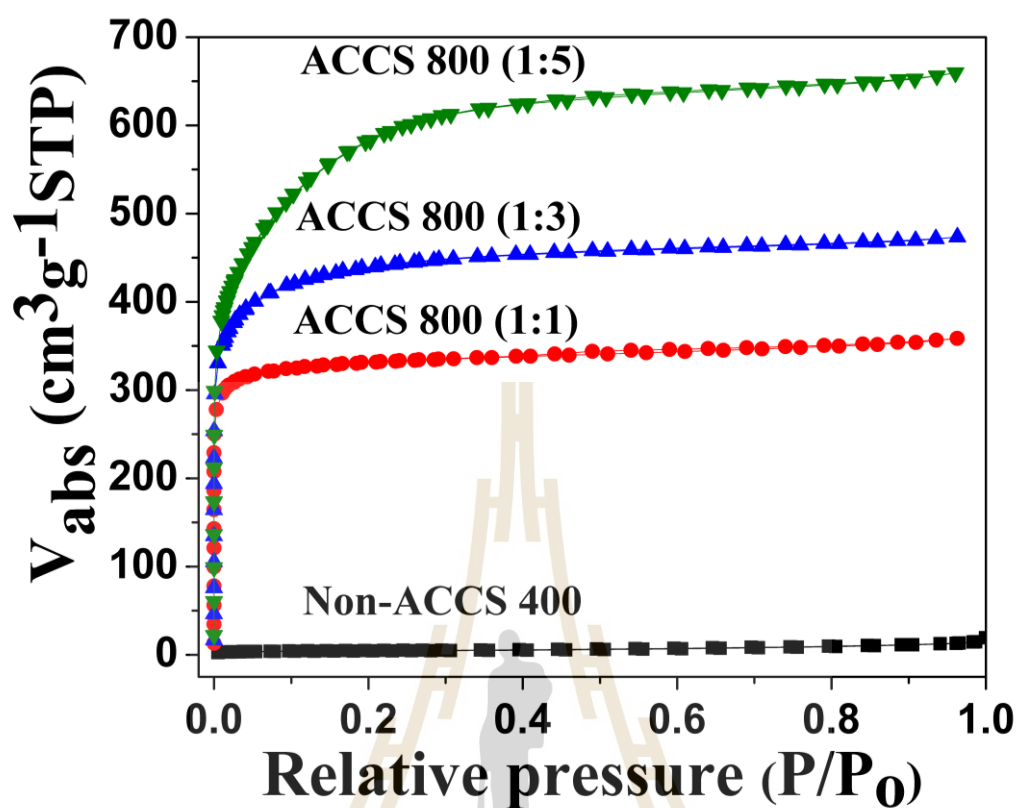
Figure. 4.25 FTIR pattern of non-activated   and activated carbon of ACCS 800 (1:1),

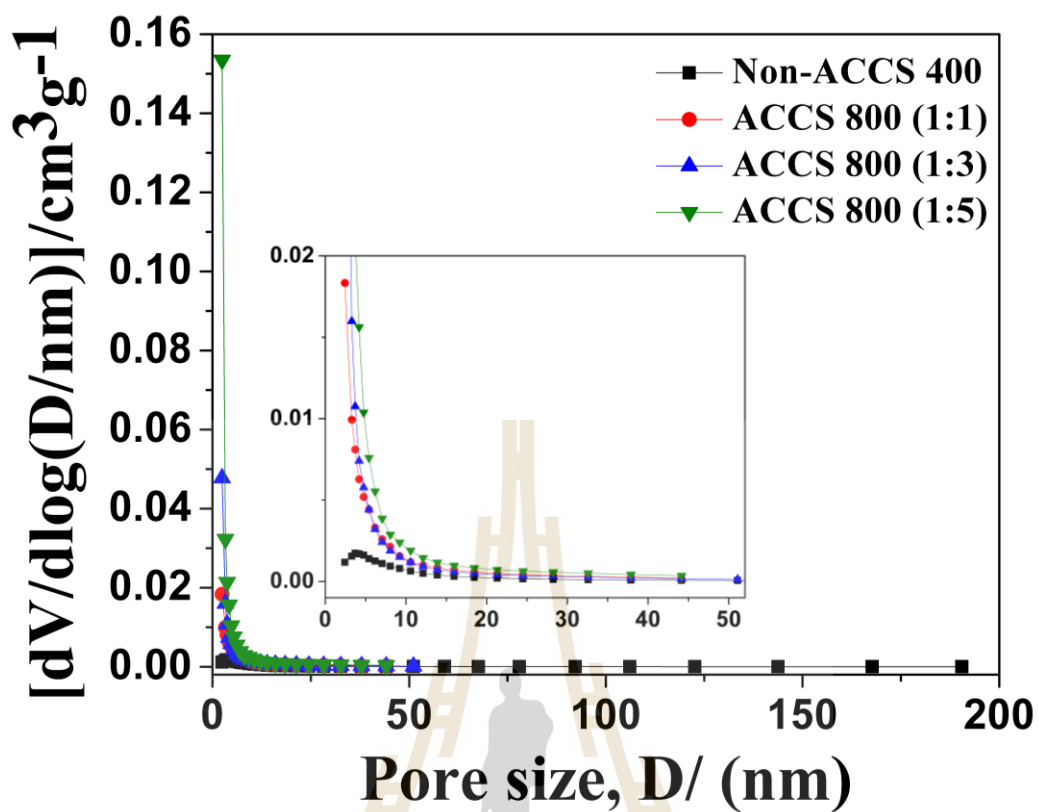ACCS 800 (1:3) and ACCS 800 (1:5) derived from cassava starch.

\

4.3.1.5 X-ray photoemission spectroscopy (XPS) analysis of the carbonization at temperature of 800 ºC

The chemical compositions of the activated carbons were studied by XPS. The high resolution XPS spectra of C1s peaks of the activated carbon (ACCS 800 (1:1), ACCS 800 (1:3) and ACCS 800 (1:5)) are shown in figure 4.23. The C1s spectra can be deconvoluted into three sub-peaks at approximately 284.8 eV, 286.2 eV and 288.3 eV which are attributed to C-C/C=C bond, C-O bond and O-C=O bond, respectively (Shulga *et al.*, 2015). The C/O and carbon functional groups concentration of all samples are slightly different. This result shows that the KOH activation has no significant effect on the chemical composition of the samples.
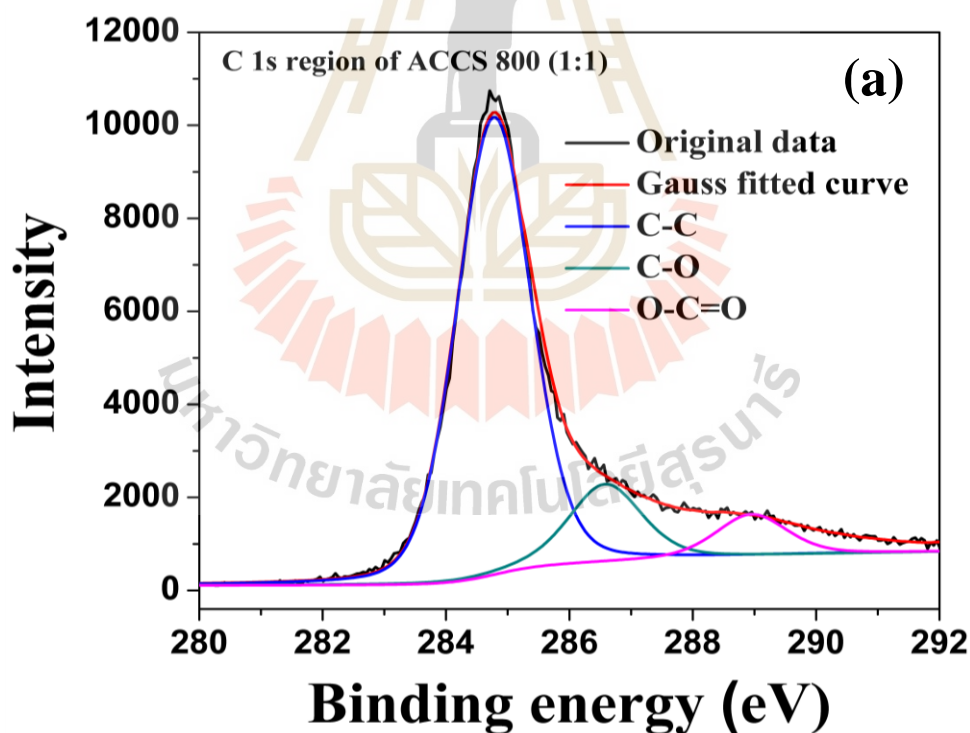
Figure 4.26 High resolution XPS spectra of C1s peak of non-activated   and activated carbon of (a) ACCS 800 (1:1), (b) ACCS 800 (1:3) and (c) ACCS 800 (1:3) derived from cassava starch.

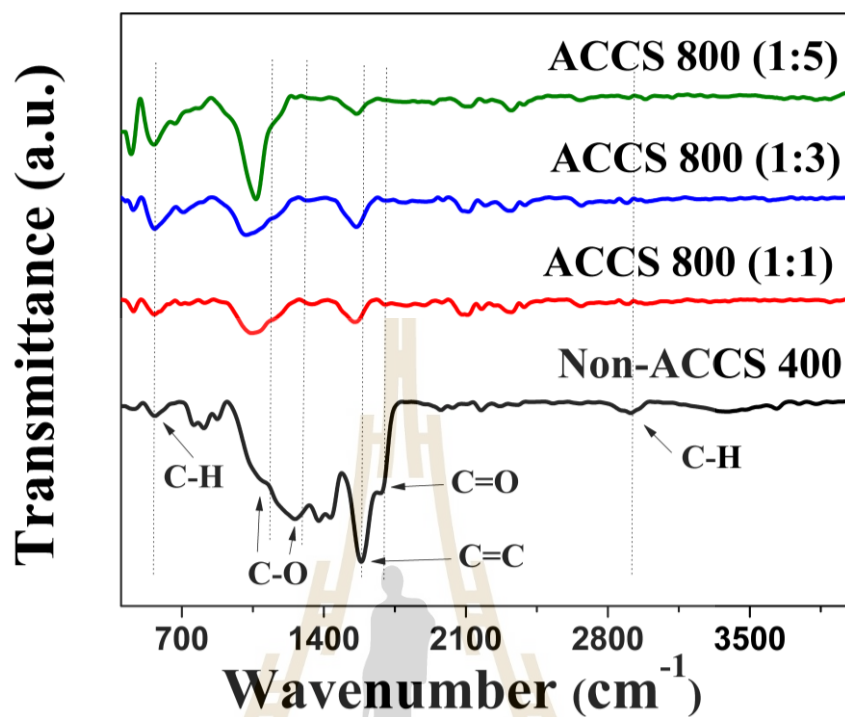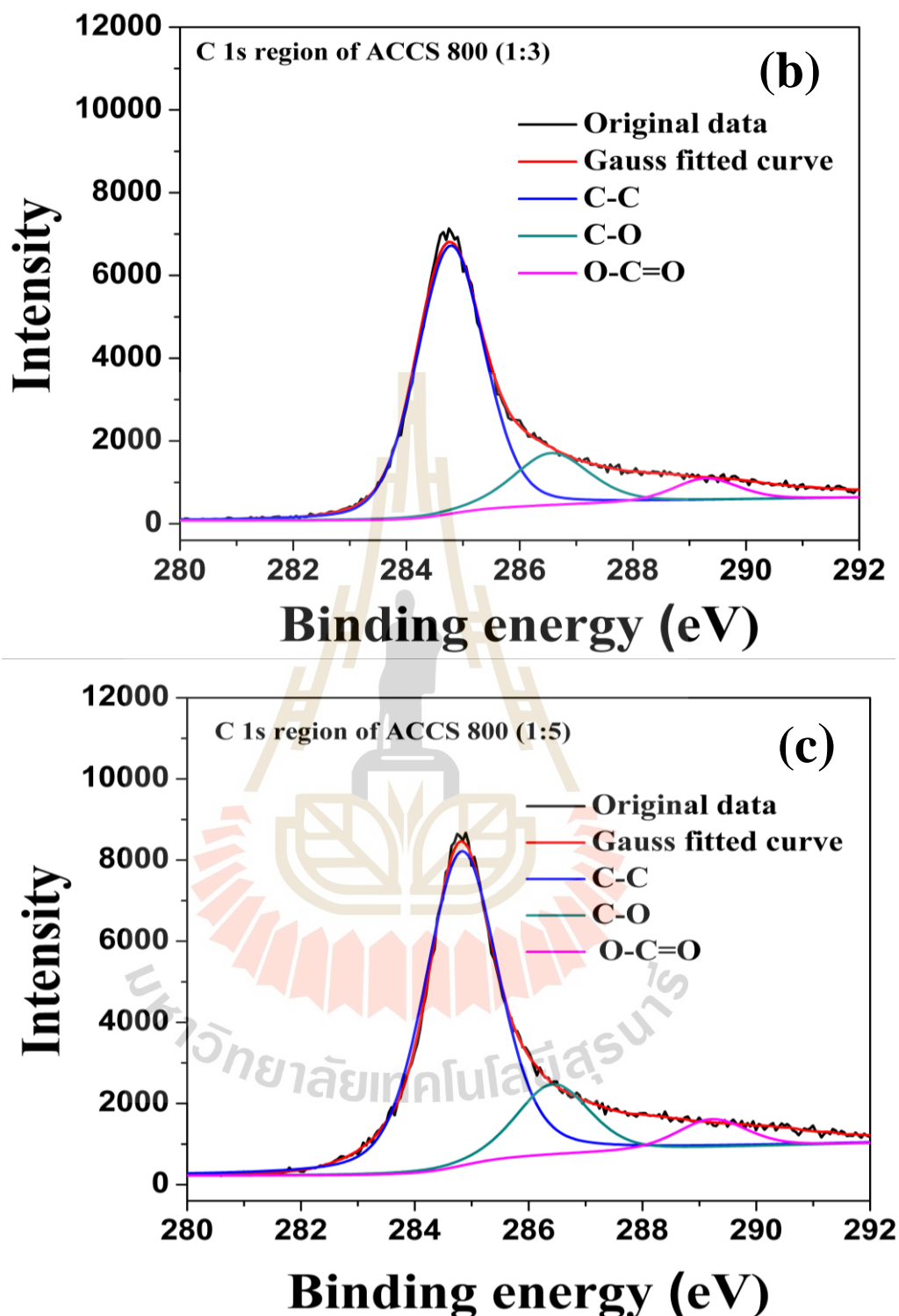**Figure 4.26** (Continued) High resolution XPS spectra of C1s peak of non-activated and activated carbon of (a) ACCS 800 (1:1), (b) ACCS 800 (1:3) and (c) ACCS 800 (1:3) derived from cassava starch.

4.3.2 Electrochemical properties

4.3.2.1 Cyclic voltammetry measurement

The cyclic voltammetry (CV) curve of KOH activation derived from cassava starch at 600 $^{\circ}$C carbonization recorded between -1 to 0 V at differential scan rate of 2 to 200 mV s^{-1} are present in the figure 4.24. All sample were measurement in 6 NaOH solution using by three electrode system. The CV curve of all sample electrode vary scan rate between 2 to 200 mV s^{-1} revealed a quasi-rectangular shape unapparent redox peak. This result indicated an ideal double layer capacitor of charge discharge method. The rectangular shape is a high area with increase high scan rate at 200 mV s^{-1} due to fast charge-discharge rate and low equivalent series resistance (Peng *et al.*, 2016). Addition, the non- activated carbon (Non-activated carbon 400) is small area compare with the activated carbon of all sample. Indicating, the activated carbon is high specific capacitance more than the non-activated carbon may be the result related pore structure of BET method due to the activated carbon create pore structure.

Figure 4.27 CV curves of the activated carbon derived from cassava starch: (a) Non-ACCS 400, (b) ACCS 800 (1:1), (c) ACCS 800 (1:3) and (d) ACCS 800 (1:5).

Figure 4.27 (Continued) CV curves of the activated carbon derived from cassava starch: (a) Non-ACCS 400, (b) ACCS 800 (1:1), (c) ACCS 800 (1:3) and (d) ACCS 800 (1:5).

4.3.2.2 Galvanostatic charge-discharge measurement

The galvanostatic charge-discharge behavior of the electrode at current densities from 0.5 to 30 A g^{-1} are shown in figure 2.25. The galvanostatic charge-discharge curves measured in all samples show that current density increases with decrease of the discharge time. The specific capacitance of Non-ACCS 400, ACCS 800 (1:1), ACCS 800(1:3) and ACCS 800(1:5) are 14, 101, 109 and 97 F g^{-1}, respectively. The maximum specific capacitance of 109 F g^{-1} at 0.5 A g^{-1} current density was obtained from the ACCS 800 (1:3) as show the table 4.6. The shape of curve exhibit closely linear in the potential range. The all of sample indicated a good capacitance of these material (Zheng *et al.*, 2014). The specific capacitance of activated carbon is high compare with non-activated carbon (Non-ACCS 400) because of surface area and pore volume from BET technique analysis as shown in table 4.5.

(a) Non ACCS 400
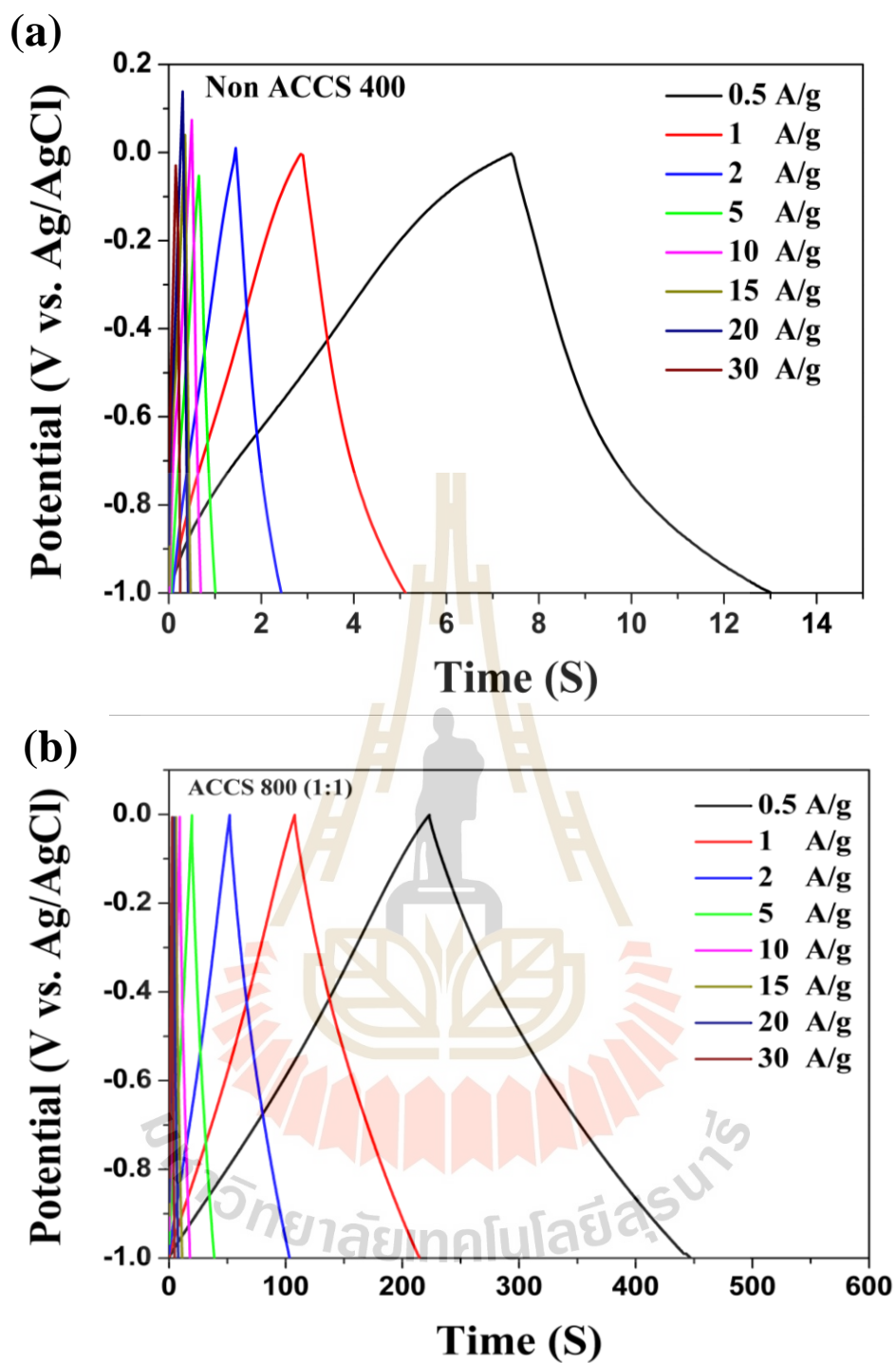
(b) ACCS 800 (1:1)

Figure 4.28 Galvanostatic charge-discharge curves of the activated carbon derived from cassava starch: (a) Non-ACCS 400, (b) ACCS 800 (1:1), (c) ACCS 800 (1:3), (d) ACCS 800 (1:5) and (E) GCD curve comparison capacitance value of all sample.

(c)

(d)
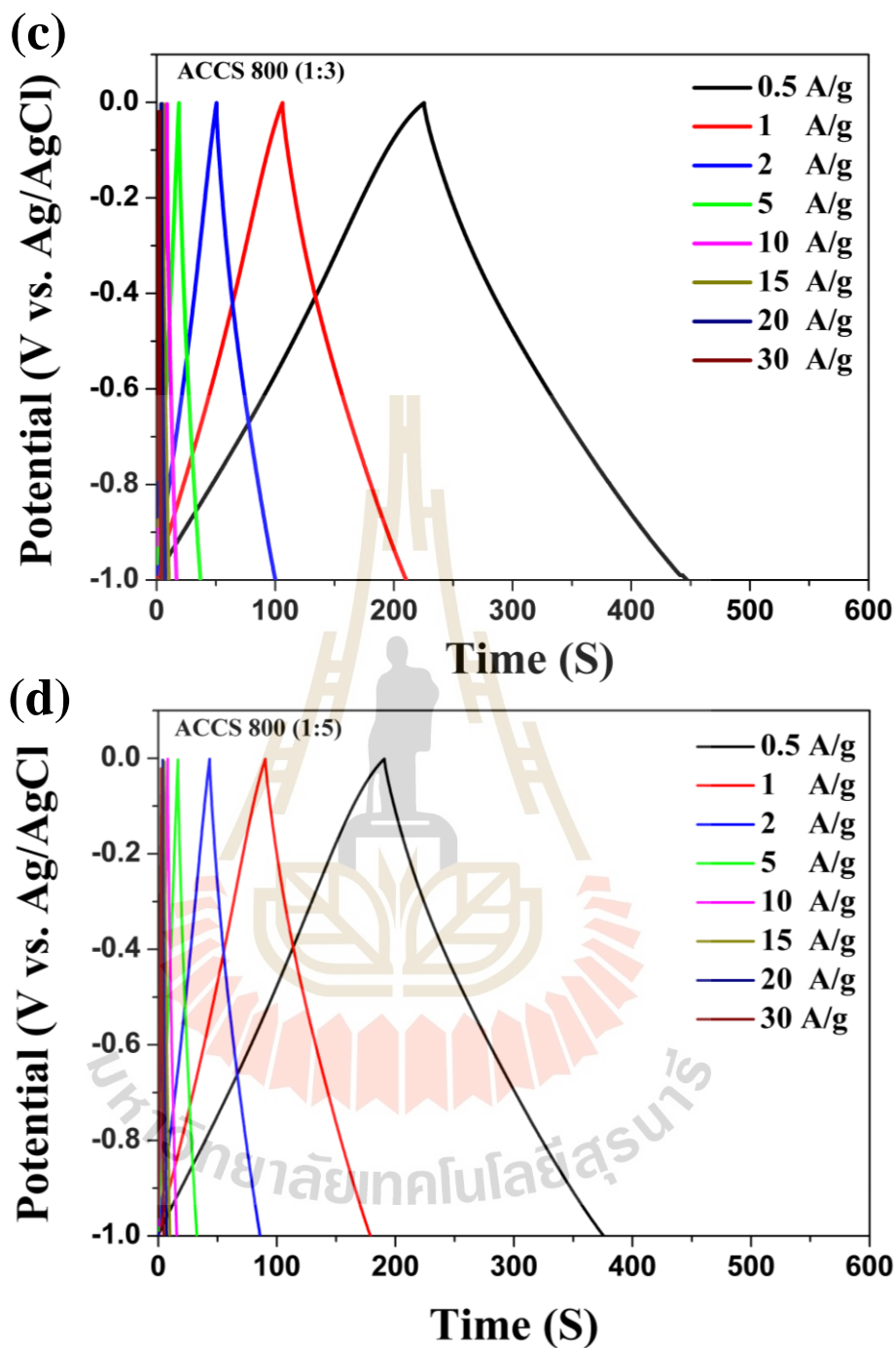
Figure 4.28 (Continued) Galvanostatic charge-discharge curves of the activated carbon derived from cassava starch: (a) Non-ACCS 400, (b) ACCS 800 (1:1), (c) ACCS 800 (1:3), (d) ACCS 800 (1:5) and (E) GCD curve comparison capacitance value of all sample.
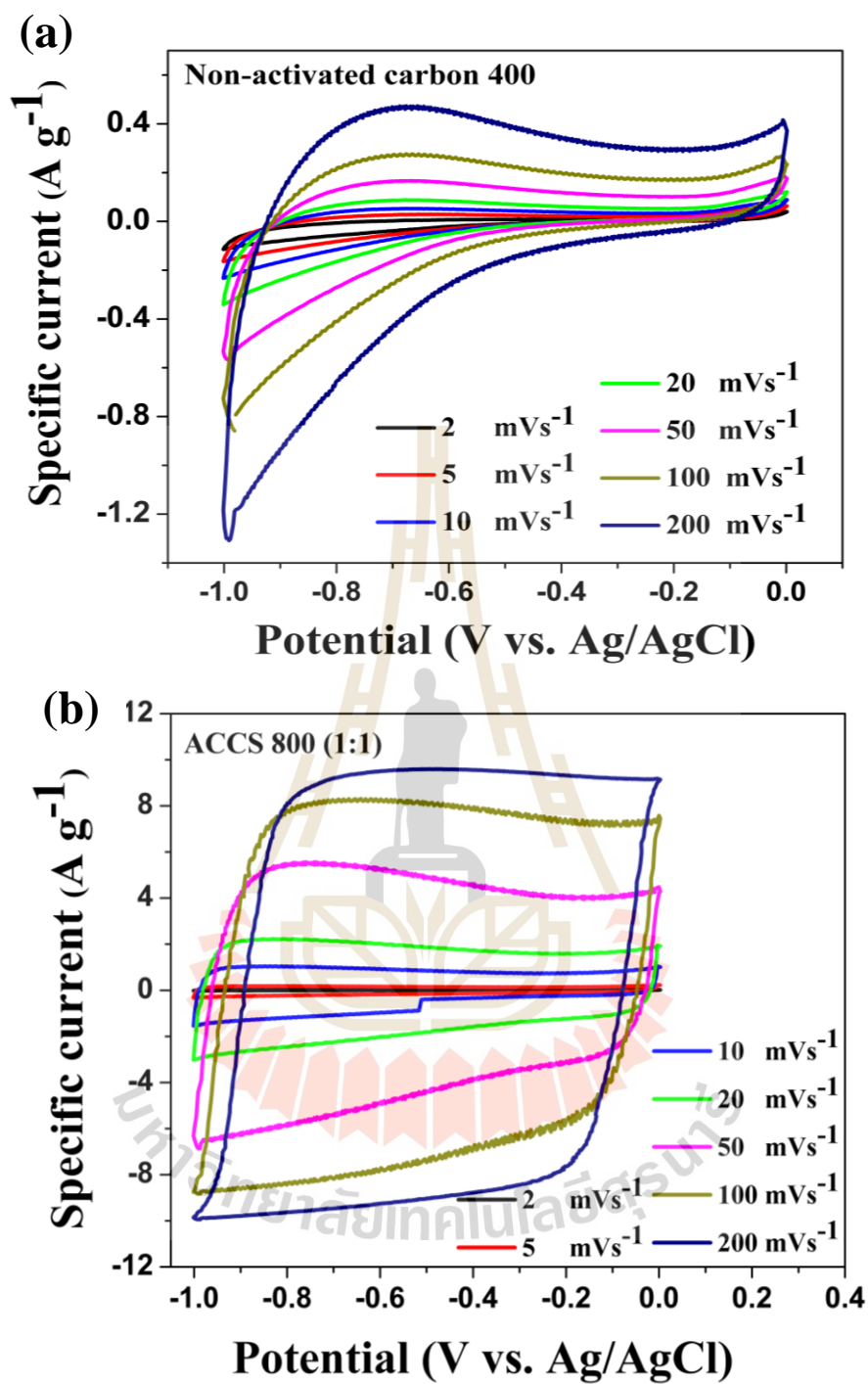
(e)

Figure 4.28 (Continued) Galvanostatic charge-discharge curves of the activated carbon derived from cassava starch: (a) Non-ACCS 400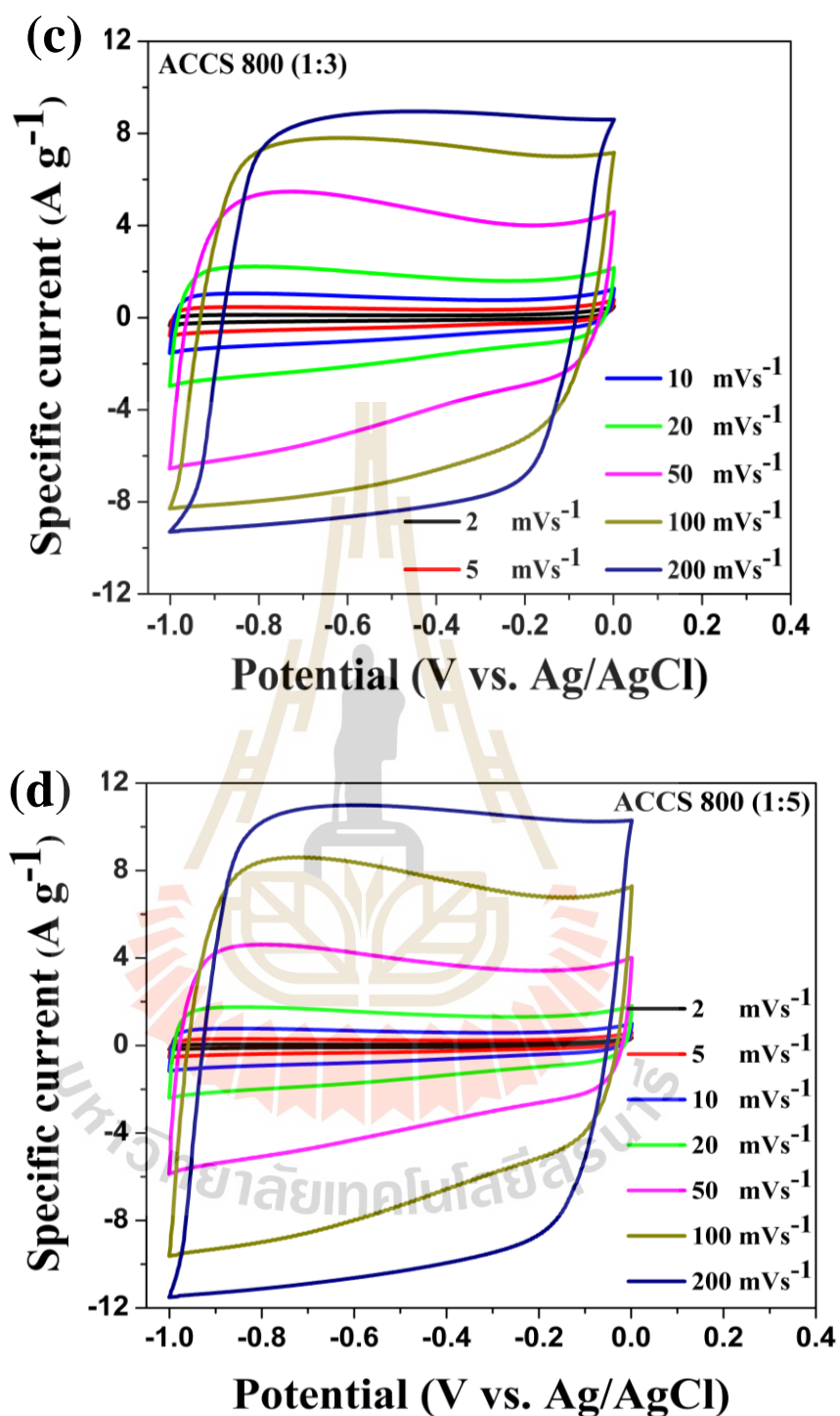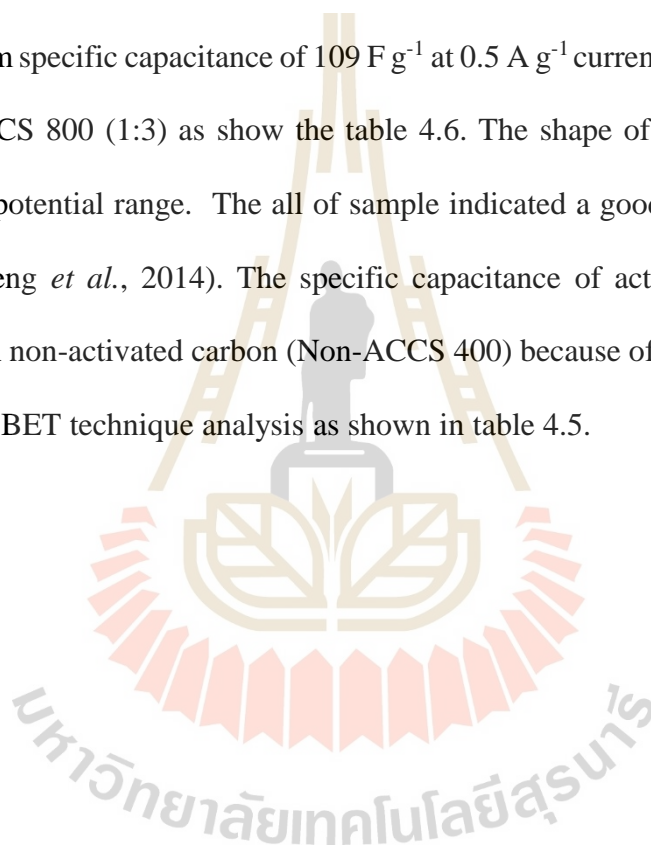, (b) ACCS 800 (1:1), (c) ACCS 800 (1:3), (d) ACCS 800 (1:5) and (e) GCD curve comparison capacitance value of all sample.

Table 4.6 Specific capacitance from GCD curve of non-activated and activated

carbon of ACCS 800 (1:1), (ACCS 800 (1:3) and ACCS 800 (1:5) derived from

cassava starch.

Sample	Current density (A/g)							
	0.5	1	2	5	10	15	20	30
ACCS 800 (1:1)	101	98	95	91	87	85	83	80
ACCS 800 (1:3)	109	104	101	97	94	91	89	86
ACCS 800 (1:5)	97	92	89	85	83	81	79	77

4.3.2.4 The Nyquist plot of non-activated and activated carbon

The behavior of the activated carbon electrodes was further investigated by

the electrochemical impedance spectroscopy (EIS). Figure. 4.26 shows the Nyquist plot

of the impedance for the activated carbon electrodes. The solution resistance (Rs)

interpreted from the intercept at Z′ axis (inset in figure 4.26) indicates that the non-

activated carbon electrode has the Rs value higher than the activated carbon electrode.

The Rs not tends to increase with KOH ratio, The better electrochemical performance

of for ACCS 800 (1:1), ACCS 800 (1:3) and ACCS 800 (1:5) can be attribution to the

better electronic compare with non-activated carbon (Peng *et al.*, 2014).
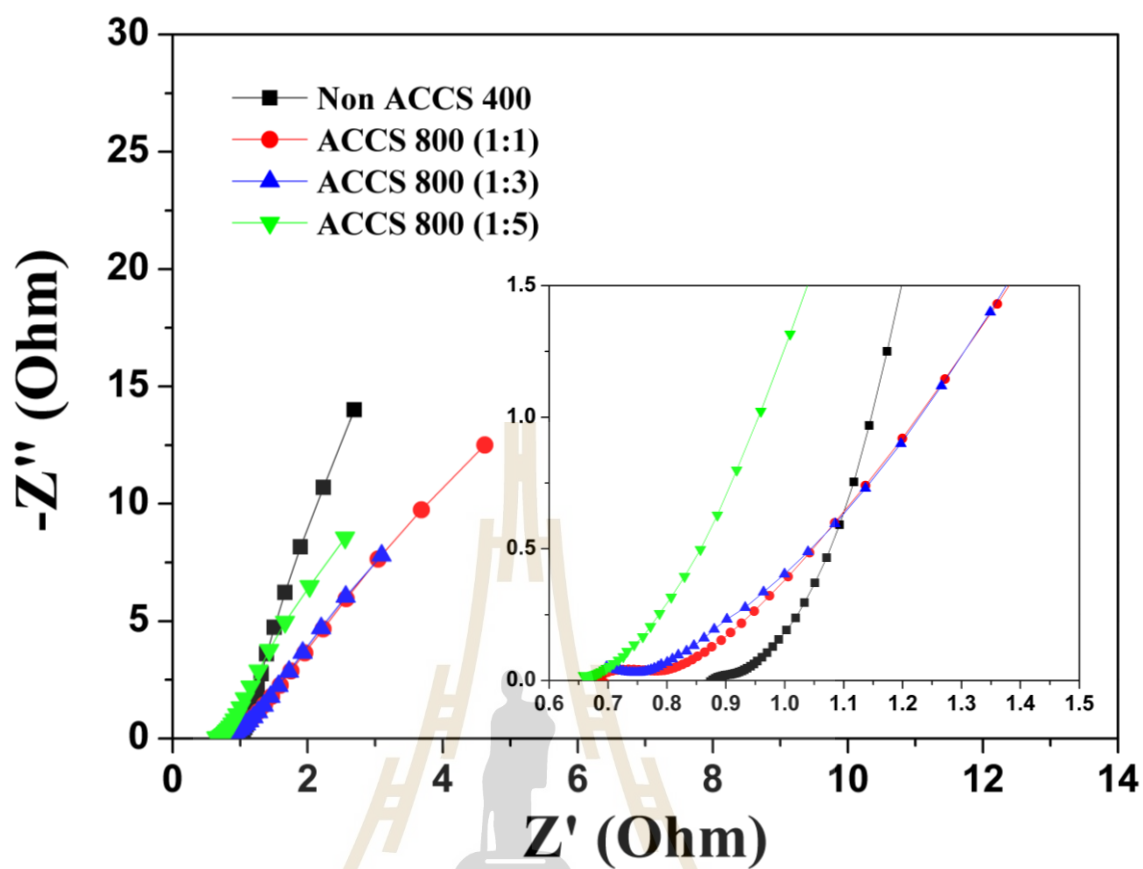
Figure 4.29 the Nyquist plot of non-activated carbon and activated carbon drive from

cassava starch.

4.3.2.5 The cycle life of non-activated carbon and activated carbon derived from cassava starch at 2 A g⁻¹

The cyclic lifetime for the ACCS 800 (1:1) sample which has the highest specific capacitance is shown in the figure 4.27. But specific capacitance increasing due to the high surface to volume ratio of ACCS 800 (1:1) compare with ACCCS 800 (1:3) and ACCCS 800 (1:5). Indicating, allowing to more active surfaces for ion adsorption. The measurement was performed in 6 M NaOH electrolyte with 1000 cycles at the current density of 2 A g⁻¹. The Coulomb efficiency of Non ACCS 400, ACCS 800 (1:1), ACCS 800 (1:3) and ACCS 800 (1:5) samples remains the value of 53 %, 87 %, 94 % and 111 %, respectively after 1000 cycles. This result indicate that the activated carbon electrode has long life cycle stability and good electrochemical conductivity (Huang *et al.*, 2014; Li *et al.*, 2008).
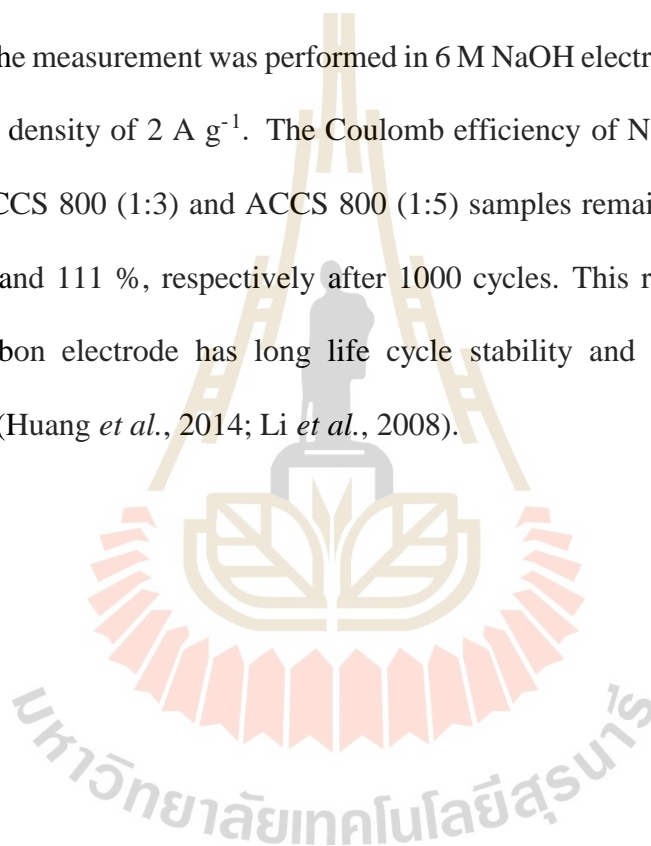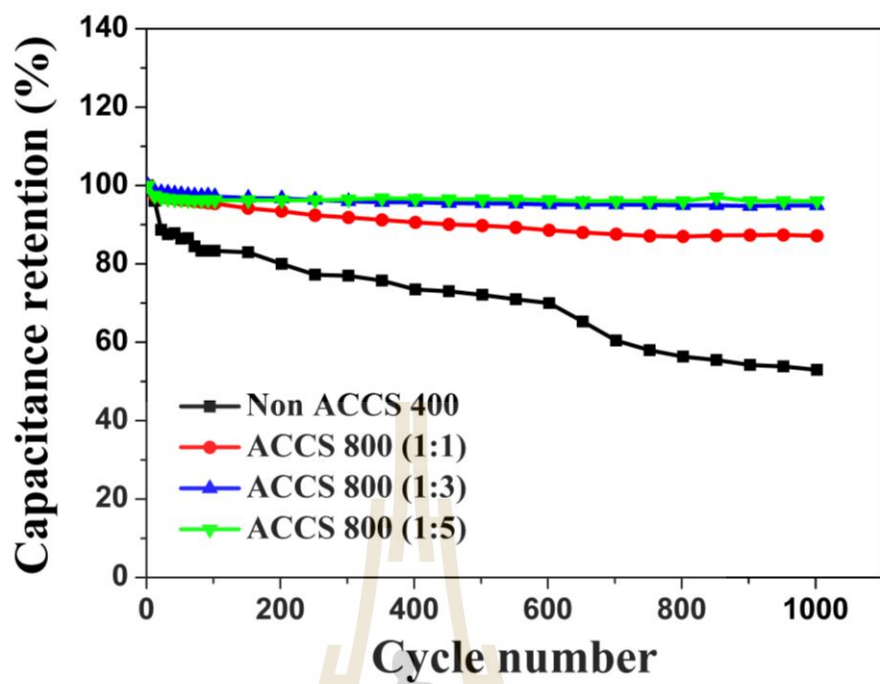
Figure 4.30 The cycle life of non-activated carbon and activated carbon drive from cassava starch.
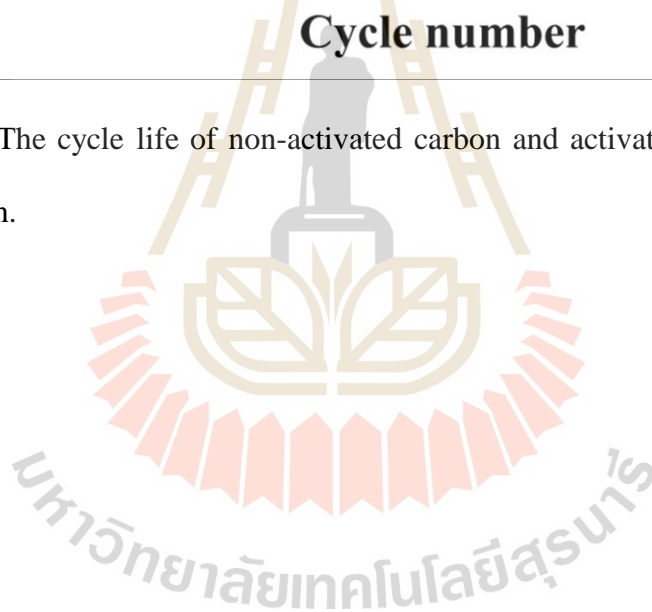
CHAPTER V

CONCLUSION

In this study, the activated carbon of potassium hydroxide derived from cassava starch have been successfully fabricated, which calcined by using argon atmosphere of stabilization carbonization. The cassava starch source was in Thailand. The morphology, thermal stability, surface chemistry, microstructure, porosity, and chemical state were investigated by XRD, SEM, BET FTIR and XPS. The electrochemical properties were studied via three electrochemical techniques including CV, GCD and EIS. From the results and discussion, the conclusion of the whole thesis can be drawn as follows. We have successfully preparation of activated carbon from cassava starch by using potassium hydroxide agent. The surface area is highest at 2000 $m^2\,g^{-1}$. The adding the KOH agent can affect to pore structure and surface area of the electrode material. The electrochemical properties of the electrode depend on pore structure and concentration ratio of the KOH agent. The decreasing of the pore structure by adding KOH can improve the specific capacitance of activated carbon from the cassava starch. The activated carbon electrode exhibits the highest specific capacitance of 130 F g^{-1} at 0.5 A g^{-1} current density. The activated carbon from cassava starch is a good choice as the electrode material for supercapacitor applications.

Suggestion

Enhanced supercapacitor could be obtained by designing electrode materials as EDLC. In this thesis, the improving on specific capacitance by activated carbon results in high energy and power density for the electrochemical performance of the materials. Moreover, the development of new material should be considered the important factors, such as cost, toxicity, light weigh lifetime etc. However, the biomass and natural material application is a good choice for the development to supercapacitor application.

REFERENCES
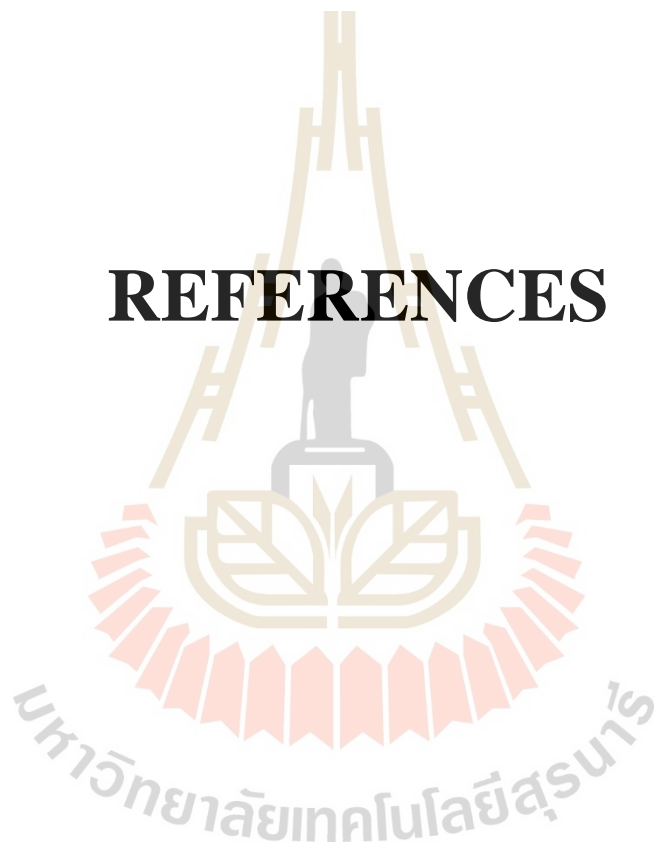
REFERENCES

ALOthman, Z. (2012). A review: fundamental aspects of silicate mesoporous materials. **Materials.** 5(12): 2874-2902.

Cao, Y., Wang, K., Wang, X., Gu, Z., Fan, Q., Gibbons, W., Hoefelmeyer, J. D., Kharel, P. R. and Shrestha, M. J. E. A. (2016). Hierarchical porous activated carbon for supercapacitor derived from corn stalk core by potassium hydroxide activation. **Electrochimica Acta.** 212: 839-847.

Chandra, A. (2012). Supercapacitors: an alternate technology for energy storage. **Proceedings of the National Academy of Sciences, India Section A: Physical Sciences.** 82(1): 79-90.

Chen, S.-M., Ramachandran, R., Mani, V. and Saraswathi, R. (2014). Recent advancements in electrode materials for the high-performance electrochemical supercapacitors: a review. **International Journal of Electrochemcal Science.** 9: 4072-4085.

Chmiola, J., Yushin, G., Gogotsi, Y., Portet, C., Simon, P. and Taberna, P.-L. (2006). Anomalous increase in carbon capacitance at pore sizes less than nanometer. **Science.** 313(5794): 1760-1763.

Conway, B. E. (2013). **Electrochemical supercapacitors: scientific fundamentals and technological applications.** New York, Springer Science & Business Media.

Elmouwahidi, A., Zapata-Benabithe, Z., Carrasco-Marín, F. and Moreno-Castilla, C. (2012). Activated carbons from KOH-activation of argan (Argania spinosa) seed shells as supercapacitor electrodes. **Bioresource technology.** 111: 185-190.

Enock, T. K., King'ondu, C. K., Pogrebnoi, A. and Jande, Y. A. C. (2017). Status of biomass derived carbon materials for supercapacitor application. **International Journal of Electrochemistry.** 14.

Fan, Z., Zhao, Q., Li, T., Yan, J., Ren, Y., Feng, J. and Wei, T. (2012). Easy synthesis of porous graphene nanosheets and their use in supercapacitors. **Carbon.** 50(4): 1699-1703.

Farma, R., Deraman, M., Awitdrus, A., Talib, I., Taer, E., Basri, N., Manjunatha, J., Ishak, M., Dollah, B. and Hashmi, S. (2013). Preparation of highly porous binderless activated carbon electrodes from fibres of oil palm empty fruit bunches for application in supercapacitors. **Bioresource technology.** 132: 254-261.

Frackowiak, E. (2007). Carbon materials for supercapacitor application. **Physical chemistry chemical physics.** 9(15): 1774-1785.

Gao, Z., Zhang, Y., Song, N. and Li, X. (2017). Biomass-derived renewable carbon materials for electrochemical energy storage. **Materials Research Letters.** 5(2): 69-88.

Huang, Y., Candelaria, S. L., Li, Y., Li, Z., Tian, J., Zhang, L. and Cao, G. (2014). Sulfurized activated carbon for high energy density supercapacitors. **Journal of Power Sources.** 252: 90-97.

Huang, Y. and Zhao, G. J. H. (2016). Preparation and characterization of activated carbon fibers from liquefied wood by KOH activation. **Holzforschung.** 70(3): 195-202.

Ioannidou, O. and Zabaniotou, A. (2007). Agricultural residues as precursors for activated carbon production—a review. **Renewable and sustainable energy reviews.** 11(9): 1966-2005.

Jiang, S., Zhang, Z., Qu, Y., Wang, X., Li, Q., Lai, Y. and Li, J. (2014). Activated carbon aerogels with high bimodal porosity for lithium/sulfur batteries. **Journal of Solid State Electrochemistry.** 18(2): 545-551.

Jiang, S., Zhang, Z., Qu, Y., Wang, X., Li, Q., Lai, Y. and Li, J. J. J. o. S. S. E. (2014). Activated carbon aerogels with high bimodal porosity for lithium/sulfur batteries. **Journal of Solid State Electrochemistry.** 18(2): 545-551.

Kalderis, D., Bethanis, S., Paraskeva, P. and Diamadopoulos, E. (2008). Production of activated carbon from bagasse and rice husk by a single-stage chemical activation method at low retention times. **Bioresource technology.** 99(15): 6809-6816.

Kalyani, P. and Anitha, A. (2013). Biomass carbon & its prospects in electrochemical energy systems. **International Journal of Hydrogen Energy.** 38(10): 4034-4045.

Kim, I.-H. and Kim, K.-B. (2006). Electrochemical characterization of hydrous ruthenium oxide thin-film electrodes for electrochemical capacitor applications. **Journal of The Electrochemical Society.** 153(2): A383-A389.

Kötz, R. and Carlen, M. (2000). Principles and applications of electrochemical capacitors. **Electrochimica acta.** 45(15-16): 2483-2498.

Lee, J.-L., Kim, J. K., Lee, J. W., Park, Y. J. and Kim, T. (1999). Effect of surface treatment by KOH solution on ohmic contact formation of p-type GaN. **Solid-State Electronics.** 43(2): 435-438.

Leng, Y. (2009). **Materials characterization: introduction to microscopic and spectroscopic methods.** John Wiley & Sons.

Li, Q.-Y., Wang, H.-Q., Dai, Q.-F., Yang, J.-H. and Zhong, Y.-L. (2008). Novel activated carbons as electrode materials for electrochemical capacitors from a series of starch. **Solid State Ionics.** 179(7-8): 269-273.

Lu, M. (2013). **Supercapacitors: materials, systems, and applications.** John Wiley & Sons.

Ma, G., Yang, Q., Sun, K., Peng, H., Ran, F., Zhao, X. and Lei, Z. (2015). Nitrogen-doped porous carbon derived from biomass waste for high-performance supercapacitor. **Bioresource technology.** 197: 137-142.

Pandolfo, A. and Hollenkamp, A. (2006). Carbon properties and their role in supercapacitors. **Journal of power sources.** 157(1): 11-27.

Peng, C., Lang, J., Xu, S. and Wang, X. (2014). Oxygen-enriched activated carbons from pomelo peel in high energy density supercapacitors. **RSC Advances.** 4(97): 54662-54667.

Peng, C., Lang, J., Xu, S. and Wang, X. J. R. A. (2014). Oxygen-enriched activated carbons from pomelo peel in high energy density supercapacitors. **RSC Advances.** 4(97): 54662-54667.

Peng, C., Yan, X.-b., Wang, R.-t., Lang, J.-w., Ou, Y.-j. and Xue, Q.-j. (2013). Promising activated carbons derived from waste tea-leaves and their application in high performance supercapacitors electrodes. **Electrochimica Acta.** 87: 401-408.

Peng, Z., Guo, Z., Chu, W. and Wei, M. J. R. A. (2016). Facile synthesis of high-surface-area activated carbon from coal for supercapacitors and high CO_2 sorption. **RSC Advances.** 6(48): 42019-42028.

Pushparaj, V. L., Shaijumon, M. M., Kumar, A., Murugesan, S., Ci, L., Vajtai, R., Linhardt, R. J., Nalamasu, O. and Ajayan, P. M. (2007). Flexible energy storage devices based on nanocomposite paper. **Proceedings of the National Academy of Sciences.** 104(34): 13574-13577.

Puziy, A. M., Poddubnaya, O. I., Martínez-Alonso, A., Suárez-García, F. and Tascón, J. M. (2005). Surface chemistry of phosphorus-containing carbons of lignocellulosic origin. **Carbon.** 43(14): 2857-2868.

Rufford, T. E., Hulicova-Jurcakova, D., Khosla, K., Zhu, Z. and Lu, G. Q. (2010). Microstructure and electrochemical double-layer capacitance of carbon electrodes prepared by zinc chloride activation of sugar cane bagasse. **Journal of Power Sources.** 195(3): 912-918.

Shukla, A., Banerjee, A., Ravikumar, M. and Jalajakshi, A. (2012). Electrochemical capacitors: Technical challenges and prognosis for future markets. **Electrochimica Acta.** 84: 165-173.

Shulga, Y. M., Shulga, N. Y. and Parkhomenko, Y. N. (2015). Carbon nanostructures reduced from graphite oxide as electrode materials for supercapacitors. **Modern Electronic Materials.** 1(1): 1-9.

Simon, P. and Gogotsi, Y. (2008). Materials for electrochemical capacitors. **Nature materials.** 7(11): 845-854.

Simon, P. and Gogotsi, Y. (2010) Materials for electrochemical capacitors. **In Nanoscience and Technology: A Collection of Reviews from Nature Journals World Scientific**, pp. 320-329.

Sing, K. S. (1985). Reporting physisorption data for gas/solid systems with special reference to the determination of surface area and porosity (Recommendations 1984). **Pure and applied chemistry.** 57(4): 603-619.

Sun, K., chun Jiang, J. J. B. and bioenergy (2010). Preparation and characterization of activated carbon from rubber-seed shell by physical activation with steam. **Biomass and Bioenergy**. 34(4): 539-544.

Sung, J.-H., Kim, S.-J., Jeong, S.-H., Kim, E.-H. and Lee, K.-H. (2006). Flexible micro-supercapacitors. **Journal of power sources.** 162(2): 1467-1470.

Taberna, P.-L., Portet, C. and Simon, P. (2006). Electrode surface treatment and electrochemical impedance spectroscopy study on carbon/carbon supercapacitors. **Applied Physics A.** 82(4): 639-646.

Wang, K., Zhao, N., Lei, S., Yan, R., Tian, X., Wang, J., Song, Y., Xu, D., Guo, Q. and Liu, L. (2015). Promising biomass-based activated carbons derived from willow catkins for high performance supercapacitors. **Electrochimica Acta.** 166: 1-11.

Yagmur, E., Ozmak, M. and Aktas, Z. (2008). A novel method for production of activated carbon from waste tea by chemical activation with microwave energy. **Fuel.** 87(15-16): 3278-3285.

Yakout, S. and El-Deen, G. S. J. A. J. o. C. (2016). Characterization of activated carbon prepared by phosphoric acid activation of olive stones. **Arabian Journal of Chemistry.** 9: S1155-S1162.

Yan, J., Liu, J., Fan, Z., Wei, T. and Zhang, L. (2012). High-performance supercapacitor electrodes based on highly corrugated graphene sheets. **Carbon.** 50(6): 2179-2188.

Yu, A., Chabot, V. and Zhang, J. (2013). **Electrochemical supercapacitors for energy storage and delivery: fundamentals and applications.**

Zhang, J., Zhang, L., Liu, H., Sun, A. and Liu, R. (2011). **Electrochemical Technologies for Energy Storage and Conversion.** Wiley-VCH.

Zheng, C., Zhou, X., Cao, H., Wang, G. and Liu, Z. (2014). Synthesis of porous graphene/activated carbon composite with high packing density and large specific surface area for supercapacitor electrode material. **Journal of power sources.** 258: 290-296.

Zheng, C., Zhou, X., Cao, H., Wang, G. and Liu, Z. J. J. o. p. s. (2014). Synthesis of porous graphene/activated carbon composite with high packing density and large specific surface area for supercapacitor electrode material. **Journal of power sources.** 258: 290-296.

Zhou, Q. Q., Chen, X. Y. and Wang, B. (2012). An activation-free protocol for preparing porous carbon from calcium citrate and the capacitive performance. **Microporous and Mesoporous Materials.** 158: 155-161.

Zhou, X., Li, H. and Yang, J. (2016). Biomass-derived activated carbon materials with plentiful heteroatoms for high-performance electrochemical capacitor electrodes. **Journal of Energy Chemistry.** 25(1): 35-40.

Zhu, Y., Murali, S., Stoller, M. D., Ganesh, K., Cai, W., Ferreira, P. J., Pirkle, A., Wallace, R. M., Cychosz, K. A. and Thommes, M. (2011). Carbon-based supercapacitors produced by activation of graphene. **Science.** 332(6037): 1537-1541.

CURRICULUM VITAE

Name   Miss. Suphawi Chaisit

Date of Birth   June 12, 1993

Place of Birth   127 Moo 5, Ban Phudin, Tambol Lupca, Kaengkhrow

                      District, Chaiyaphum, 36150, Thailand

Education

2016-2019   Suranaree University of Technology, Nakhon

                      Ratchasima, Thailand. Ms.C in Physics

2012-2016   Suranaree University of Technology, Nakhon

                      Ratchasima, Thailand. B.S. in Physics

Position and Place of

Work   Student of Physics

                      Suranaree University of Technology, Nakhon

                      Ratchasima, Thailand.